Determining the jet energy resolution of the ATLAS detector using the bisector method

Tanja Holm

Masterarbeit in Physik
angefertigt im Physikalischen Institut

vorgelegt der
Mathematisch-Naturwissenschaftlichen Fakultät
der
Rheinischen Friedrich-Wilhelms-Universität
Bonn

April 2018

I hereby declare that this thesis was formulated by myself and that no sources or tools other than those cited were used.

Bonn, ...
Date Signature

1. Gutachter: Prof. Dr. Ian C. Brock
2. Gutachter: Prof. Dr. Klaus Desch

Acknowledgements

I would like to thank everyone who helped and supported me during my masterthesis.

Special thanks of course go to my family and friends who were always there for me and gave me general advice at all stages of my study. Another special thanks goes to everyone in the group. Thanks for always being there answering questions and discussing over various topics. This thesis would have not been possible without Prof. Dr. Ian Brock who gave me the opportunity to write my thesis about this interesting topic and Dr. Regina Moles-Valls my supervisor who always helped me with my questions despite here limited time. Additional thanks goes to everyone in the Desch group for the discussions during the Jamborees. Of course also thanks to the members of the ATLAS jet calibration group for providing me this topic and helpful suggestions during my work.

Contents

CHAPTER 1

Introduction

What is this? What does this consist of? How does it behave? These are basic questions that build the foundation of curiosity, one of the most fundamental traits of humans. However, physicists have taken this question to a new level. These questions are not only applied to macroscopic objects that we can hold in our hands but also to things that are way beyond this scale, either much bigger such as stars and the universe or to the smallest components of matter that mankind can reach. If one looks at the latter physicists have entered territory where our imagination gets to its boundaries. The smallest things that we know are actually the particles in the Standard Model and they are to our knowledge even point-like.

That does not mean those particles do not exist. On the contrary even more particles exist than one would assume. For each particle that exists in nature two particles exist that behave similarly but have another mass. How do physicists know that? They produced them. By colliding particles with high energies onto each other new particles can be produced and studied. Some of them even have very interesting properties, such as particles that can not stay alone. They are called quarks and gluons. Instead these particles produce themselves a lot of friends. This sounds like an opportunity to study even more particles. But unfortunately disentangling them is almost not possible. Instead these groups of particles are called jets and studied as a whole. They still have the properties of the first particle so measuring them leads to some use in further analysis. The measurement of these objects is however a great challenge. How should one know what particles belong to the jet? How could one measure all of these particles simultaneously? What can one actually say about the thing that has been reconstructed? Exactly the last question is what this thesis is about. If a jet is reconstructed with a certain energy one also needs to know how accurate the energy measurement is. Assigning it an energy of 105 GeV[1] does tell nothing if it is not known if the precision of this measurement is 0.5 GeV, 10 GeV or 100 GeV. This characteristic is called the jet energy resolution.

The goal of this thesis is to determine the jet energy resolution of the ATLAS detector using the bisector method. This is a mostly data-driven approach and stands is complementary to the direct balance method which has already been applied to the current dataset. One advantage of it is that a large part of the uncertainty can actually be obtained directly from data. This method was applied similarly at 7 TeV [1] and 8 TeV[2], but this is the first time the bisector method has been applied in Run 2.

To explain how this is done the thesis is organized at follows: in chapter 2 the basics of our knowledge about the Standard Model are presented. In chapter 3 an overview about the experiment and experimental methods is given. A more detailed look at jets is presented in chapter 4 before in chapter 5 the implementation of the bisector method is explained. The results of this can be found in chapter 6.

[1] 1 eV corresponds to the energy one electron has after being accelerated by 1 V

CHAPTER 2

Theory

2.1 Standard Model

The Standard Model is a successful theory that describes most of our knowledge about the (to our knowledge) fundamental constituents and interactions in nature. It has crystallized out over the last decades through a lot of experiments and different theories to combine all this knowledge into one theory. This chapter gives an overview over the Standard Model and mentions a few key experiments as well as some drawbacks of the model. A more detailed description can be found e.g. at [3].

2.1.1 Particles

The Standard Model is based on in total 30 particles which are believed to build up all the matter and interactions possible (without gravity, see section 2.1.3). They are characterized by their properties as mass, spin, different kinds of charges and how they interact with each other. Particles are divided into different subgroups, where the basic classification is **boson** or **fermion**:

Bosons

Bosons are defined as particles with an integer spin. Most of them are associated to an interaction, for which they are the force carriers.

- **Photon (γ):** force carrier of the **electromagnetic force**, interacts with anything that has electric charge, but carries none itself. Acts attractive or repulsive depending on the involved electric charges. At macroscopic scales one would call them electromagnetical radiation. The particle itself does not carry any mass.
- **Gluon (g):** force carrier of the **strong force**, interacts with anything that has colour charge. Since it carries colour it also interacts with itself. Acts strongly attractive. It also does not carry mass.
- **W^+, W^- and Z:** force carriers of the weak force, couple to anything with helicity (which is basically every fermion). Since they have a finite mass they are harder to exchange and thus the weak force is very short ranged. The weak force itself is normally not recognized because of an attractive or repulsive effect, but rather by enabling decays.
- **Higgs H:** the Higgs is not associated to a force but rather to the mechanism that gives mass to the elementary particles (not the weight). Thus it couples to the mass of particles. The Higgs particle

is a bit outstanding in this list since it has just recently been discovered at the LHC in 2012 [4, 5] also some of its properties are different to the others (scalar not vector particle).

Fermions

Fermions are defined as particles with half-integer spin. They actually form the matter and are divided into even more subgroups. Each of the subgroups consists of three particles which behave similarly, the only way to distinguish them is their mass. One calls the difference between them the flavour charge. For each subgroup there exists a group with exactly the same mass but opposite charges, the so-called antiparticles.

- charged leptons: ($\boldsymbol{e^-}$, $\boldsymbol{\mu^-}$, $\boldsymbol{\tau^-}$) interact electromagnetically and weakly. In nature[1] one can find only the electron e. Together with a nucleus it forms neutral atoms, which all matter in nature consists of. Thus it is (in presence or absence) the most common cause for a manifestation of the electromagnetic force in our everyday live. It has already been discovered in 1897 [7].
- charged anti-leptons: ($\boldsymbol{e^+}$, $\boldsymbol{\mu^+}$, $\boldsymbol{\tau^+}$) interact electromagnetically and weakly. In contrast to charged leptons they carry positive electronic charge. Only the positron (e^+) is observed in nature for short time-scales as the so called β^+-radiation in nuclear decays.
- neutrinos: ($\boldsymbol{\nu_e}$, $\boldsymbol{\nu_\mu}$, $\boldsymbol{\nu_\tau}$) interact only weakly and thus are hard to observe directly. Indirectly one can only observe the electron neutrino ν_e in nature as missing energy in the β^+ nuclear decay [8].
- anti-neutrinos: ($\boldsymbol{\overline{\nu}_e}$, $\boldsymbol{\overline{\nu}_\mu}$, $\boldsymbol{\overline{\nu}_\tau}$) also interact only weakly and thus are hard to observe directly. Analogue to the ν_e one can observe the anti electron neutrino $\overline{\nu}_e$ as missing energy in the β^- nuclear decay.
- up-type quarks: (**up** $\boldsymbol{u}$, **charm** $\boldsymbol{c}$, **top** $\boldsymbol{t}$) interact weakly, strongly and electromagnetically (electric charge $+\frac{2}{3}$). In nature the up quark forms protons ($u\ u\ d$) and neutrons ($u\ d\ d$) together with the down quark.[2]
- anti-up-type quarks: ($\boldsymbol{\overline{u}}$, $\boldsymbol{\overline{c}}$, $\boldsymbol{\overline{t}}$) interact weakly, strongly and electromagnetically (electric charge $-\frac{2}{3}$). These type of quarks can not (easily) be observed in nature.
- down-type quarks: (**down** $\boldsymbol{d}$**, strange** $\boldsymbol{s}$**, bottom** $\boldsymbol{b}$) interact weakly, strongly and electromagnetically (electric charge $-\frac{1}{3}$). In nature the down quark forms protons ($u\ u\ d$) and neutrons ($u\ d\ d$) together with the up quark.
- anti-down-type quarks: ($\boldsymbol{\overline{d}}$, $\boldsymbol{\overline{s}}$, $\boldsymbol{\overline{b}}$) interact weakly, strongly and electromagnetically (electric charge $+\frac{1}{3}$).These type of quarks can not (easily) be observed in nature.

Based on their ability to interact two subcategories of all fermions can be formed: **quarks** which interact strongly and **leptons** which do not. Important to note is also that all charges like the electric charge are conserved and opposite charges can annihilate. Because of this particles and their corresponding antiparticle (e.g. s and $\overline{s}$) can annihilate with each other. In contrast two particles of the same charge could not annihilate into an uncharged particle. More information on this and other interactions can be found in the next section.

[1] With nature here is meant matter found and originating on the earth. It is known that fast extraterrestrial particles collide with our atmosphere and produce a lot of particles. Also neutrinos come from extraterrestrial sources as the sun [6]. Also particles are created in colliders (see section 3.1). This is not meant in this list.

[2] In principle protons and neutrons due to the nature of the strong force also consists of all other quark types and gluons, but this can only be resolved at higher energies. For details have a look into section 2.2.

2.1.2 Quantum field theory

In the previous section the particles of the Standard Model were described. In this section a brief introduction to the possible interactions between these particles will be given. The focus will lie on the graphical way to describe it. For a more extensive explanation have a look into e.g. [9].

Feynman diagrams

In principle everything that is possible in the theory of the Standard Model fits into one formula, the so called Lagrangian of the Standard Model. It contains all laws of all elementary particles propagating as well as all possible interactions between them (see e.g. [9]). In order to show what is going on in a graphical way Richard Feynman introduced the so called "Feynman diagrams" [10]. Actually a numerical value[3] is assigned to it which is called the amplitude, it corresponds to the probability of this process happening. From this value the so called cross-section can be derived that includes also the kinematic characteristics of the process.

The constituents of a Feynman diagram are lines, which represent propagating particles. If multiple lines meet this corresponds to an interaction. Often the assigned coupling constant tells which interaction takes place (for example α_S for the strong force), but here they are not written, assuming that one knows from the display of the bosons which type of interaction takes place (see section 2.1.1). Time goes from left to right in all Feynman diagrams shown in this document. If the little arrow points into the direction of time it is considered as a particle while an arrow in the opposite direction is considered as the corresponding antiparticle. Thus a Feynman diagram can describe physically different situations if one turns it. In principle the amplitude stays the same. The particles in at the beginning (so here at the left border of the Feynman diagram) form the initial state. The final state is given by the particles at the end of the process (here right).

In figure 2.1 all interactions a photon can undergo are shown. As explained before one can see it just couples to electrically charged fermions (not to neutrinos) and bosons(W) but not to itself. One can see that for example the first of the graphs corresponds to a force acting between the fermion and a particle that is not in the figure. If one turns it by 120° it shows a fermion and an anti-fermion annihilating to a photon. If one turns it once again by 180° it shows a photon splitting up into a fermion- anti-fermion pair. Similar diagrams also exist for the other forces.

The boson interaction of the weak force are shown in figure 2.2. As we do have more bosons there are also more diagrams to draw. Important to note is that the two types act differently. While an interaction with a W always changes the flavour a Z never does. Also they can couple to one another.

The strong force vertices are shown in picture 2.3. Additional to the interaction with quarks (not leptons) we also have here a self-coupling of the gluons to themselves as in the weak force. But since the gluon itself has no mass this puts us into some problems since one can create a large amount of gluons. Also the coupling constant α_s is much higher at lower energies which makes things harder to calculate and to handle in general. See section 2.2 for more details.

In principle one can put together all of these vertices as you like as long as conserved quantities as energy and momentum are not violated. An example can be seen in picture 2.4 where a propagating gluon splits up into two quarks and they recombine shortly after (this diagram becomes more important in section 2.2). Another more complicated example can be seen in figure 2.5 where a top quark decays into

[3] Some work has to go into the mathematics though in order to assure that it is not mathematically ill defined.

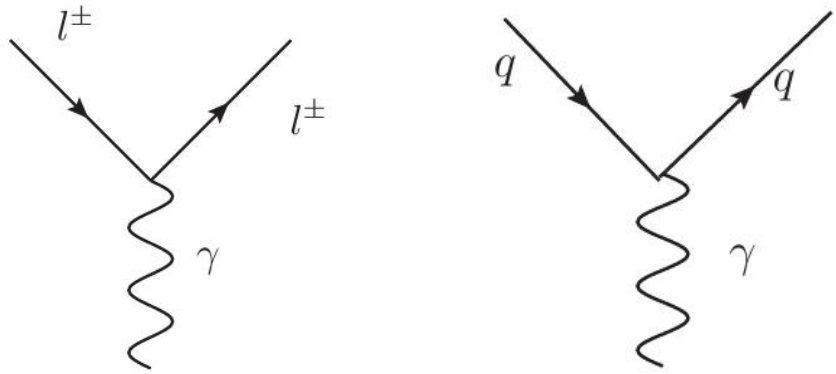

Figure 2.1: A photon can interact with both leptons and quarks.

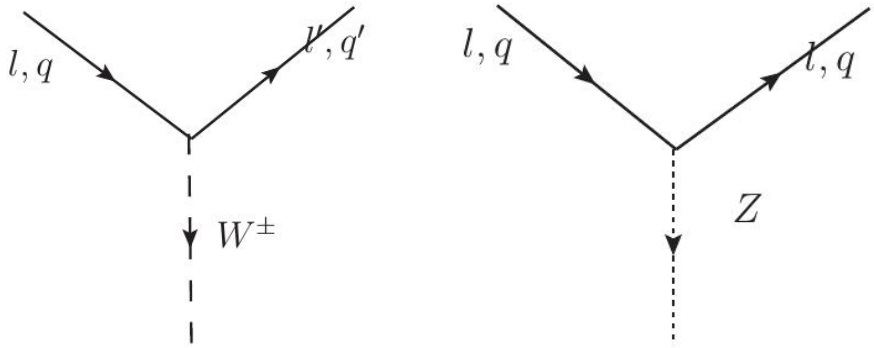

Figure 2.2: Possible vertices of the weak interaction including the Z- and the W-boson.

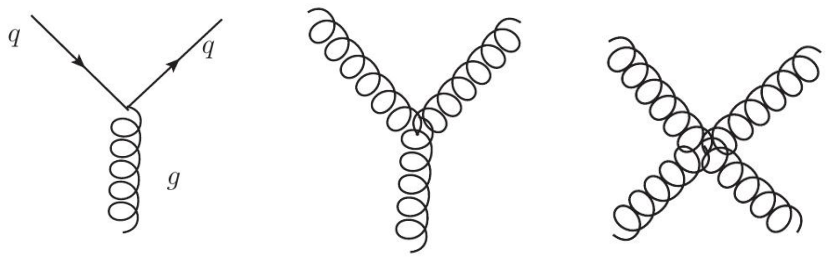

Figure 2.3: A gluon can interact with quarks or other gluons.

a b-quark and a W-boson which later decays itself into a lepton and an anti-neutrino while the b-quark radiates of an additional gluon.

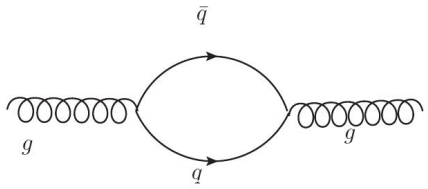

Figure 2.4: A gluon splits up into a quark and an anti-quark, which recombine later. This forms a loop.

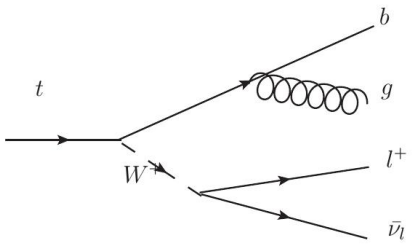

Figure 2.5: An example of a more complicated Feynman diagram, that consists of several fundamental vertices.

2.1.3 Open questions

The Standard Model is a successful theory, but there are still some questions that are not solved within it or do not fit with the outcome of experiments. Some will be mentioned here, a more detailed description can be found for example in [3].

Neutrino oscillation

Despite the fact that neutrinos are described as massless in the Standard Model they seem to have a mass. A hint to this are neutrino oscillations. An example are neutrinos that interact as ν_μ although they were created as ν_e in nuclear power plants. They should only be able to do this if they have some finite mass. However no one has been able to measure it yet, only upper limits have been extracted from experiments [11].

Gravitation

Gravitation is not included in the Standard Model. There are some attempts to unify it, but effects as the recently measured gravitational waves are not explained yet by a quantum field theory. There is some hope though that at really high energies all four forces can be described as one (the so called Grand Unified Theory).

Dark Matter

Studies of the universe, like observing the rotation speed of galaxies lead to the conclusion that a big part of matter in the universe actually does not emit electromagnetical radiation. With other words there is a lot of mass that does not emit photons, which we could measure on earth. Ordinary matter like the earth - in contrast to stars - or black holes do not contribute the needed fraction of mass in order to make up for this. The missing piece is often referred to as Dark Matter and it is possible that Dark Matter actually consists of elementary particles that are not part of the Standard Model.

2.2 QCD

As described in section 2.1.2 the strong interaction has a few features that make it harder to calculate. The theory behind describing the strong interactions with the methods of Quantum Field Theory is called Quantum Chromo Dynamics (QCD). "Chromatos" is Greek for colour, so it could be explained as "the theory of the movement of colourful objects described on the basis of Quantum Field Theory". As we have seen earlier the gluons interact with everything that carries colour charge, so quarks and other gluons. There are several hints to the idea of having an additional property associated to quarks that can take exactly three values for quarks (and three additional ones for anti-quarks). Stable objects are always neutral w.r.t. colour. So either a combination of one value combined with its corresponding anti-value or a combination of all three values (or anti-values). This resembles the symmetry of visible colours: red, green and blue light together are seen as white (so neutral) and also red and "anti-red" light, which one would call cyan, together are seen as white. That is the reason why this charge is called colour charge, there is no further connection to light (which is an electromagnetic effect). The quark type does not influence which colour charge the quarks should have. The two forms of neutral states are:

- **Mesons:** colour-anticolour neutral states. Since quarks do carry colour charge and anti-quarks carry anti-colour charge Mesons are formed from a combination of both. An often occurring example is the π^+ which consists of an up-type quark and an down type anti-quark.
- **Baryons:** mixture of all three colours. So a combination of three quarks. The lightest baryon is the proton which consists of two up-type quarks and one down-type quark. Of course it is also possible to combine three anti-quarks with all three different anti-colours to an anti-baryon.

But things are not quite as easy as that. As mentioned earlier gluons are not colour-neutral to the outside[4]. Since only colour-neutral states are stable gluons are not stable, but occur only at small distances. Also gluons attract each other, because they all carry colour charge themselves. This leads to behaviours that are unique among the forces:

Coupling constant

The coupling constant gives the strength of the coupling or the possibility for an interaction to happen. In section 2.1.2 basic Feynman diagrams were discussed. As said these can be combined in various different ways. For each basic process including a given number of couplings there exist infinitely more where the initial and final state particles are the same but additional vertices occur. They are called higher order diagrams. If the coupling constant is way below one the calculation converges. So these additional

[4] In principle neutral is not a well-defined description for the colour states. They are more precisely referred to as singlets. Gluon colours are also not easily described by states like "red and anti-green". But since we do not measure the colour charge itself it does not that much for this thesis. For more details see [12]

diagrams can be omitted in the calculation of the final process and one would still get to a pretty accurate result.

In figure 2.6 the α_s can be seen as a function of the energy scale. Because of the inclusion of higher order diagrams in a single gluon line it depends on the transferred energy (q^2), so its actually not really "constant". The calculation process is called renormalization and is also applied to the other coupling constants. In contrast to them α_s rises at lower q^2 to values $O(1)$. This leads to additional difficulties of calculating the processes of QCD at low energies, because a lot of higher orders should have to be taken into account.

Proton

As mentioned in section 2.2 protons in a general way consist of two u and one d quarks. These are called valence quarks. But at low energies higher order corrections in QCD processes cannot be neglected. Since the three quarks are attracted to each other by the strong coupling constant, clearly a QCD process is going on at all times inside the proton including higher order processes. The conclusion of this is that if one shoots a projectile with the right amount of energy to resolve this structures there is a probability of scattering on gluons and even quarks that are not valence quarks inside a proton. In figure 2.7 one can see this probability as a function of momentum of the projectile, this graph looks different depending on the Q^2. These quarks are so-called sea quarks and can have in theory any flavour if the energy to produce them is high enough. All constituents of a proton are called partons. The density of partons in a proton with a given momentum can be calculated which gives the so-called particle density functions (PDFs).

2.2.1 Jets

In figure 2.8 one can see what happens if two quarks are separated from each other: an attractive force acts on them transported by gluons. The gluons themselves also carry colour charge so there is also an attractive force between them carried by even more gluons. This causes a so-called "colour-tube" between the two quarks resulting in an attractive force increasing linearly with distance. The energy density is approximatively 1GeV/fm. So if the distance becomes large enough the energy stored is big enough to produce new quark-anti-quark pairs. This leads to the splitting of the colour tube into two and instead of one particle pair two emerge. Most of the attractive force acts now in between these pairs, which results into further splitting of each pair until the energy is so low that instead of creating new particles the created quarks form bound states. The result are two sets of bound states that go approximatively in the direction of the original two quarks. These sets are called jets and represents quarks from the original process. The same thing happens if shortly before or after the creation of two separated quarks a high energetic gluon is radiated from the process. This is called initial state radiation (ISR) or final state radiation (FSR) respectively. If the energy of the gluon is high enough it gets separated and it forms a jet.[15]

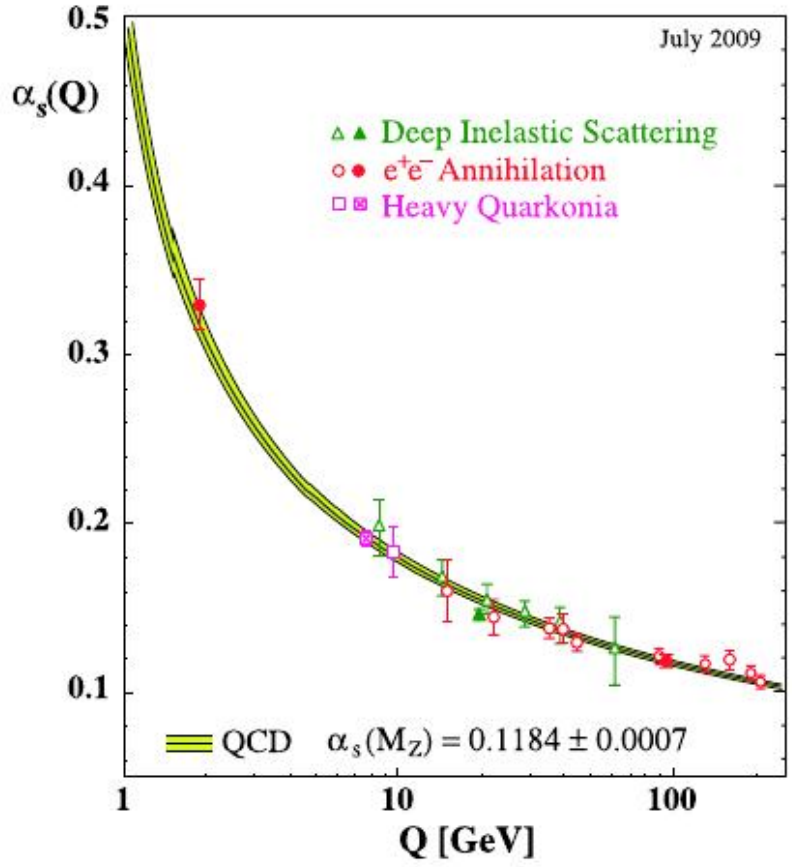

Figure 2.6: Worldwide average of the strong coupling constant α_s as a function of the energy scale Q, published 2009 in [13].

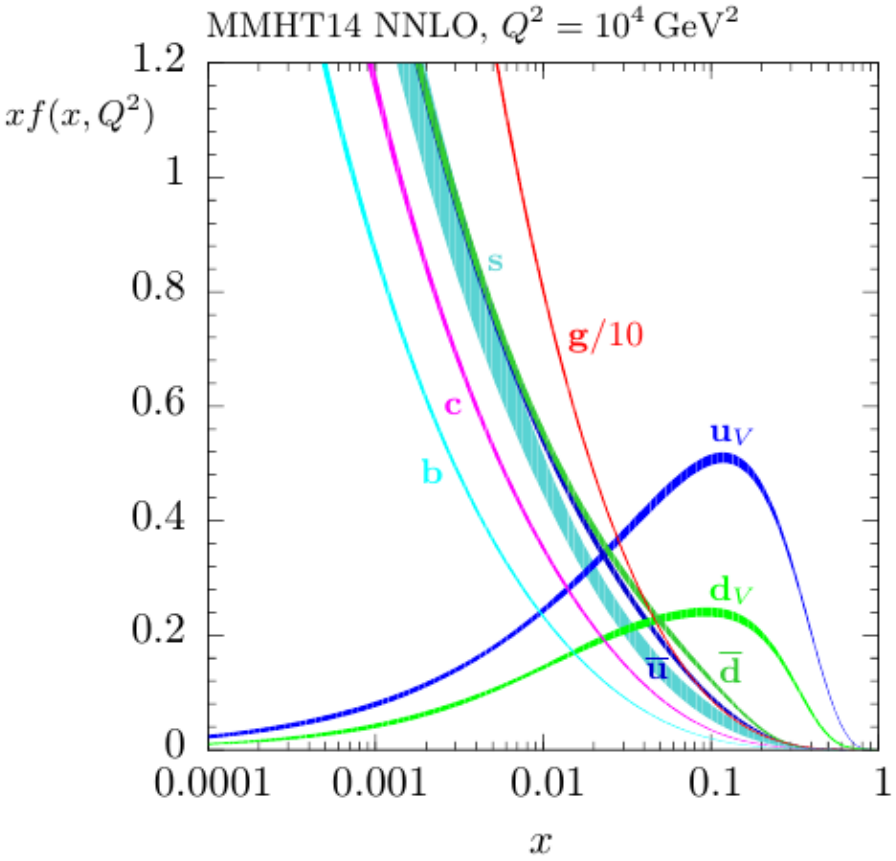

Figure 2.7: Particle density functions evaluated at an energy scale of $Q^2 = 10^4\mathrm{GeV}^2$ as a function of the momentum of the proton carried by this component. The valence quarks are denoted by a small v. Note that the gluon component is scaled down by a factor of 10. [14]

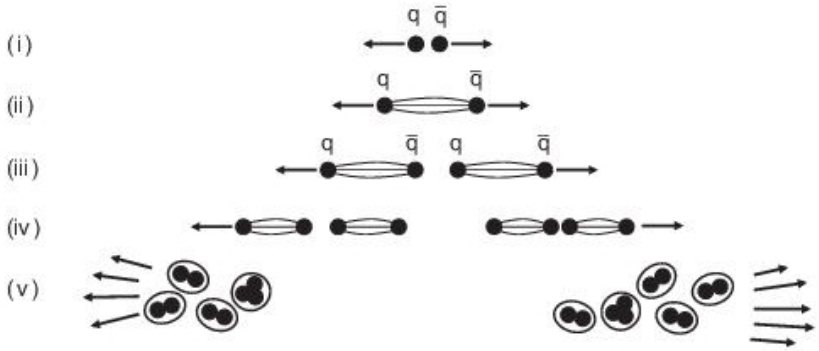

Figure 2.8: Sketch of the formation of a jet. Two quarks get divided and due to the nature of QCD each of them evolves to a jet. For a more detailed description look into section 2.2.1. [3]

CHAPTER 3

Experimental Setup

3.1 LHC

The Large Hadron Collider (LHC) is the world's most energetic hadron-hadron collider[16]. It is located at CERN which is partly in Geneva, but a big part of it is actually in France. It collides mostly protons and is also used for colliding heavy ions. This thesis focuses on proton-proton collisions. In order to accelerate the protons to 6.5 TeV preaccelerators are needed. In figure 3.1 the overall layout of the LHC including the preaccelerators can be seen. Both the preaccelerators and the LHC are explained in the following.

3.1.1 Preaccelerators

Protons are obtained from hydrogen, which consists of one proton as the nucleus and one electron. The hydrogen atoms get stripped by pointing an electron beam on them. These electrons will collide with the electron from the hydrogen atom and left over is a proton with thermal energy. It gets extracted by a negatively charged extraction-electrode. After extraction it has an energy of 9 keV.

The first acceleration step is the use of linear colliders. At the LHC a radio-frequency quadrupole (RFQ) is first used to accelerate the protons to an energy of 750 keV. Through the use of quadrupoles (magnets with 4 poles arranged symmetrically with two positive and to negative poles each arranged opposite of the pole with the same charge) the proton beam also gets focused and divided into bunches. The LINAC2 after it uses cylindrical electrodes with alternating charges in order to always accelerate the next bunch. It accelerates the protons to an energy of 50 MeV which corresponds to a velocity of approximatively 31% of the speed of light.

For higher energies it is more convenient to use circular colliders since protons can travel through them several times. The downside is that those particles have to be forced on a circular course by strong magnetic fields created by dipoles. Also at higher energies charged particles emit bremsstrahlung which goes as m^{-4}. This would cause electrons accelerated to an energy comparable to the energy in the LHC and at a similar radius to emit a large amount of their energy while being bent on the circle. The first LHC circular preaccelerators are the Proton Synchrotron Booster (PSB) and the Proton Synchrotron (PS). They accelerate the protons to an energy of 1.4 GeV and 25 GeV. The PS additionally further divides the 6 proton bunches that it gets from the PSB into 72 smaller ones while there is a gap of 320 ns between the individual bunches. The last preaccelerateor ist the Super Proton Synchrotron (SPS) which accelerates the particles up to 450 GeV from where the bunches get injected into the LHC. [17][18]

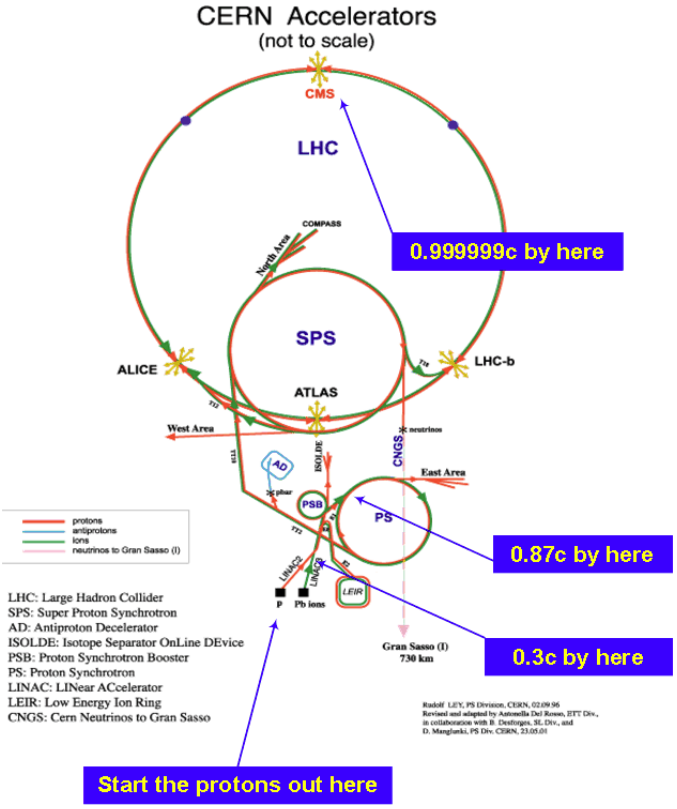

Figure 3.1: Sketch of the LHC and its preaccelerators starting from the LINAC. The beam directions are indicated with arrows. Additionaly to the experiments directly at the LHC other experiments attached to the preaccelerators are shown. [19]

3.1.2 LHC

The LHC is filled with up to 5616 bunches. Half of them run clockwise and the other half run counter-clockwise in a different beam pipe. Currently they get accelerated up to an energy of 6.5 TeV each, achieving an collision energy of 13 TeV. The circumference of the LHC is 26.659 km and it is located underground. In a more detailed look it is not really circular, but composed of eight arcs and eight straight sections. So it looks more like an octagon. In figure 3.2 one can see a sketch of the LHC layout. In the arcs a complicated magnet system is located that bends and focuses the beam. Focusing also takes place in the straight sections. Additionally other utilities can be placed in the straight section. In one straight section the acceleration takes place, in another the beam gets dumped(thrown out of the accelerator). In two straight sections the beams gets further collimated.There also can be crossing points where both beams cross each other and collisions take place. These are the spots of the four experiments ALICE, ATLAS, CMS and LHCb. ALICE is a heavy ion experiment[16], ATLAS and CMS are general purpose detectors and LHCb studies flavour physics (so mostly working with b-quarks)[16].

An important characteristic of accelerators is the possibility of creating events in colliders. It is called luminosity $L = \frac{\dot{N}}{\sigma}$ where σ stands for the cross-section and $\dot{N}$ denotes the event rate of the process. It can also be calculated from the detector accelerator properties: n the number of bunches, N_1, and N_2 the

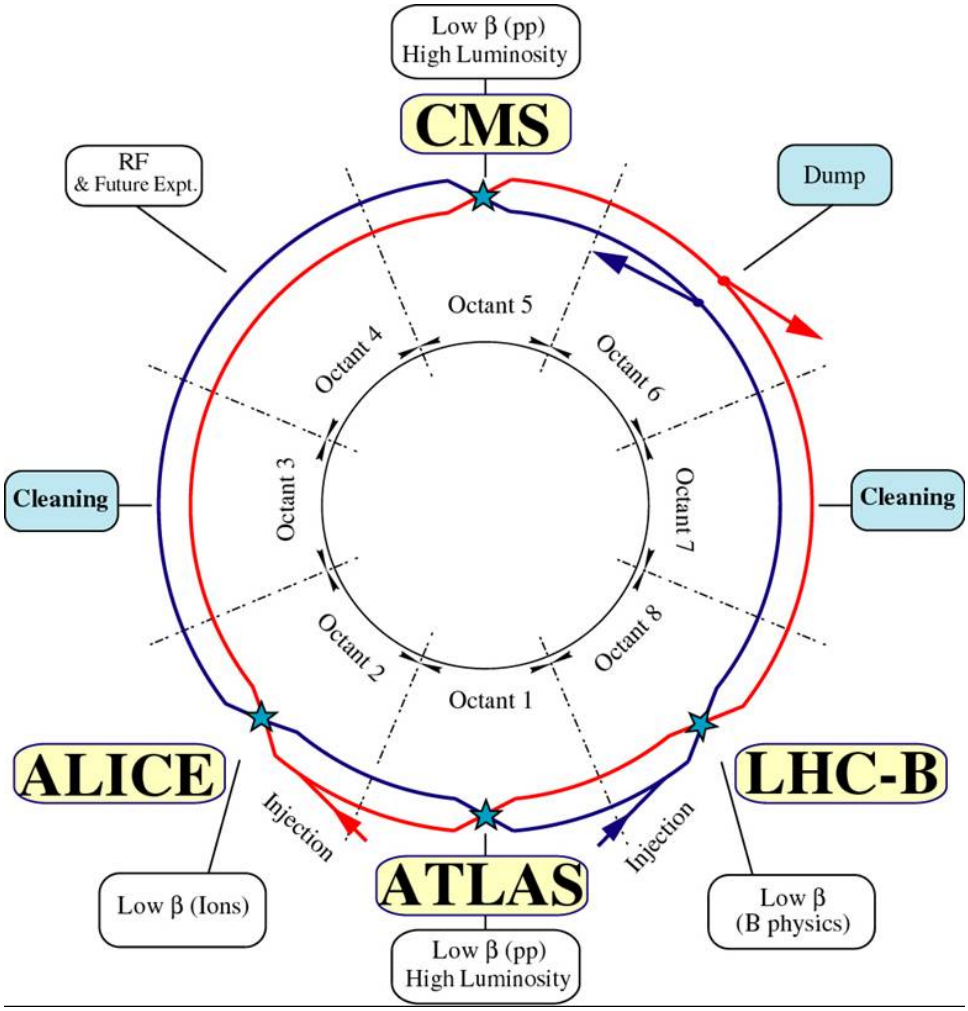

Figure 3.2: Sketch of the LHC ring indicating the position of the experiments and other facilities. RF indicates the Radio Frequency accelerating device.[19]

number of particles in the bunches, the cross-section area of both, A, and the frequency of bunches, f:

$$L = \frac{n \cdot N_1 \cdot N_2 \cdot f}{A} \tag{3.1}$$

The integral of the luminosity over time $\mathcal{L} = \int_0^T Ldt$ the so called integrated luminosity is associated to the number of events that the collider provided in a certain time. In total at ATLAS an integrated luminosity of 38.5 fb^{-1} was delivered by the LHC in 2016 [17, 20].

3.2 ATLAS

The ATLAS detector is one of the two general purpose experiments at the LHC. It is positioned in a cavern directly between both injection points. General purpose experiments are designed to discover and measure particles and their interactions at the highest possible energy. Additionally the ATLAS experiment is designed to measure and store a high number of events that is provided by the LHC and is

needed in order to measure rare processes or more common processes with a better accuracy which could lead to the discovery of new physics. A sketch of the overall detector can be found in figure 3.3. This section is based on [21].

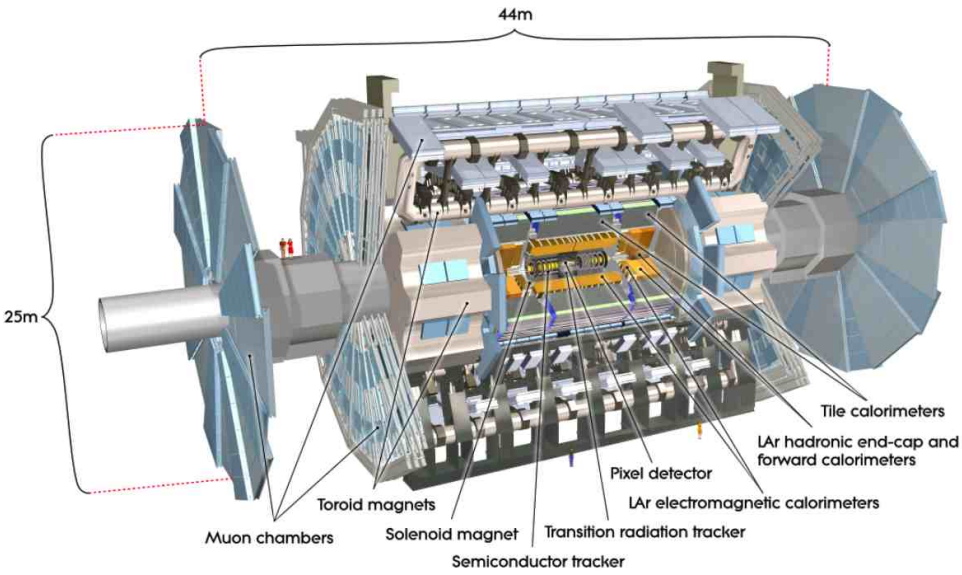

Figure 3.3: Sketch of the ATLAS detector.[22]

Coordinate system

A sketch of the coordinate system ATLAS uses can be seen in figure 3.4. The three axis form a right-handed coordinate system and are defined as follows:

- ***x*-axis**: pointing from the interaction point towards the centre of the LHC
- ***y*-axis**: pointing upwards
- ***z*-axis**: pointing along the beam-line

Thus the transverse plane is perpendicular to the beam axis. The angle in this plane is called ϕ. Another useful angle is θ which is the polar angle starting from the z-axis. Objects measured in the ATLAS detector are generally boosted along the z-axis since the colliding partons do not carry exactly the proton momentum (see section 2.2). Thus it is handy to define a property that only depends on θ and behaves similar to a boost. This property is called pseudorapidity, (η), and it is for massless particles equal the rapidity, (y):

$$\eta = -\ln(\tan(\theta)) \tag{3.2}$$

$$y = \frac{1}{2} ln\left(\frac{E + p_z}{E - p_z}\right) \tag{3.3}$$

where E denotes the energy of the particle and p_z the momentum component along the beam axis. $\eta = 0$ denotes a point that is in the transverse plane of the collision point. So the smaller $|\eta|$ of an object the more central it is.

Distances between two objects are usually measured in the $\eta - \phi$-plane:

$$\Delta R = \sqrt{\Delta\eta^2 + \Delta\phi^2} \tag{3.4}$$

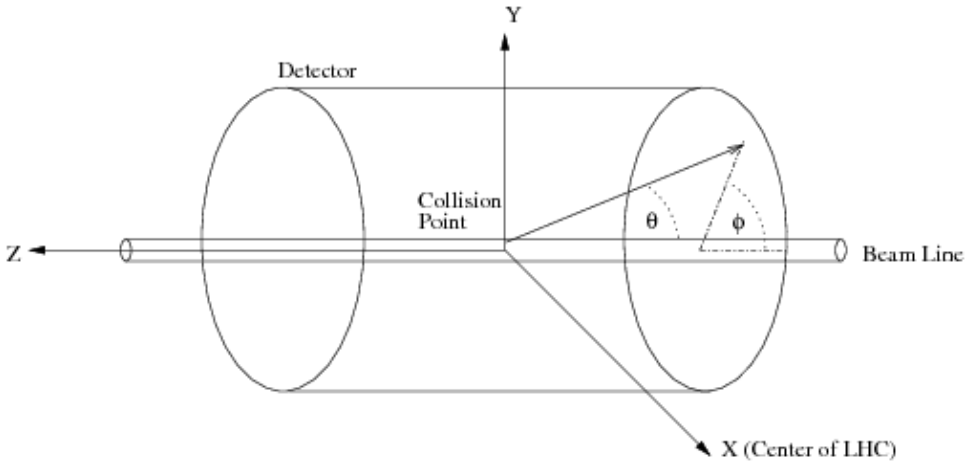

Figure 3.4: Sketch of the coordinate system used in ATLAS. [23]

3.2.1 Magnet system

Magnets in a particle detector are used to bend the track of charged particles. From the curvature of a track the momentum of that particle can be determined using $F = p \times B$. The speed, v, of particles in the detector can be assumed to be close to the speed of light. The strength of the magnetic field, B, is known in detail inside the various parts of the detector. The ATLAS detector uses 3 sets of magnetic fields:

- **Central solenoid:** produces a magnetic field inside the tracking system. The field-lines ideally are parallel to the beam-line and a close to homogeneous field of 2 T is achieved.
- **Muon toroids:** produce magnetic fields in the muon system. The field-lines idealized create a circle in the transverse plane. It is not as homogeneous as the solenoid field but provides a bending strength of 1.5-5.5 Tm in $0 < |\eta| < 1.4$. Similar to the central muon toroids the end-cap toroids produce a magnetic field in the muon end-cap system. At $1.6 < |\eta| < 2.7$ it provides a bending strength of 1-7.5 Tm

A charged particle track that passes the magnetic field produced by the solenoid would be bend in the transverse plane, while a charged particle track passing a toroid produced magnetic field would be bend along the direction of the beam-line.

3.2.2 Inner Detector: tracking system

The tracking system is closest to the beam-line in order to record the path of the produced particles as early and as accurately as possible. Particles leave so called hits in the detectors which can be combined to tracks which resemble the path of the particle through the detector. This is called track reconstruction. It is enclosed in the solenoid (see section 3.2.1) thus the particles tracks are bend. Thus by measuring the track with high precision also the momentum of a particle can be measured precisely. Also the track before the detector can be extrapolated. From this the original vertices are reconstructed.

Silicon detectors

Generally speaking semiconductor detectors are based on the fact that traversing charged particles deposit energy by creating electron-hole pairs in the semiconductor which induce a signal in the electrodes. The obtained information is in which electrode a signal is measured. So the finer the electrode structure is build the higher is the space-resolution of each hit.

Two types of semiconductor detectors are used in ATLAS:

- **Pixel detectors:** four layers of semiconductor detectors with each pixel spreading in $R-\phi$ and z. The smallest have a size of $50\,\mu\text{m} \times 250\,\mu\text{m}$. Alone the pixel detector has approximately 92 million readout channels [24].
- **Semi-conductor tracker (SCT)**: consist of strips each providing position information in just one dimension. By stacking eight of them alternating in either the $R-\phi$ or z direction still four space-points can be obtained. Each strip has a pitch of $80\,\mu\text{m}$. The SCT still has 6.3 million readout channels.

Transition Radiation Tracker (TRT)

Similarly as in silicon detectors traversing charged particles create electron-ion pairs in gases. ATLAS uses straw tube detectors that consist of a gas-filled straw with a wire spanned in the middle. Between the wire and the cylinder a voltage is applied that makes the electrons drift to the wire (anode) while the ions drift to the cylinder (cathode). While drifting the electrons get accelerated and produce more electron-ion pairs what enhances the signal read out. Depending on the voltage the overall behaviour of such gaseous detectors change tremendously. Straw tubes at ATLAS are operated with a xenon–CO_2–oxygen mixture at a voltage of 1.5 kV which results in the signal being proportional to the deposited energy. This enhances the resolution in $R-\phi$. Unfortunately no information about the z component of the interaction is obtained since the tubes are aligned with the beam axis. Between the straws polymer fibres are deposited where additionally high-energetic transition-radiation can be produced if high energetic charged particles pass the border between media with different refraction coefficient. This effect is most prominent for electrons. So if a photon originating in this process deposits its energy in the xenon gas this is a sign that a high energetic electron passed through.[25]

3.2.3 Calorimetry system

The calorimeters are designed to measure the energy of particles and where it is deposited. During the measurement process particles lose their energy by creating a so-called shower. The calorimeters are positioned between the solenoid and the toroid magnets so no dedicated magnetic field is applied here.[26]

Electromagnetic Calorimeter (ECal)

In the ECal an electromagnetic shower is started by photons or electrons[1] and measured. An electron produces photons due to so-called bremsstrahlung while photons can decay into an electron-positron pair in the electric fields of atoms. These two processes happen repeatedly.

Often a combination of active and passive materials is used. In an active material the produced particles produce ionization radiation. In the passive material the shower progresses, so it is designed to allow as many interactions as possible.

[1] electron in this context always includes positrons

ATLAS uses a accordion-like folded structure of liquid argon as active material and lead absorbers as passive material. The electrodes are formed by kapton. This shape makes it possible to cover the whole range in ϕ with all components. The central part covers $|\eta| < 1.475$. An important variable for electromagnetic calorimeters is their depth in radiation lengths. In one radiation length an electron has $\frac{1}{e}$ of its energy left. The ECal at ATLAS reaches 22 radiation lengths.

Hadron calorimeter (HCal)

After the ECal an HCal is located which is designed to measure the energy of hadrons. Several processes are responsible for showers created by hadrons which are measured in the HCal.

1. **High energy cascade:** high energetic particles undergo inelastic scattering with nuclei, hereby part of the nucleus –mostly single protons or neutrons– get accelerated and leave the nucleus

2. **Spallation:** the nuclei got a lot of energy due to the interaction with the primary hadron and the secondary produced hadrons. It emits this energy by emitting further protons, neutrons or even small parts of the nucleus. These have energies of about 100 MeV or higher.

3. **Evaporation:** after the spallation the nucleus is still in an excited state. Depending on the nucleus it emits further parts at an energy of about 2 MeV or even undergoes nuclear fission.

4. **Electromagnetic shower:** the light hadrons that have been produced may decay into photons as for example neutral pions $\pi^0 \rightarrow \gamma\gamma$. Just these get measured in the active part of the calorimeter.

ATLAS uses a hadron calorimeter that is made of a steel absorber and a scintillator as the active material. It consists of one central barrel $|\eta| < 1.0$ and two extended barrels with $0.8 < |\eta| < 1.7$. The length of a hadron calorimeter is measured in interaction lengths which corresponds to the distance after which $\frac{1}{e}$ of the original particles have not interacted. Both the central and the extended barrel contain in total 7.4 interaction length. Because the measured response for the electromagnetic and the hadronic part of the shower are different the response to electrons and the hadrons with the same energy is different and thus the calorimeter is called non-compensating. This leads to the fact that electrons and photons are measured more accurately than hadrons.

3.2.4 Muon system

The muon system consists of several types of gaseous detectors, outlined in section 3.2.2. The basic idea can be extended to so-called multi-wire cPERF-2007-01hambers that contain several wires in one gas volume. This idea is used in the cathode strip chambers (CSC) that are installed in $2.0 < |\eta| < 2.7$. Gaseous detectors with separated volumes (monitored drift tubes) are used in the central region $|\eta| < 2.7$. For triggering purposes fast responding detectors are needed. ATLAS uses resistive plate chambers (RPC) and thin gap chambers (TGC) in the forward region, which are both parallel plate chambers. As the name suggest these gaseous detectors consist of two parallel plates which work as anode and cathode.

3.2.5 Forward detectors

Additional to the central detectors that are positioned cylindrically around the beam the same structure is built up at the endcaps. For some detectors other choices had to be made though:

- **Pixel detector:** three disks of pixel detectors are positioned at each side

- **SCT:** nine disks of SCT modules are positioned at each side
- **TRT:** layers of straw tubes are positioned at each side , the filling is made out of foils though
- **ECal:** two additional end-cap ECal are used that cover $1.375 < |\eta| < 3.2$
- **HCal:** the end-cap hadronic calorimeter consists of two components:
  - **Hadronic end-cap calorimeter (HEC):** is made of liquid argon as an active material and copper plates as the passive material, it covers $1.5 < |\eta| < 3.2$.
  - **Forward Calorimeter (FCal):** it is approximately 10 interaction length deep and covers $3.1 < |\eta| < 4.9$. Liquid argon is again used as the active material while the first module uses copper as passive material, which is optimized for electromagnetic measurements and tungsten for the other two modules which is better for the measurement of hadronic components.
- **Muon system:** has already been discussed in section 3.2.4.

Some additional smaller detectors (LUCID, ALFA, ZDC) are located in the very forward region 17-240 m behind the interaction point. They are mainly used for luminosity measurements.

3.2.6 Trigger system

As seen in section 3.2.2, alone the inner detector produces tremendous amounts of information. This happens at a bunch-crossing rate of approximatively 30 MHz. It is at the current status of computing not possible to store that much information and it is also not wanted to store all of that. In most of the bunch-crossings the protons interact just with low energy with each other, the interesting processes however happen at higher energy. So the trigger system is needed that decides if a process should be stored or not. In ATLAS the trigger system consists of two parts [27]

- **Level-1 (L1)**: makes the decision if an event should be stored in less than 2.5 μs. Therefore it uses just limited detector information and reduces the rate to about 100 kHz. It also defines regions of interest (RoI) in $\eta - \phi$
- **High-Level-Trigger (HLT)**: includes a processing of the data using the full detector information in either the whole event or in the ROIs what takes approximately 200 ms and is performed offline. In this final process the event rate is reduced to about 1 kHz.

In general events are scanned for interesting signals such as particles with high energy.[2] The triggers that require such things are called “raw triggers”. But the number of events that pass these is still too high in some cases. So just every k-th event with that signature is stored, that is called prescaling. k is called the prescale weight or downscale factor. The actual trigger consists of both the raw decision and the prescaling decision, the numbers of events recorded are related as follows:

$$n_{\text{event,actual trigger}} = \frac{1}{k} n_{\text{event,raw trigger}} \tag{3.5}$$

[2] Some events are also stored despite the fact that they contain no signal that causes the trigger to fire. For example the so called zero-bias sample consist of events that happened exactly one accelerator turn after a specific trigger. It is used for example in the random cone method explained in section 4.3.4.

3.2.7 Data storage

The large amount of data recorded by the LHC experiments have to be stored and processed somewhere. This is done using the Worldwide LHC Computing Grid (WLHCCG). The Grid is a worldwide network of servers storing and processing physics data (including simulations) for the four big experiments at the LHC (ALICE, ATLAS, CMS and LHCb). It is composed of thirteen Tier-1 sites connected to CERN with a 10 Gb/s connection which are located worldwide their purpose is storing, distributing and computing to the more spread-out 160 Tier-2 sites.

3.3 MC generators

In order to answer the question if the outcome of an experiment is comparable to what one expects it first has to be simulated based on the principles of our theory. Since the particle physics is based on quantum mechanics it has to be interpreted statistically. In many processes that should be simulated it is desired to simulate when or if a process happens, but only the probability of the process happening is known. Therefore just a statistical prediction can be given. For example it is not possible to simulate when a gluon will be radiated of a quark to form a jet, but it is possible to simulate a large number of jets. If also the probabilities are not known accurately enough results from previous experiments are used to tune them. In this approach for each decision a random number is generated and determines if the process happens in the simulation or not. It is called Monte Carlo (MC) simulation. The simulation of a certain process can be separated into several steps, which can be seen in figure 3.5. Each of them is simulated with the Monte Carlo technique:

1. Incoming particles: both incoming protons contain valence quarks, gluons and sea quarks. At high centre-of-mass energies not whole protons collide but their constituents. The underlying probabilities for each of the constituents are given by PDFs (see section 2.2)

2. Hard scatter (processes of interest): physics process that one wants to study. One example is the scattering of two quarks with high momentum transfer. The underlying probabilities are given by the cross-sections of the process.

3. Decay of short lived particles: particles like the top-quark are short lived. Their decay can be viewed as part of the hard process.

4. Initial State Radiation (ISR): the initial state particles can radiate of gluons. They are modelled by space-like parton showers. Space-like corresponds to $0 > p^2 = E^2 - \vec{p}^2$ where E is the energy and $\vec{p}$ is the three-vector of the particles involved. The sign in p^2 leads to different kinematics in the shower.

5. Final State Radiation (FSR): the particles in the final state can also radiate of gluons. They are modelled by time-like parton showers. Time-like corresponds to $0 < p^2$.

6. Multi Parton Interactions (MPI): since a proton consists of more than one parton also more then two partons can collide when two protons collide. These additional interactions also have to be modelled.
   - MPI radiation: Also in MPI ISR or FSR can occur.

7. Hadronization: if a parton is separated from the rest of the interaction there spreads a colour tube which will break and produce more quarks until hadrons are formed.

8. Hadron decay: the produced hadrons are often unstable and decay further.

9. Detector: particles traverse through the detector and are measured. This may interplay with the hadron decay if the produced hadrons are stable enough to decay inside the detector.

Simulated events that undergo every step but the last are called truth events. Often the collection of stable particles so particles that not decay for at least 30 ps is called truth particle collection[28]. Especially the hadronization step is not easily solvable from first principles. There are different ways to approach this. For more information see [29]. In this thesis Pythia8[30] will be used as a general MC generator. The detector simulation is done by Geant4 [31].

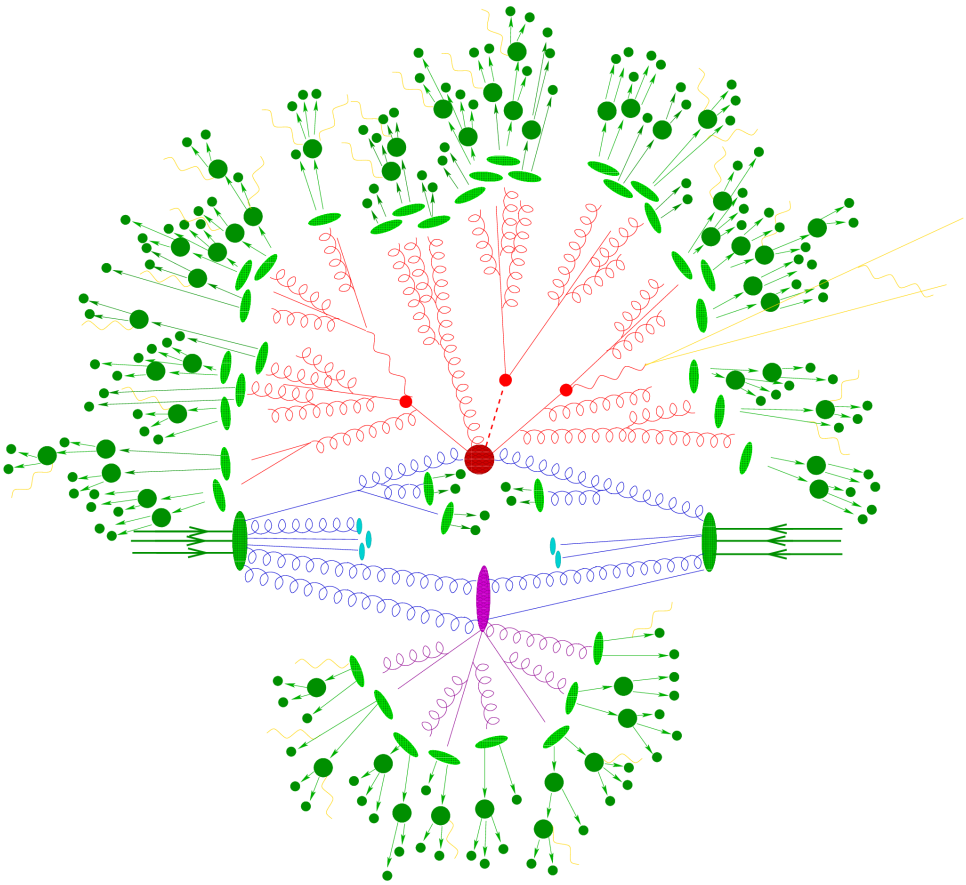

Figure 3.5: Sketch of the different steps in a Monte Carlo simulation of one event. The green blobs coming from left and right represent the incoming protons. The cyan blobs stand for the not interacting partons. The hard scattering event is represented by the big red circle. Directly below it an example for ISR can be seen that produces particles. From the main event four particles are created that are indicated by red lines and curls. From left to right a quark, a gluon, a scalar and a second quark. The quarks and the gluon radiate further gluons. The small red circles represent further decay of the quarks and the scalar. The produced quarks and bosons eventually decay further into quarks or leptons and radiate of further gluons. Every gluon may radiate even further gluons. The light green blobs represent recombined hadrons. They decay of these hadrons is represented by dark green circles and green arrows. Yellow curved lines represent the radiation of soft gluons. On the lower half a big violet blob can be seen that represents a MPI. Associated to it is the production of further hadrons following the same steps as the main event. [32]

3.3.1 Pile-up

An optional step that can be simulated is the so-called pile-up. It describes additional collisions that are recorded with the main event. It is divided into in-time pile-up that originates in additional interactions that occur in the same bunch-crossing and out-of-time pile-up that originates in interactions from other bunch crossings. As for the MPI pile-up events are normally assumed to be of very low $p_{\mathbf{T}}$.

CHAPTER 4

Jets at ATLAS

4.1 Jet Definiton

As described in section 2.2.1 jets are a bundle of particles that originate from the hadronization of a quark or a gluon. The first challenge is to combine the input objects into one object that resembles the properties of the original particle therefore one uses jet algorithms.

4.1.1 Jet algorithm

A jet algorithm is the procedure of recombining measured objects into one. There are several requirements a good jet algorithm should fulfil:

- Order independence: the jet algorithm should be applicable to objects of different orders i.e. tracks and clusters as well as hadrons.
- Collinear safety: colinear splitting of a particle should not change the number of jets
- Infrared safety: the number of jets should also be conserved if a soft gluon is emitted, if this is not fulfilled the emittance of a soft gluon could lead to the merging of two jets.
- Insensitivity to longitudinal boosts: as described in section 3.2 the particles in the final state still have an unknown boost along the z-axis, the algorithm should not be sensitive to this.
- Boundary stability: the kinematic boundaries of the reconstructed jet should not be sensitive to details like the number of particles.
- Insensitivity to the underlying events: as described in sections 3.3 and 3.2 simultaneously to each interesting collision other collisions with lower $p_{\mathbf{T}}$ happen and the remnants are also recorded. The reconstructed jets should not be affected by them.
- Insensitivity to hadronization: the details of the hadronization model should not impact the reconstructed jet, but ideally the originating jet is reconstructed.
- Insensitivity to detector effects: as the hadronization also the specifics of the measurement procedure should not impact the reconstructed jet.
- Preservation of jet properties: properties as the angular direction and the energy of the reconstructed jet should be as close to the original jet as possible.

- Reconstruction efficiency: all objects should be used for the output, i.e. every jet should be reconstructed (if a jet is not seen at all it is called a "dark jet").

- Easy implementation: in the reconstruction which even takes place during the triggering the jet algorithm has to be run often; hence it should be easy and fast to compute, the calculation time should not depend to much on the number of input objects.

The order independence, boundary stability and insensitivity to longitudinal boosts can be achieved by using four-vectors and the rapidity (instead of the pseudorapidity) to define the particles and recombine them by adding the four vectors. To fulfil the other requirements several approaches were tried in the past. One approach uses cones that are defined around a high $p_{\mathbf{T}}$ seed. Obviously these cone-algorithms have problems with the collinear safety. To overcome this problem a so-called seedless infrared safety cone algorithm (SISCone) has been developed in 2007. Another problem is the possibility of producing "dark jets" which do not occur in sequential algorithms.

Sequential jet-algorithms sequentially combine objects until a certain threshold requirement is fulfilled. They are in general easy to implement and fast. The basic procedure is described in the following:

1. a distance d_{ij} between each object is calculated, this distance in general does not only depend on the geometry but also on the kinematic properties:

$$d_{ij} = \frac{\Delta R_{ij}^2}{R} \min\left(p_{T,i}^{2x}, p_{T,j}^{2x}\right) \tag{4.1}$$

   where R is a parameter that determines the size of the recombined jets, $\Delta R = \sqrt{\Delta y^2 + \Delta\phi^2}$, $p_{\mathbf{T}}$ is defined as in section 3.2, x is a parameter that characterizes different jet algorithms

2. calculate the distance between each object i and the beam:

$$d_{iB} = p_{T,i}^{2x} \tag{4.2}$$

3. choose the minimal value out of all d_{ij} and d_{iB}

4. if the minimal value is d_{ij} combine objects i and j, if it is d_{iB} declare the jet as final and remove it from the list

5. repeat the process with one input object fewer

This procedure runs until every object is taken out and all final jets have been obtained.

Most widely used are three sequential jet algorithms. The Cambridge-Aachen algorithm uses $x = 0$ which makes the algorithm insensitive to the kinematic of the constituents. It is especially useful for small jets that are part of a bigger jet which may originate from a heavy boosted object that decayed further, the so-called constituent jets. If $x = 1$ the algorithm is called the k_T algorithm. This algorithm prefers to combine objects with small momenta first. In contrast the anti-k_T algorithm ($x = -1$) preferably combines objects with large momenta. Nowadays this algorithm is widely used for general purpose experiments. It provides a circular area in the $\eta - \phi$ plane that simplify the method to reduce the pile-up contribution. A comparison between the performance of the three described algorithms can be found in figure 4.1. The parameter R determines how big the jets grow, the bigger it is the higher is the probability to merge two jets. The smaller it is the higher is the probability to miss constituents that belong to the

original particle. The standard ATLAS jet algorithm is the anti-k_T algorithm with the parameter $R = 0.4$[1]. They are reconstructed using the *FastJet*[33] algorithm [34]. In general there is no ideal jet algorithm and there will always be uncertainties associated to the jet reconstruction. They are often referred to as out-of-cone (OOC) uncertainties because they mainly occur if the wrong or not all particles are combined into the jets.[15, 33, 35]

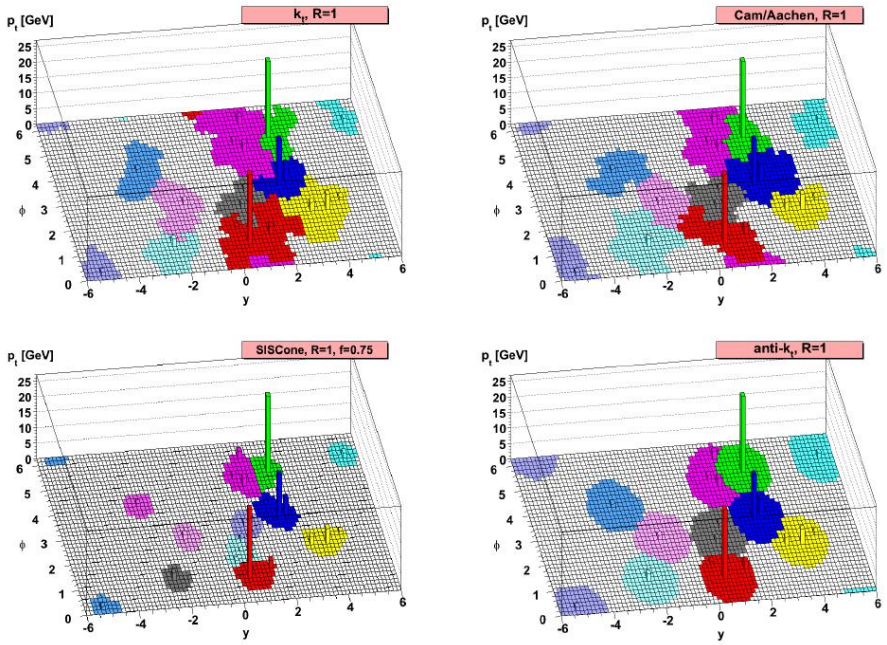

Figure 4.1: Plot of the jet areas in $\eta - \phi$ that are associated to jets calculated with different jet algorithms. In the third axis the $p_{\mathbf{T}}$ of the input particles can be seen. The ghost-association method (see section 4.2.2) was used to obtain the jet areas. [35]

4.1.2 Topo-clusters

Clusters are the way calorimeter-signal are used as input for jet algorithms. They combine the information of several cells in order to be able to treat the collected information similar to the response of a single particle. Also they help to differentiate real signals from noise. Of course the clusters could also be just part of the shower of one particle or of several particles or even a combination of both.

The basic discriminant for each calorimeter cell in this process is the cell signal significance $\varsigma^{\mathrm{EM}}_{\mathrm{cell}}$ which is the ratio of the cell signal $E^{\mathrm{EM}}_{\mathrm{cell}}$ to the average expected noise in this cell $\sigma^{\mathrm{EM}}_{\mathrm{noise,cell}}$:

$$\varsigma^{\mathrm{EM}}_{\mathrm{cell}} = \frac{E^{\mathrm{EM}}_{\mathrm{cell}}}{\sigma^{\mathrm{EM}}_{\mathrm{noise,cell}}} \tag{4.3}$$

Both are calculated the electromagnetic (EM) scale that corresponds to the energy deposited by electrons and photons as described in section 3.2.3. Each topo-cluster consists of a seed, a growing region and a periphery:

[1] In principle a larger R would lead to a higher probability of associating all objects to the jet that originate from it. On the other hand more energy originating from pile-up gets added to the jet.

- **Primary seed:** each cell that fulfils $\varsigma_{\text{cell}}^{\text{EM}} > S$ is a primary seed and has a protocluster assigned to it.
- **Growing region:** cells that are neighbours of a primary seed and fulfil $\varsigma_{\text{cell}}^{\text{EM}} > N$ are added to the protocluster, also their neighbours that fulfil the same condition are added and so forth.
- **Merge:** if a neighbouring cell is a seed cell both protoclusters are merged.
- **Periphery:** cells that are neighbours of cells in the protocluster and fulfil $\varsigma_{\text{cell}}^{\text{EM}} > P$ are added to the protocluster.

S, N and P correspond to thresholds optimized for the clustering algorithm. Neighbouring here corresponds to adjacent cells in the same layer or cells that overlap in $\eta - \phi$ and are in an adjacent layer. If the clusters are to big important substructure may get lost so if a cluster has more than two maxima [2] it is split between the signal peaks that correspond to this maxima. An example of the formation of topological clusters can be found in figure 4.2.

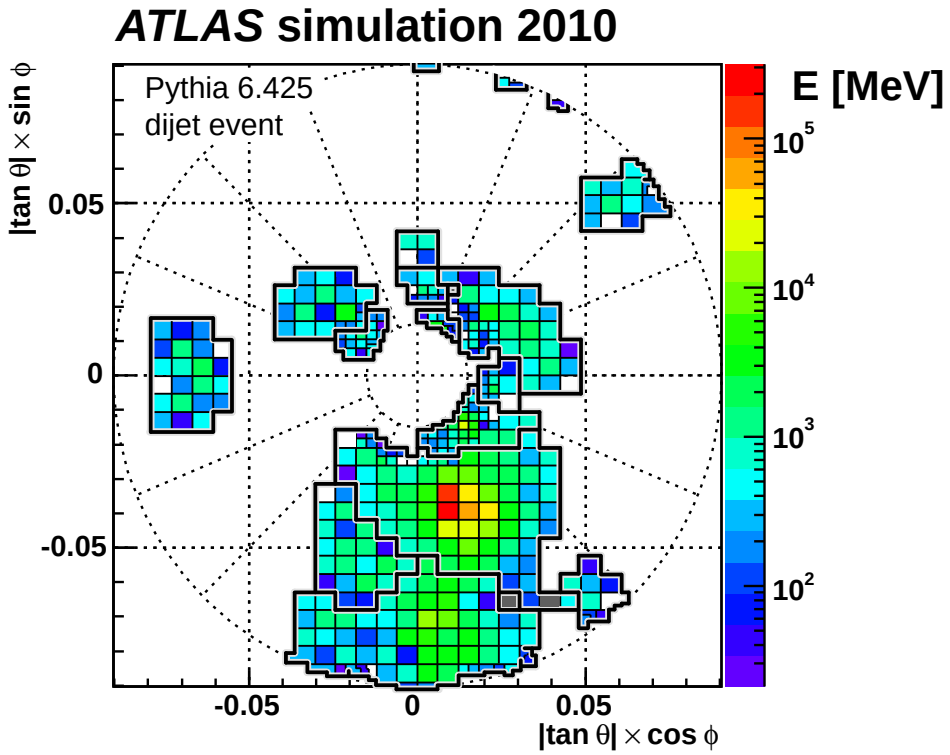

Figure 4.2: Example of ATLAS topo-clusters. Each box represents a calorimeter cell and its colour represents the energy measured in it. The thicker black lines represent the borders of the topo-clusters. Cells with an energy above the threshold that have not been associated to topo-clusters are not shown.[36]

Local hadronic calibration

The Local Hadronic Cell Weighting (LCW) is applied to each cluster in the so-called LC-weighted collections. It is designed to compensate for several sources of possible mis-calibration:

[2] A maximum is defined as a cell that has at least four neighbours, none of them having a higher energy than this cell. Additional $E_{\text{cell}}^{\text{EM}}$ has to be at least 500 MeV.

- **Calorimeter response to hadrons:** as described in section 3.2.3 the calorimeter response is calibrated to the response of electrons and photons, the response to hadrons is known to be smaller.
- **Clustering losses:** clusters can miss energy that should be part of the cluster but is not because of the clustering scheme.
- **Dead material losses:** not all energy of a particle is measured in the calorimeter but some is deposited in dead material in front of the calorimeter or even between calorimeter cells and inside a cell for example in the readout system.

The first step of the calibration is the calculation of a probability $\mathcal{P}_{\text{clus}}^{\text{EM}}$ for each cluster of originating from an electromagnetic shower . It determines the strength of the further corrections, since they are typically smaller for electromagnetic showers. An obvious example for this is the calibration to a hadronic scale. The weight for each cell in the cluster is in this case calculated as following:

$$w_{\text{cell}}^{cal} = P_{\text{clus}}^{\text{EM}} \cdot w_{\text{cell}}^{\text{EM-cal}} + \left(1 - P_{\text{clus}}^{\text{EM}}\right) \cdot w_{\text{cell}}^{\text{had-cal}} \tag{4.4}$$

Where $w_{\text{cell}}^{\text{em-cal}} = 1$ in case of the hadronic calibration and $w_{\text{cell}}^{\text{had-cal}}$ denotes the correction obtained for hadronic showers. This procedure is repeated for all corrections. In the end the energy of the cluster is corrected by the multiplicated weight for each step:

$$E_{\text{clus}}^{\text{cal}} = \sum_{i \in \text{clus}} w_{\text{cell},i}^{\text{cal}} \cdot E_{\text{cell},i}^{\text{cal}} \tag{4.5}$$

More details details about the LCW can be found in [36].

4.1.3 Particle Flow

As seen in the previous section topo-clusters just use the information obtained in the calorimeters, but tracking information is available and could provide a lot of additional information. The technique that combines information from both systems is called Particle Flow (PFlow). It combines tracks and clusters to so-called PFlow-objects. Since the information collected in the tracking system has a better resolution at low $p_{\mathbf{T}}$ it is used preferably. Double counting a particle that left a track and energy in the calorimeter has to be avoided. Therefore the energy that this particle deposited has to be subtracted from the closest cluster.[3] Additionally the deposited energy has to be at least 10% of the track $p_{\mathbf{T}}$ and $\Delta R'$ is at most required to fulfill $\Delta R' < 1.64$. If the energy is spread through several topo-clusters all clusters fulfilling $\Delta R_{\text{clus,track}} < 0.2$ are matched to the track.

Unfortunately one cluster does not always contain the energy of only one particle. To avoid subtracting also the energy of nearby neutral particles the subtraction is performed cell-by cell. A sketch of this can be found in figure 4.3. It includes also a further step called the "remnant removal" where cells belonging to the track which were not subtracted and have $E_{\text{cell}} < 1.5\sigma(E_{\text{dep}})$ get removed. As an input for the jet algorithm only objects originating from the primary vertex are used. This requires $|z_0 \sin\theta| < 2\,\text{mm}$ for tracks. z_0 is here the distance along the beam axis to the hard scatter vertex (definition in section 4.2.1). Clusters are just corrected back to this hard scatter vertex. For more details on Particle Flow see [37].

[3] Closest is in this context given by

$$\Delta R' = \sqrt{\left(\frac{\Delta\phi}{\sigma\phi}\right)^2 + \left(\frac{\Delta\phi}{\sigma\phi}\right)^2} \tag{4.6}$$

in the coordinate system defined in section 3.2. σ_ϕ and σ_η represent the width of the cluster w.r.t. the associated angle.

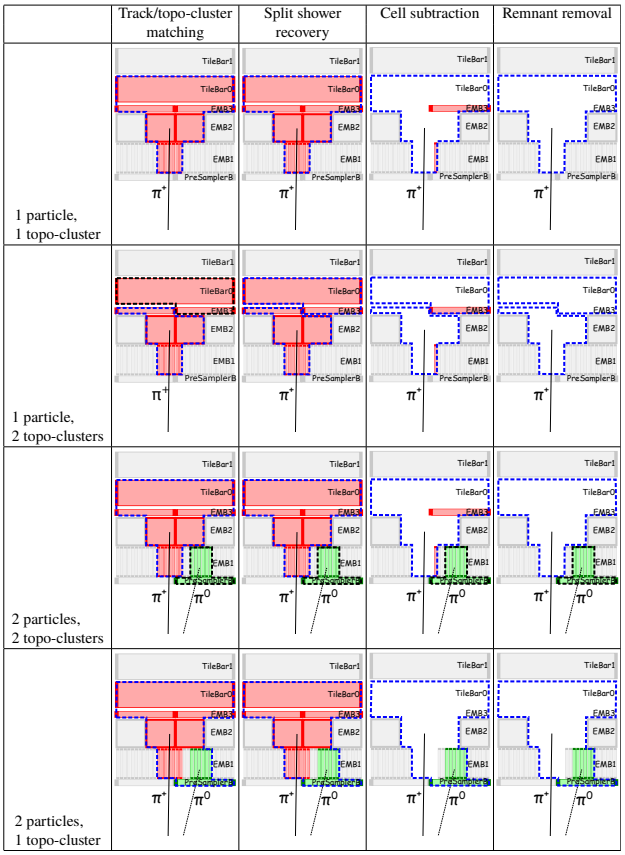

Figure 4.3: Sketch of the cell removal procedure for different configurations. The energy in the cells marked as red has been deposited by a charged pion that left a track in the tracking system. The energy in the cells marked as green had been deposited by a neutral pion that did not leave a track. Thus the first should be removed while the second should be left.[37]

4.2 Jet calibration

As described before jets are quite complicated objects. So the measurement and reconstruction procedure is not simple. This leads to not ideal measurements. In order to correct for possible errors or missing information jets get calibrated before they are used in analysis. This section is based on [28].

4.2.1 JVT and origin correction

Origin correction

In general the direction of an object is based on two points: the origin and the endpoint which is in this context the area where a jet is measured. The obvious choice for the energy is the centre of the detector which is also used to define the origin of the topo-clusters used to obtain the jet. However, the area where the collision takes place is 40-55 mm long (2012 [28]) so this assumption is not completely correct. A better definition of the origin of an event is the point which has the highest $\sum p^2_{T,\text{tracks}}$, where only tracks with $p_\mathbf{T} > 400\,\text{MeV}$ are counted. Jets combined from topo-clusters are corrected back to this point by recalculating the 4-vector to this origin while keeping the energy constant. PFlow jets do not need to be corrected since they rely on input objects that already have been corrected to the origin (see section

4.1.3).

JVT

The Jet Vertex Tagger (JVT) technique uses a discriminant calculated for each jet individually and gives a probability for the jet to originate from the hard scatter vertex or from a pile-up vertex. It is based on the fraction of tracks in a jet that belong to the primary vertex (corrJVT) and the fraction of $p_{\mathbf{T}}$ in a jet that originates from tracks from the primary vertex (R_{pT}). From this a 2-dimensional likelihood is calculated via a machine learning technique that is called k-nearest-neighbour algorithm. So for each jet a JVT weight is calculated which corresponds to the probability for the jet to originate from the hard scatter vertex. [38]

4.2.2 Pile-up corrections

4.2.3 Jet area based pile-up correction

Pile-up is believed to basically add a uniformly distributed amount of energy in the detectors. That increases the $p_{\mathbf{T}}$ of reconstructed jets. Therefore this pile-up contribution is subtracted using the following formula:

$$p_T^{\text{corr}} = p_T^{\text{const}} - \rho \cdot A - \alpha \cdot (N_{PV} - 1) - \beta \cdot < \mu > \tag{4.7}$$

Here p_T^{const} denotes the jet $p_{\mathbf{T}}$ before the correction. The first term corrects the mean pile-up contribution. It is calculated by multiplying the medium energy density of the event ρ with the active area of the jet A. [4] After this corrections still a dependency on pile-up is seen. Therefore two residual corrections are performed: one as a linear function of the number of primary vertices[5] and one as a linear function of $< \mu >$, the average numbers of interactions per bunch crossing. The factors α and β are obtained from MC simulations.

4.2.4 MC Jet Energy scale

The jet energy scale (JES) correction is applied based on Monte Carlo simulated events. It relates the energy of the reconstructed jet to the energy of the truth jet.

$$\text{JES} = \frac{p_{\text{T, data/MC}}}{p_{\text{T,truth}}} \tag{4.8}$$

The factor is calculated for different $p_{\mathbf{T}}$ and η using isolated jets[6] after origin and pile-up correction. The inverse of the jet calibration is called average energy response.

[4] ρ is calculated using jets obtained from a k_T algorithm with $R = 0.4$. It is defined as the median of the energy density $\frac{p_{\text{T}}}{A}$ of these jets. A is calculated with a so-called ghost matching algorithm. Therefore low $p_{\mathbf{T}}$ ghost particles are added uniformly in the $\eta - \phi$ plane and the area of a jet is defined as the area where those ghost particles are recombined into the jet [33].

[5] $N_{PV} - 1$ because there has to be at least one true primary vertex

[6] Isolated jets are defined as jets where no jet with $p_{\mathbf{T}} > 7\,\text{GeV}$ lies within a certain area around the jet. This area is chosen as a cone of $\Delta R = 1.5R$ for reconstructed jets and $\Delta R = 2.5R$ for truth jets.

4.2.5 Global sequential correction (GSC)

After the JES correction additional corrections are applied, while the mean jet energy response is left unchanged. It corrects the energy based on

1. the fraction of energy that is deposited in the first layer of the tile calorimeter to account for the punch through effect in the ECal (see section 3.2.3)
2. the fraction of energy that is deposited in the third layer of the ECal also to account for the punch through effect in the ECal (see section 3.2.3)
3. the number of tracks associated to the jet with $p_{\mathbf{T}} > 1\,\text{GeV}$
4. the average distance between those tracks weighted by $p_{\mathbf{T}}$ and the jet axis in the $\eta - \phi$ plane
5. the activity in the muon spectrometer behind the jet to account for the punch through effect in the HCal

Points 3 and 4 are connected to the fact that quark and gluon initiated jets have a different ratio of high to low energetic constituents.

4.2.6 in situ JES

Several residual corrections are applied to data in order to account for differences between the energy response in Monte Carlo and data. They are applied one after the other:

η-intercalibration

The η-intercalibration is based on balancing two jets in the transverse plane. It is used to calibrate the jets w.r.t. a central reference region. The quantity used is the asymmetry:

$$\mathcal{A} = \frac{p_T^{\text{probe}} - p_T^{\text{ref}}}{\overline{p_T}} \tag{4.9}$$

$$\left\langle \frac{p_T^{\text{probe}}}{p_T^{\text{ref}}} \right\rangle = \frac{2 + \langle \mathcal{A} \rangle}{2 - \langle \mathcal{A} \rangle} \tag{4.10}$$

where p_T^{probe} is the $p_{\mathbf{T}}$ of a jet in the (forward) region being probed and p_T^{ref} is the $p_{\mathbf{T}}$ of a jet in the (central) reference region. $\overline{p_T}$ is the average between the leading and the subleading jet $p_{\mathbf{T}}$.

Boson+jet

This step is based on balancing a jet against a boson. It is either a Z-boson decaying into $\mu^+\mu^-$ or e^+e^- or a photon. There are two ways of applying it: one uses the direct balance method where the jet is directly balanced against the $p_{\mathbf{T}}$ of the reference object into the direction of the jet:

$$p_T^{\text{ref}} = p_T \cdot \sin(\phi_{\text{ref,jet}}) \tag{4.11}$$

The other method uses the missing projectile fraction $\mathcal{R}_{MPF}$ which is calculated as the ratio between the reference jet and the full hadronic recoil of the event. Because the number of recorded events for this techniques has to be high enough the boson+jet calibration is limited to a range of 20 - 950 GeV.

Multijet balance

In the multijet balance a high $p_{\mathbf{T}}$ jet is balanced against a system of lower $p_{\mathbf{T}}$ jets, that previously have been calibrated with the boson+jet method. Therefore it can be used to calibrate jets in a range between 300 GeV and 2 TeV.

4.3 Jet energy resolution

The jet energy resolution (JER) gives the precision of the jet energy measurement and thus it is an important input to analysis. The precision depends on the $p_{\mathbf{T}}$ so the JER is usually denoted as $\frac{\sigma}{p_{\mathbf{T}}}$. It is calculated as a function of $p_{\mathbf{T}}$ and η. There are basically two ways to determine the JER. For both the basic idea is that two objects ideally should be balanced in the transverse plane. Sources for imbalance could be:

- initial state radiation;
- final state radiation;
- dead material in front of the detector;
- dead material in the detector;
- the energy of a jet was not completely measured in a detector "punch-through";
- miscalibration of a jet due to the fact that the calorimeter response is measured for electrons and photons;
- energy is deposited under the noise threshold;
- energy is misidentified as coming from pile-up;
- errors from the jet algorithm.

From these not all are counted under sources for jet energy resolution. The first two items ISR and FSR are physics effects and thus do not contribute to the precision with which the energy of a jet can be measured. The last item is on one hand part of our procedure, but on the other hand it is not part of the measurement itself and thus contains no information about the detector. Also it is not contained in the balance of a jet against a boson, since this procedure corrects to how well a jet is measured w.r.t. a truth jet. Clearly also a truth jet can suffer from these errors. All other imbalances listed above are seen as sources for the jet energy resolution. They all have been accounted for on average, but the width of the distributions gets measured in the JER.

4.3.1 Direct balance

The direct balance method can be obtained from different di-object systems and can be applied in different $p_{\mathbf{T}}$ regions.

Z+jet

As for the direct balance method in the in situ calibration a well measured Z-boson is balanced against a jet. The Z-Boson either decays via $Z \to \mu^+\mu^-$ or via $Z \to e^+e^-$. The distributions in the $p_{\mathbf{T}}$-balance are then fitted with a Gaussian and the σ of the fit is used to determine the JER ($\frac{\sigma}{p_T}$). Because enough events with Z-bosons have to be produced this method is just derived for 17 - 260 GeV jets.

γ+jet

The γ+jet method works similarly, just that the reference object is a photon. From the number of events containing this kind of signature just a small fraction is recorded at low $p_{\mathbf{T}}$, also it is not easily distinguishable from dijet events. At high $p_{\mathbf{T}}$ there are basically not enough events produced. Thus this method is is just used to derive the JER for jets with $25\,\text{GeV} \leq p_{\mathbf{T}} \leq 800\,\text{GeV}$.

Dijet balance

A method to obtain the JER up to high $p_{\mathbf{T}}$ is using an event with a balanced dijet system. As described earlier in section 4.2.6 an asymmetry can be derived for dijet systems. Assuming Gaussian distributions the width σ of this distribution can be written as:

$$\mathcal{A} = \frac{p_T^{\text{probe}} - p_T^{\text{ref}}}{0.5(p_T^{\text{probe}} + p_T^{\text{probe}})} \tag{4.12}$$

$$\sigma(\mathcal{A}) = \frac{\sqrt{2\sigma\left(p_T^{\text{ref}}\right)^2 - 2\sigma\left(p_T^{\text{probe}}\right)^2}}{\overline{p_T}} \tag{4.13}$$

$$\frac{\sigma(p_{\mathbf{T}})}{p_{\mathbf{T}}} = \frac{\sqrt{\sigma\left(p_T^{\text{ref}}\right)^2 - \sigma\left(p_T^{\text{probe}}\right)^2}}{\overline{p_T}} = \sqrt{2}\sigma(\mathcal{A}) \tag{4.14}$$

So the JER is obatined from the width of the asymmetry distribution.

4.3.2 Bisector method

Another method to obtain the JER from a dijet system is the bisector method. It is a geometric approach to separate particle-level from detector-level contributions to the transverse momentum imbalance in dijet events. Thus it specifically accounts for the ISR being not a part of the JER and thus is expected to give a resolution that is a bit lower than the direct balance dijet method.

Coordinate system

The bisector method coordinate system is defined on the dijet system in the transverse plane. In figure 4.4 a sketch can be seen that shows the vectors representing the $p_{\mathbf{T}}$ of the leading and the subleading jet as well as the α-axis (blue) and the β-axis (violet). The α-axis is defined as the bisector of the two jet vectors. The β-axis is perpendicular to it. This defines a coordinate system that does not rely on the $p_{\mathbf{T}}$ of the used jets. Also it provides a definition for "in the direction of the jet axis" which is the β-axis.

Methodology

To get the imbalance in each direction the imbalance vector $p_{T,\text{add}}$ is projected onto the axes:

$$\vec{p}_{T,\text{add}} = \vec{p}_T^{\,\text{leading jet}} + \vec{p}_T^{\,\text{subleading jet}} \tag{4.15}$$

$$p_T^{\alpha} = p_{T,\text{add}} \sin(\gamma) \tag{4.16}$$

$$p_T^{\alpha} = p_{T,\text{add}} \cos(\gamma) \tag{4.17}$$

where γ denotes the angle between α and the imbalance vector. A sketch of this can be seen in figure 4.5.

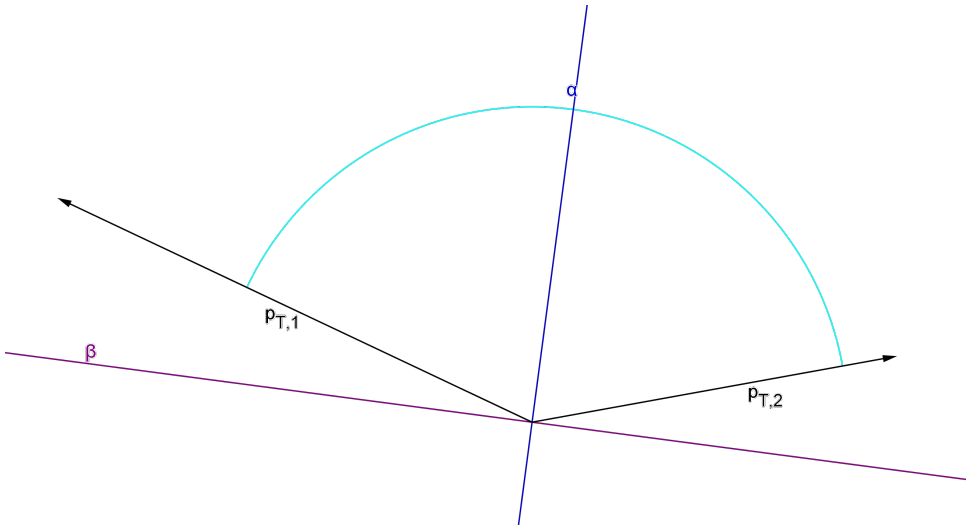

Figure 4.4: Sketch of the bisector coordinate System. It is created in the transverse plane. α goes into the direction of the bisector of both jets and β is perpendicular to it.

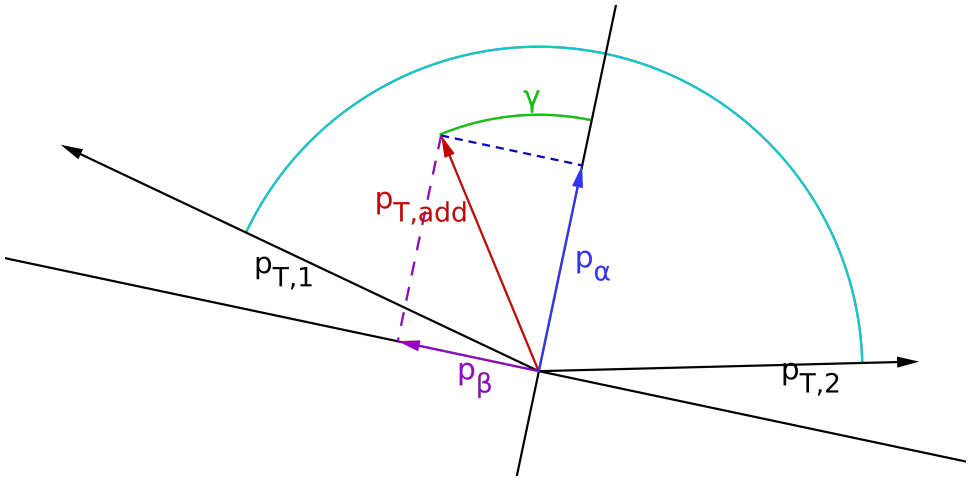

Figure 4.5: Sketch of the bisector system. It is created in the transverse plane. α goes into the direction of the bisector of both jets. β is perpendicular to it.$\vec{p}_{T,\text{add}}$ is the imbalance vector. γ is the angle between $\vec{p}_{T,\text{add}}$ and the bisector. With the help of it $\vec{p}_{T,\text{add}}$ is projected onto α and β.

For both p_T^α and p_T^β an uncertainty σ_α, σ_β can be derived. These uncertainties contain different contributions. Some imbalances originate from processes that happen before the formation of jets, the so-called particle level. The biggest contribution to it is ISR. General speaking the imbalances at particle level (P) are isotropic in the transverse plane.

$$\sigma_\alpha \approx \sigma_\beta \tag{4.18}$$

On the other hand there are also imbalances that originate in the formation of jets. Especially mismeasurements in the detector lead to fluctuations. These fluctuations mostly change the length of the $p_\mathbf{T}$-vectors. Since our coordinate system is independent of this the contribution to σ_α are very small and it can be approximatively assumed that they only contribute to σ_β.

The $\vec{p}_{T,\text{add}}$ that is measured in the end includes both particle and detector level imbalances. It is also called the $\vec{p}_{T,\text{add}}$ at detector level, D. For the projection along β ($p_{T,\beta}$) holds:

$$\begin{aligned} p_{T,\beta}^D &= p_{T,1,\beta}^D - p_{T,2,\beta}^D && (4.19)\\ &= \left(p_{T,1,\beta}^D - p_{T,1,\beta}^P\right) - \left(p_{T,2,\beta}^D - p_{T,2,\beta}^P\right) + \left(p_{T,1,\beta}^P - p_{T,2,\beta}^P\right) && (4.20) \end{aligned}$$

For each part of equation 4.20 the variance can be calculated (here for the case that both jets are in the same pseudorapidity region):

$$\begin{aligned} \text{Var}\left(p_{T,\beta}^D\right) &= {\sigma_\beta^2}^D \\ \text{Var}\left(p_{T,1,\beta}^D - p_{T,1,\beta}^P\right) &= \text{Var}\left(\left(p_{T,1}^D - p_{T,1}^P\right)\sin\left(\frac{\Delta\phi_{12}}{2}\right)\right) \\ &\approx \sigma^2(p_T)\left\langle\sin^2\left(\frac{\Delta\phi_{1,2}}{2}\right)\right\rangle && (4.21)\\ \text{Var}\left(p_{T,2,\beta}^D - p_{T,2,\beta}^P\right) &= \text{Var}\left(\left(p_{T,2}^D - p_{T,2}^P\right)\sin\left(\frac{\Delta\phi_{12}}{2}\right)\right) \\ &\approx \sigma^2(p_T)\left\langle\sin^2\left(\frac{\Delta\phi_{1,2}}{2}\right)\right\rangle && (4.22)\\ \text{Var}\left(p_{T,1,\beta}^P - p_{T,2,\beta}^P\right) &= {\sigma_\beta^2}^P && (4.23) \end{aligned}$$

These terms can then be combined in order to get the variance of $p_{T,\beta}^D$;

$${\sigma_\beta^2}^D \approx 2\sigma^2(p_T)\left\langle\sin^2\left(\frac{\Delta\phi_{12}}{2}\right)\right\rangle + {\sigma_\beta^2}^P \tag{4.24}$$

The same calculation holds for ${\sigma_\alpha^2}^D$:

$${\sigma_\alpha^2}^D \approx 2\sigma^2(p_T)\left\langle\cos^2\left(\frac{\Delta\phi_{12}}{2}\right)\right\rangle + {\sigma_\alpha^2}^P \tag{4.25}$$

By subtracting equation 4.25 from equation 4.24 the detector component can be isolated using equation

4.18:

$$\sigma_\beta^{2D} - \sigma_\alpha^{2D} = 2\sigma^2(p_T)\left\langle \sin^2\left(\frac{\Delta\phi_{12}}{2}\right)\right\rangle - 2\sigma^2(p_T)\left\langle \cos^2\left(\frac{\Delta\phi_{12}}{2}\right)\right\rangle \tag{4.26}$$

$$= 2\sigma^2(p_T)\left\langle \cos^2\left(\Delta\phi_{12}\right)\right\rangle \tag{4.27}$$

$$\Leftrightarrow \sigma^2(p_T) = \frac{\left(\sigma_\beta^{2D} - \sigma_\alpha^{2D}\right)}{2\left\langle \cos^2\left(\Delta\phi_{12}\right)\right\rangle\}} \tag{4.28}$$

$$\Leftrightarrow \frac{\sigma(p_T)}{p_T} \approx \sqrt{\frac{\sigma_\beta^{2D} - \sigma_\alpha^{2D}}{2p_T^2\left\langle \|\cos(\Delta\phi_{1,2})\|\right\rangle}} \tag{4.29}$$

Therefore by measuring σ_α and σ_β at detector level the JER can be calculated.
In case both of the jets are in different $|\eta|$-regions eq.4.21 is not the same as eq.4.22. So the JER has to be calculated a bit differently:

$$\sigma_\beta^{2D} \approx \left(\sigma^2(p_T)_1 + \sigma^2(p_T)_2\right)\left\langle \sin^2\left(\frac{\Delta\phi_{12}}{2}\right)\right\rangle + \sigma_\beta^{2P} \tag{4.30}$$

$$\sigma_\alpha^{2D} \approx \left(\sigma^2(p_T)_1 + \sigma^2(p_T)_2\right)\left\langle \cos^2\left(\frac{\Delta\phi_{12}}{2}\right)\right\rangle + \sigma_\beta^{2P} \tag{4.31}$$

$$\Rightarrow \sigma_\beta^{2D} - \sigma_\alpha^{2D} = \left(\sigma^2(p_T)_1 + \sigma^2(p_T)_2\right)\left(\left\langle \sin^2\left(\frac{\Delta\phi_{12}}{2}\right)\right\rangle - \left\langle \cos^2\left(\frac{\Delta\phi_{12}}{2}\right)\right\rangle\right) \tag{4.32}$$

$$\Leftrightarrow \frac{\sigma(p_T)_1}{p_T} \approx \sqrt{\frac{\sigma_\beta^{2D} - \sigma_\alpha^{2D}}{p_T^2\left\langle \|\cos(\Delta\phi_{1,2})\|\right\rangle} - \frac{\sigma(p_T)_2^2}{p_T^2}} \tag{4.33}$$

4.3.3 Particle-level correction

As described in section 4.3.2 the bisector method is defined in order to separate the detector resolution from the imbalance created by ISR. Nevertheless as explained in section 4.3 there is another source of imbalance that affects the resolution. It is caused by errors that occur at the stage of the jet reconstruction. The main contribution to this is the so-called out-of-cone (OOC) effect produced by errors in the jet algorithm. For more details on this see section 4.1.

The JER should only describe the resolution originating in detector mismeasurements. So a particle level correction is applied. The name is chosen because it corrects the resolution to the effect seen at particle level. In order to achieve this the truth resolution is calculated and subtracted in quadrature from the JER calculated from reconstructed MC or data events. This strategy follows the simplified assumption that the OOC uncertainties and the detector uncertainties are independent from each other. Also the particle level uncertainties are assumed to be independent of the OOC uncertainties since otherwise the particle level corrections should be performed before the determination of the JER for each collection.

4.3.4 JER Parametrization

The JER is parametrized as a function of $p_{\mathbf{T}}$. It contains three terms:

1. Noise term: associated to the contribution from pile-up and electronic noise: $\sigma(p_T) \sim N$.

2. Statistical term: associated to the statistical uncertainty since the shower fluctuations can be described by a Poisson distribution: $\sigma(p_T) \sim S\ \sqrt{p_{\mathbf{T}}}$.

3. Constant term: the higher the $p_{\mathbf{T}}$ the higher the imbalance associated to e.g. passive material is: $\sigma(p_T) \sim C p_{\mathbf{T}}$.

So at the end the JER is modeled as follows:

$$\frac{\sigma(p_T)}{p_T} = \frac{N}{p_{\mathbf{T}}} \oplus \frac{S}{\sqrt{p_{\mathbf{T}}}} \oplus C \tag{4.34}$$

$$\frac{\sigma(p_T)}{p_T} = \sqrt{\left(\frac{N}{p_{\mathbf{T}}}\right)^2 + \left(\frac{S}{\sqrt{p_{\mathbf{T}}}}\right)^2 + C^2} \tag{4.35}$$

where the terms are quadratically added; $\oplus$ depicts the error summation without any impact from correlations.

Noise Term

In order to improve the parametrization of the JER the noise term can be measured separately. In general it has two contributions: one constant term that originates from electronic noise and threshold effects and one term originating in pile-up that grows with $\langle\mu\rangle$. The main method to determine it is the so-called random cone method. As the name suggests two cones (in the $\eta - \phi$ plane) with a given radius are randomly projected into a randomly chosen event, the so-called zero-bias sample. The imbalance between them is then used to determine the noise term. By restricting the cones to certain η-regions one can also derive the noise contribution for different η.

CHAPTER 5

Bisector Method Implementation

A general description of the bisector method has been given in the previous chapter (section 4.3.2). Here the details of the implementation are explained. In general ATLAS uses different software releases which imply a recalibration of the data and a complete new set of simulated events. In this thesis release 20.7 has been used.

5.1 Event selection

For determining the JER with the bisector method one first has to select a set of events in a way that the selection or combination of events does not bias the resolution in the end.

5.1.1 Data and MC samples

The analysis uses a subset of data that contains mostly dijet/multijet events, it is called JETM1 sample. More information on the used datasets and calibration can be found in appendix A.

Jx	truth jet pT low [GeV]	truth jet pT high [GeV]
JZ1	20	60
JZ2	60	160
JZ3	160	400
JZ4	400	800
JZ5	800	1300
JZ6	1300	1800
JZ7	1800	2500
JZ8	2500	3200
JZ9	3200	3900
JZ10	3900	4600
JZ11	4600	5300
JZ12	5300	infinity

Table 5.1: Used JZ slices and the p_{T}-ranges they represent.

Data

In this analysis 2016 data that passed single jet triggers are used. In order to account for problems with the detector and just using events that are recorded when everything is working the information about the status of the different detectors are stored in the good run list (GRL). The applied good run list and configuration files can be found in table A.2 in the appendix. In total it recorded an integrated luminosity of $\mathcal{L} = 32.88\,\mathrm{fb}^{-1}$.

MC

For Monte Carlo samples jet events produced by Pythia 8 are used. The used events are also required to pass single jet triggers, hence the sample still contains multijet events so cutting on them is still required, see 5.1.3. The samples are split into so called JZ slices based on the $p_{\mathbf{T}}$ of the truth leading jet, the higher the number the higher $p_T^{\text{leading jet}}$ is required to be. Table 5.1 shows the used JZ slices. For each sample approximatively the same number of events was produced. If one wants to combine them a weight factor (w_i) has to be applied to the different samples in order to correct for the different cross-sections, σ_i:

$$w_i = \frac{\sigma_i \cdot f_{\text{Eff}_i}}{n_{\text{events generated},i}} \tag{5.1}$$

The filter efficiency, f_{Eff}, for each JZ slice, i, accounts for the efficiency of the applied filter.

Additionally one wants to compare the number of events produced in the MC sample with the ones observed in data. So a normalization factor has to be applied. Therefore one multiplies the weight further with the recorded integrated luminosity. The numbers that are used to calculate the weights and the weights themselves can be found in appendix A. The samples have an attached W, this tells that weights are already included in the sample.

5.1.2 Trigger chain

The data recorded uses single jet triggers which require a single jet to pass a certain $p_{\mathbf{T}}$ threshold. There are different triggers based on the $p_{\mathbf{T}}$ they require and the η range they cover. Obviously a single event can be triggered by several triggers. Triggers and downscale factors were discussed in section 3.2.6. The task is now to combine the information of used triggers to apply the correct downscale factor for each event. In general there exist three strategies to calculate the downscale factors in the case of overlapping triggers.[39]

Division method

The most straightforward way to combine overlapping triggers is called the division method. Here the sample is divided into several not overlapping region based on kinematics. In each region events are required to pass one certain trigger that is fully efficient in that region. The applied downscale factor for all events in a region is the one associated to this trigger. The downside of this method is that a large fraction of events are discarded because a trigger fired that is not fully efficient and not the required trigger.

Exclusion method

The problem of firing a not fully efficient trigger is approached differently in the exclusion method. Instead of just using one trigger in a certain kinematic region a set of triggers is used. It is just required

that the combination of them is fully efficient. To determine the downscale factor the fired raw trigger that has the smallest downscale factor is used. This is done because the statistical uncertainty on the original number of events $\delta_{n,\text{original}}$ should be as small as possible and it depends on the event weights, w_j, in the sample:

$$\delta_{n,\text{original}} = \sqrt{\sum_{j \in events} w_j} \tag{5.2}$$

In order to not use a not efficient trigger in this region the event is also required to pass the associated actual trigger. If this one did not fire it is not used.

Inclusion method

Even better statistics gives the inclusion method. In this method actually no event is thrown away but the downscale factor on it is determined as a function of every raw trigger that fired. This is done of course as before in a set of triggers that are fully efficient in combination. The probability, P_{ij}, to accept an event, j, after the downscaling procedure for a certain trigger, j, can be calculated as:

$$P_{ij} = \frac{r_{ij}}{d_i} \tag{5.3}$$

where r_{ij} is equal to 1 if the raw trigger fired and 0 if it does not. For the probability that the event gets not or gets accepted after the downscaling the procedure by any trigger is given by the following formulae:

$$P_{j,\text{not accepted}} = \prod_{i=1}^{N_{\text{trigger}}} \left(1 - \frac{r_{ij}}{d_i}\right) \tag{5.4}$$

$$P_{j,\text{accepted}} = 1 - \prod_{i=1}^{N_{\text{trigger}}} \left(1 - \frac{r_{ij}}{d_i}\right) \tag{5.5}$$

Then the weight for the event is calculated as the reciprocal value of the probability:

$$w_j = \frac{1}{P_{j,\text{accepted}}} \tag{5.6}$$

Since this formula contains the decisions which trigger fired the formula has to be executed for every event.

Used trigger strategy

For single jet triggers there are two discriminants for the triggers: $p_{\mathbf{T}}$ and η of the leading jets. Each trigger requires a certain $p_T^{\text{leading jet}}$ and defines if it was measured in the central or forward region. While the ideal strategy in terms of statistics would be the usage of an inclusion method over all trigger combinations this would imply a lot of multiplications to be performed for every single event. Instead the analysis uses the division method in terms of $\overline{p_T}$ and for each kind of $p_{\mathbf{T}}$ triggers the inclusion method to combine central and forward triggers. The binning in $\overline{p_T}$ is motivated by the fact that the JER is determined in terms of $p_{\mathbf{T}}$ (see section 4.3.4) and it should be balanced for both jets. In the analysis the

same $\overline{p_T}$ binning is used as in the trigger. The weight are then calculated as

$$w_{\text{central}} = \frac{\mathcal{L}_{\text{total}}}{\mathcal{L}_{\text{trigger, central}}} \tag{5.7}$$

$$w_{\text{forward}} = \frac{\mathcal{L}_{\text{total}}}{\mathcal{L}_{\text{trigger, forward}}} \tag{5.8}$$

$$w_{\text{central+forward}} = \frac{\mathcal{L}_{\text{total}}}{\mathcal{L}_{\text{trigger, central}} + \mathcal{L}_{\text{trigger, forward}} - \frac{\mathcal{L}_{\text{trigger, central}}\mathcal{L}_{\text{trigger, forward}}}{\mathcal{L}_{\text{total}}}} \tag{5.9}$$

$$\tag{5.10}$$

where the luminosities associated to every trigger is calculated using the lumicalc tool[40] of ATLAS.

In table 5.2 the used triggers and the corresponding $p_{\mathbf{T}}$-ranges are shown. The $p_{\mathbf{T}}$ spectrum obtained after all corrections and applied downscale factors can be found in section 5.1.5.

$\overline{p_{T,\text{min}}}$	$\overline{p_{T,\text{max}}}$	Trigger
25	40	HLT_j15_OR_HLT_j15_320eta490
40	60	HLT_j25_OR_HLT_j25_320eta490
60	85	HLT_j35_OR_HLT_j35_320eta490
85	115	HLT_j60_OR_HLT_j60_320eta490
115	145	HLT_j60_OR_HLT_j60_320eta490
145	175	HLT_j110_OR_HLT_j110_320eta490
175	220	HLT_j110_OR_HLT_j110_320eta490
220	270	HLT_j175_OR_HLT_j175_320eta490
270	330	HLT_j175_OR_HLT_j175_320eta490
330	400	HLT_j260_OR_HLT_j260_320eta490
400	525	HLT_j360_OR_HLT_j360_320eta490
525	760	HLT_j360_OR_HLT_j360_320eta490
760	1200	HLT_j360_OR_HLT_j360_320eta490
1200	1500	HLT_j380_OR_HLT_j400_320eta490
1500	4000	HLT_j380_OR_HLT_j400_320eta490

Table 5.2: Used triggers and the $p_{\mathbf{T}}$-ranges they correspond to.

5.1.3 Dijet cuts

As described in section 5.1.1 the events in the samples still contain events with more than two jets. Also the single jet triggers just require at least one trigger passing the threshold, but they do not require a cut on the number of jets minimally or maximally contained in the event. Thus cuts have to be applied to make sure that a dijet-event is selected. The most obvious cut is that at least two jets should be contained in the event. Additionally, a matching to the primary vertex had been done in the processing of the event. At least two tracks should originate there. On the other hand instead of two jets that are balanced w.r.t. to each other the event could also contain a lot of jets that are just balanced in the sum. Having a hard cut on the maximum number of jets is also not that sensible since especially at high $p_{\mathbf{T}}$ events the jet algorithm could have failed to associate all of the energy that belongs to a jet to that jet but created two jets a high $p_{\mathbf{T}}$ one and a soft jet. Another possibility is that the underlying event or the pile-up created additional jets or that the in the hard scattering two hard jets and some additional soft jets had been produced. Since

our method only requires balanced jets, instead a cut on the angle between the leading (jet_1) and the subleading (jet_2) is required:

$$\Delta\phi_{12} \geq 2.5 \tag{5.11}$$

Additionally the other jets should not have a too high $p_{\mathbf{T}}$ compared to the dijet system. Because of this a cut on the jet with the third highest $p_{\mathbf{T}}$ is applied:

$$p_{T,3} \leq 0.4\overline{p_T} \tag{5.12}$$

5.1.4 Additional cuts

There are some additional cuts that get applied because of different reasons. For example $p_T^{\text{leading jet}}$ should be at least 15 GeV since the JER up to now is just measured at higher $p_{\mathbf{T}}$ (for details see section 4.3). Also a JVT cut (see section 4.2.1 is applied:

- **PFlow:** JVT > 0.2
- **EMTopo and LCTopo:** JVT > 0.59

In order to cut away wrongly calculated Monte Carlo events with a leading jet that deviates a lot from $\overline{p_T}$ a cut on the truth $p_T^{\text{leading jet}}$ is applied:

$$1.4p_{T,\text{truth leading jet}} \leq \overline{p_T} \tag{5.13}$$

5.1.5 Control plots

In figure 5.1[1] one can see the final $p_{\mathbf{T}}$ distributions for Monte Carlo and data. As one can see they are smooth in the logarithmic plane. Also ϕ of the leading jets is smooth for both (figure 5.2). Additional plots of the distributions including data-MC comparisons can be found in appendix B.

5.2 Calculating the JER

This chapter will follow the procedure explained in section 4.3.2 in determining the jet energy resolution with the bisector method. All steps are carried out for subsets of the data in order to obtain the jet energy resolution as a function of $p_{\mathbf{T}}$ and η. The subsets are defined in terms of $\overline{p_T}$ as well as $|\eta|$ of the leading and the subleading jets. In table 5.3 one can see the borders of this binning. They have been chosen based on features of the detector depending on η and based on the used triggers in terms of $\overline{p_T}$ (see section 5.1.2). Also they were chosen in a way that they are consistent with the direct balance method. The total number of $p_{\mathbf{T}}$-η bins per jet collection can be calculated with the number of η-bins, n_η, and the number of $\overline{p_T}$-bins, $n_{\overline{p_T}}$:

$$n_{\text{bins}} = n_{\overline{p_T}} \cdot n_\eta^2 = 15 \cdot 8^2 = 960 \tag{5.14}$$

[1] In the main part of the thesis mostly plots obtained from the PFlow jet collection are shown. Plots for other jet collections can be found in the appendices B, C and D.

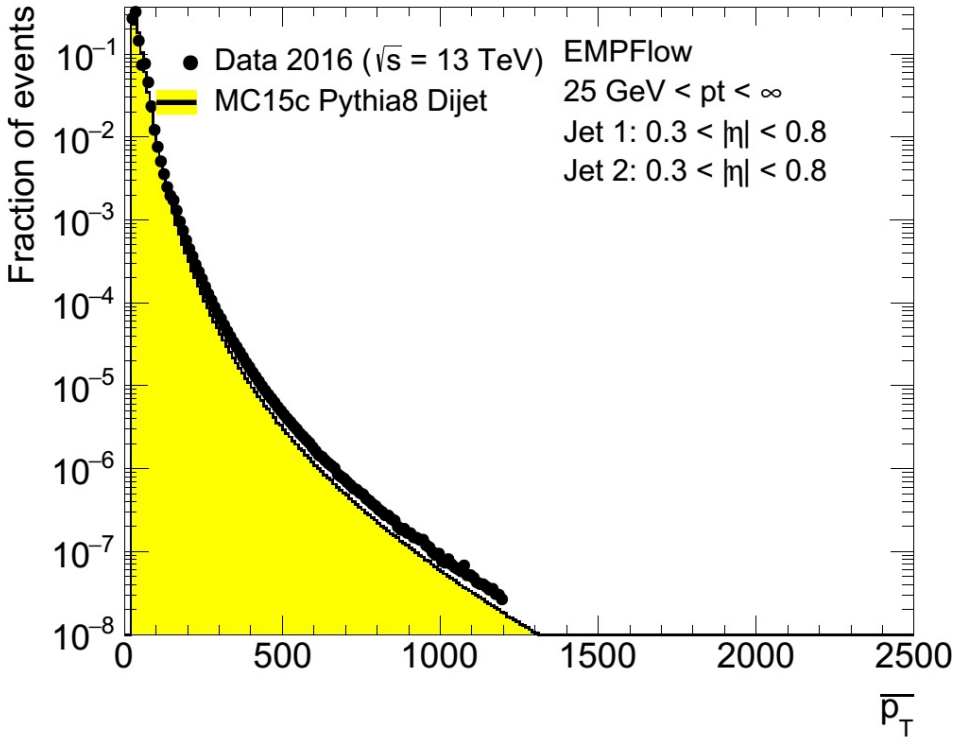

Figure 5.1: Plot of $\overline{p_T}$ in a comparison between MC and data.

$\overline{p_T}$ (GeV)	25	40	60	85	115	145	175	220	270	330	400	525	760	1200	1500
$\lvert\eta\rvert$	0	0.3	0.8	1.2	1.7	2.5	3.2	4.5							

Table 5.3: Used $\overline{p_T}$ and $|\eta|$ binning.

5.2.1 Bisector distributions

As described in equation 4.29 the JER extracted with the bisector method depends on the variance of p_T^α and p_T^β and the mean of $\cos(|\Delta\phi_{i,j}|)$. Examples of the cosine distributions can be seen in figure 5.3. As expected they peak at π and there is a cut applied at $|\cos(2.5)| \approx 0.8$ which corresponds to the dijet cut specified in section 5.1.4. Some of the distributions can be seen here, more can be found in appendix B.

p_T^α

The α-axis is defined as the bisector. Since the imbalance vector $p_{T,\text{add}}$ by construction is in the same half plane as the bisector p_T^α by definition can only be positive. Figure 5.4 shows typical distributions for p_T^α. The distributions have an exponential shape which is expected since they should mostly consist of ISR (see section 2.2.1). The distribution in total gets broader for higher $p_\mathbf{T}$. As MC models data pretty well.

p_T^β

Some typical distributions of p_T^β can be found in figure 5.5. The β-axis is calculated as $\alpha + \frac{\pi}{2}$. Since the β-axis will randomly go into the direction of the imbalance vector $p_{T,\text{add}}$ or opposite to it the distribution

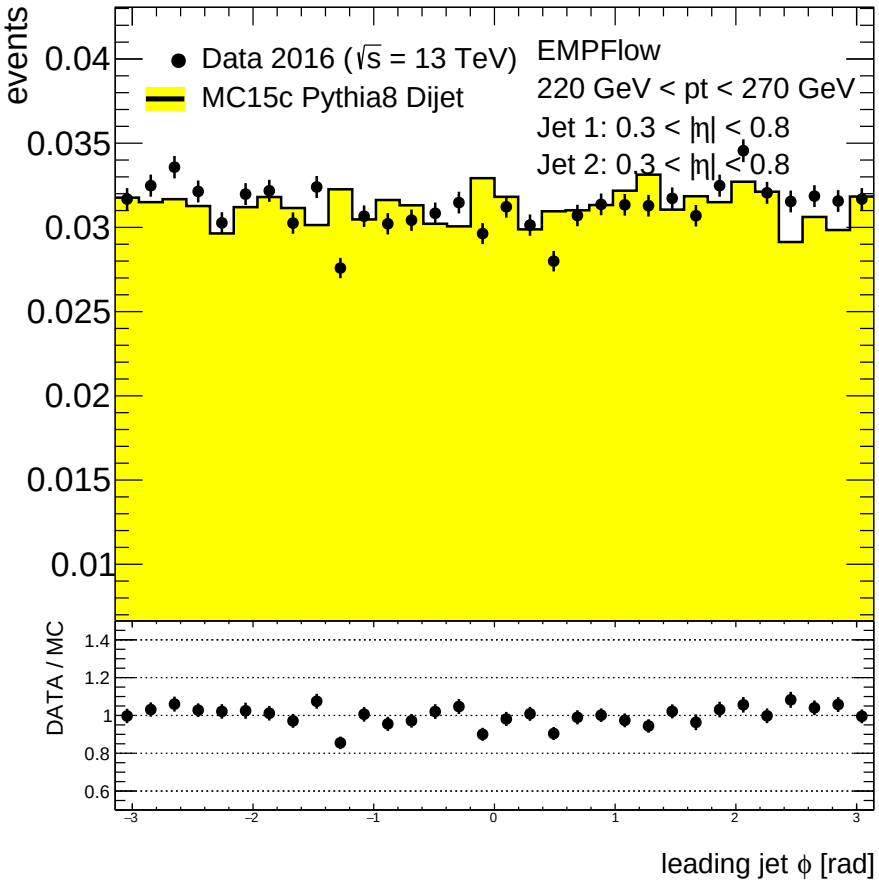

Figure 5.2: Plot of ϕ of the leading jet in a comparison between MC and data.

is symmetric around 0. In general the distributions get broader and have more prominent tails for higher $p_{\mathbf{T}}$.

5.2.2 Determining the variance: fitting procedure

For obtaining the variance of p_T^α and p_T^β the distributions are fitted and the variance of the fitted distributions is used in order to account for fluctuations and binning effects. Different approaches for this step of the procedure have been tested and are explained in the following.

Gaussian

The standard approach for resolution studies is to use a Gauss-function to fit the distribution.

$$\mathrm{Gaus}_{p_0,\mu,\sigma}(x) = \frac{p_0}{\sqrt{2\pi\sigma^2}} e^{-\frac{(x-\mu)^2}{2\sigma^2}} \tag{5.15}$$

In the past it has also been used for the bisector method [1]. In figure 5.6 the fits of a Gaussian to p_T^α and p_T^β can be seen. A fixed binning for all histograms is used, a possible improvement could be using a

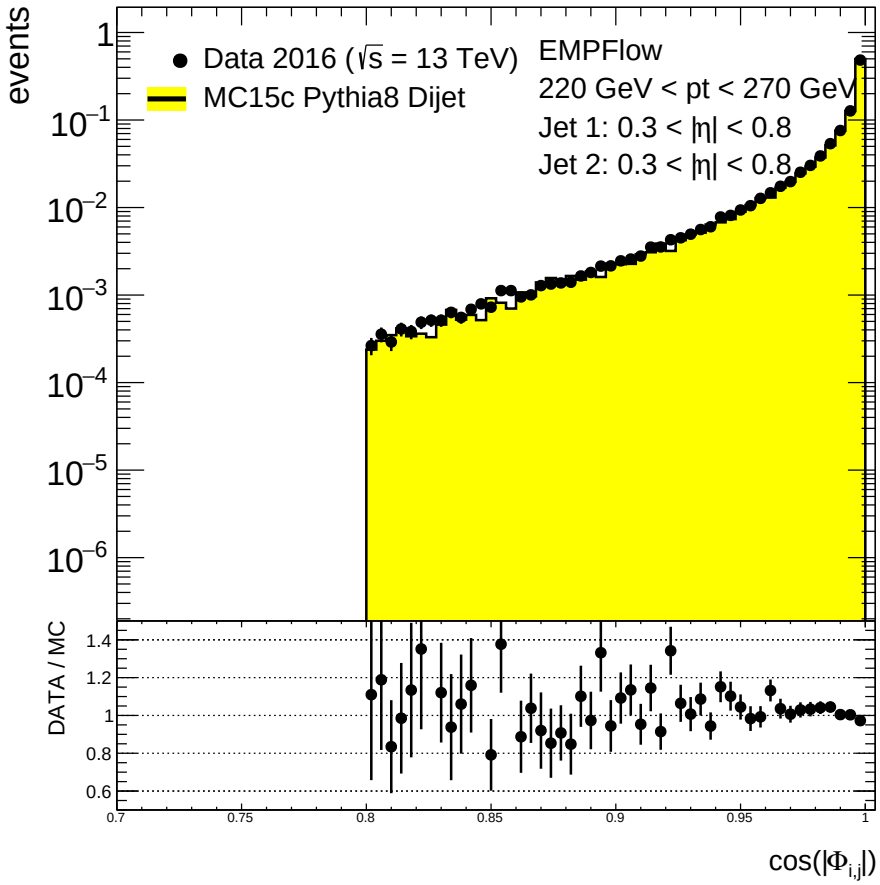

Figure 5.3: Plot of $\cos(|\Delta\phi_{i,j}|)$ in a comparison between MC and data.

variable binning. p_T^α has been fitted with half a Gaussian and fixed $\mu = 0$. The distributions justify these choices. On the other hand the choice of a Gaussian as an underlying function does not seem to resemble the distributions, especially at higher $p_\mathbf{T}$. It is arguable that p_T^β could be resembled by a Gaussian with additional non-Gaussian tails, but p_T^α is basically just described by this tail.[2]

For each fit different ranges where the fit is performed have been tried. This is well established instrument to not be affected by the non-Gaussian tails. But the Gaussian component for some p_T^α distributions are so small that the fit would have to be performed just over a few bins when the distribution itself is about a hundred times broader. It is obvious that such a fit does not resemble the true width of such a distribution. So the fit of a Gaussian is discarded. Nevertheless narrowing the fit range in order to focus on the core of the distribution instead of the tails has been proven to be a valuable tool. Thus it is used in all strategies that are presented here.

Gaussian and Exponential

Since it seems to be possible to fit the core of p_T^β with a Gaussian the first approach was to just change the fitted function that is used for p_T^α. An exponential was the obvious choice. In figure 5.7 the associated

[2] In previous analysis the same behaviour occured.[1] The reason for not changing the fit function is probably that the JER has just been calculated for lower $p_\mathbf{T}$ where using a Gaussian is still somewhat arguable.

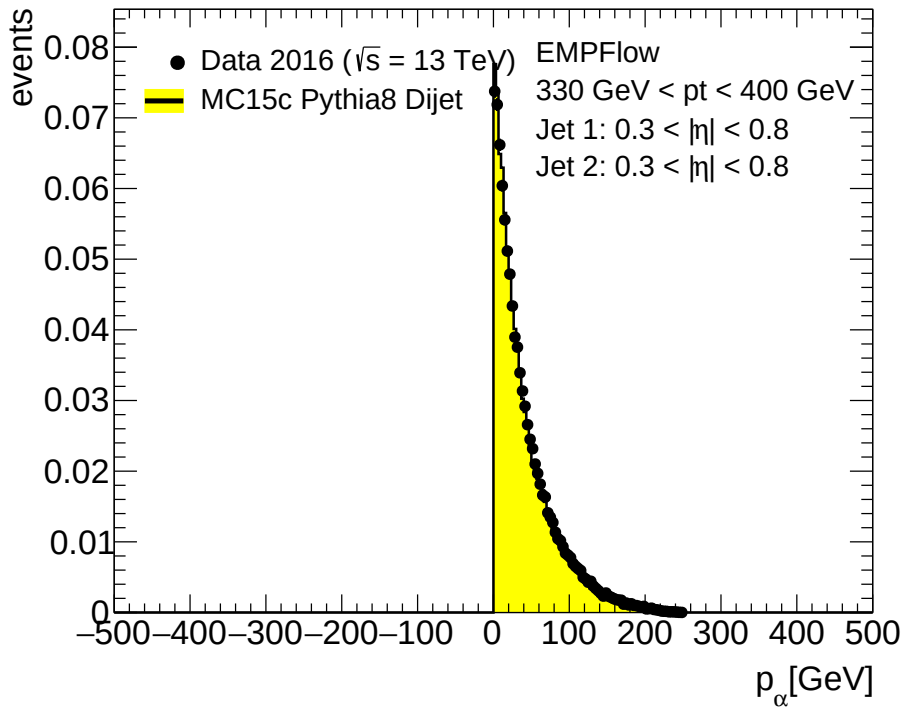

Figure 5.4: Plot of p_T^α in a comparison between MC and data. It can only be positive.

fits can be seen. The fit is definitely better than a Gaussian but still not ideal. An additional problem is the definition of the variance for an exponential function. The first approach was to use the definition of the variance as follows:

$$\mathrm{Var}(f(X)) = \int_{-\inf}^{\inf} f(X)(X-\mu)^2 dX \tag{5.16}$$

Here μ denotes the mean of the distribution and X the distribution. As the lower boarder is 0 used for p_T^α. For an exponential density function these equations hold:

$$\exp(x) = \tau e^{-\tau x} \tag{5.17}$$

$$\mathrm{Var}_{\exp}(X) = \frac{1}{\tau^2} \tag{5.18}$$

Unfortunately the variance of an exponential tends to be higher than the one of a Gaussian (σ^2) due to the fact that Gaussian tails fall quadratically. So subtracting them quadratically tends to give a negative number which makes the determination of the JER impossible.

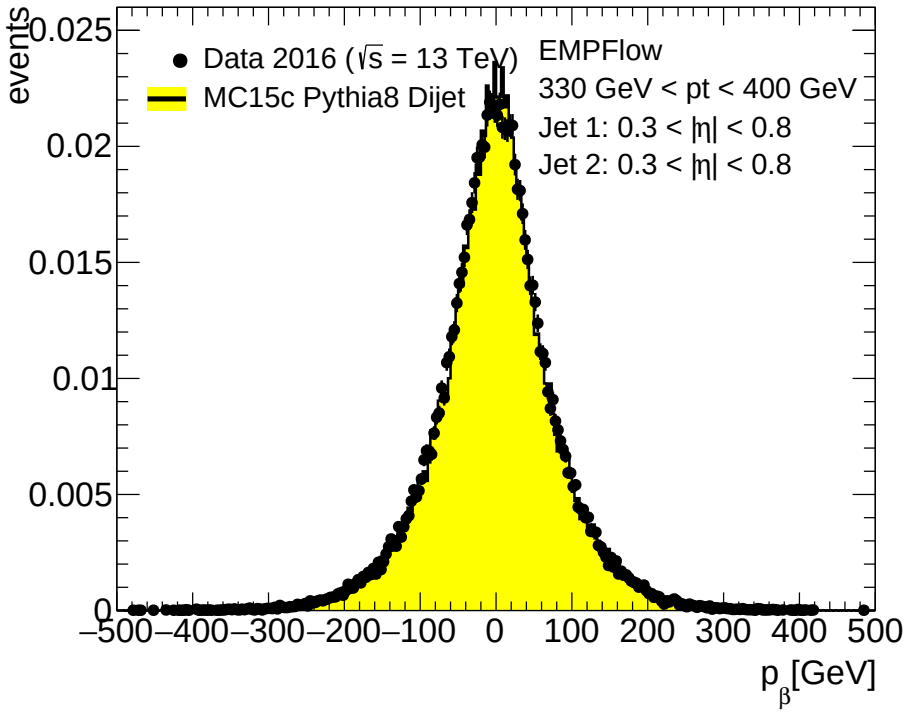

Figure 5.5: Plot of p_T^β in a comparison between MC and data.

Convolution I

In order to have a consistent definition for the variances of p_T^α and p_T^β this ansatz uses the same function to fit both distributions. Since the distributions seem to have contributions from an exponential and a Gaussian a convolution is built as:

$$(\exp(x) \circledast \text{gaus}(x))(y) = \int \exp(x) \cdot \text{gaus}(y - x)dx \tag{5.19}$$

Figure 5.8 shows the fitted distributions for p_T^α and p_T^β. The function describes the distributions very well. But in order to define the variance some additional gymnastics are required. The variance as defined in equation 5.16 is unfortunately not defined. To obtain a defined value the integration borders are set to $[-500, 500]$. As one can see in the previous plots most distributions vanish at this point. With theses definitions determining the JER works. On the other hand the values obtained for the JER are approximatively twice as high as expected, also compared to the ones obtained with the Gaussian approach. The reason for this lies close to the problem of the previous fitting strategy: by including the variance of an exponential the obtained result is no longer comparable to the previous calculations of the JER which use the variance of a Gaussian. For the calculation of the variance and its uncertainties with this approach Mathematica[41] was used.

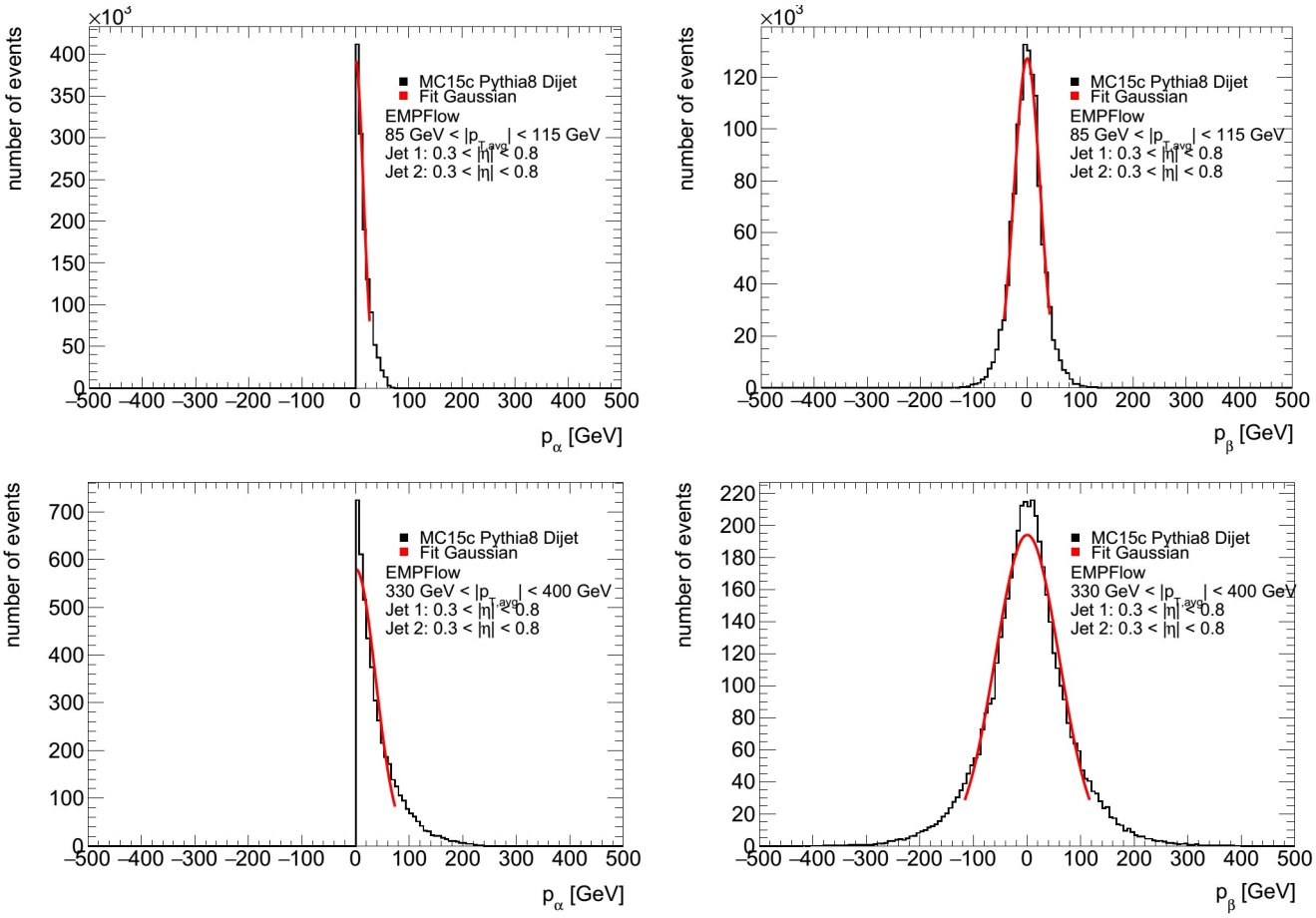

Figure 5.6: p_T^α and p_T^β fitted with a Gaussian.

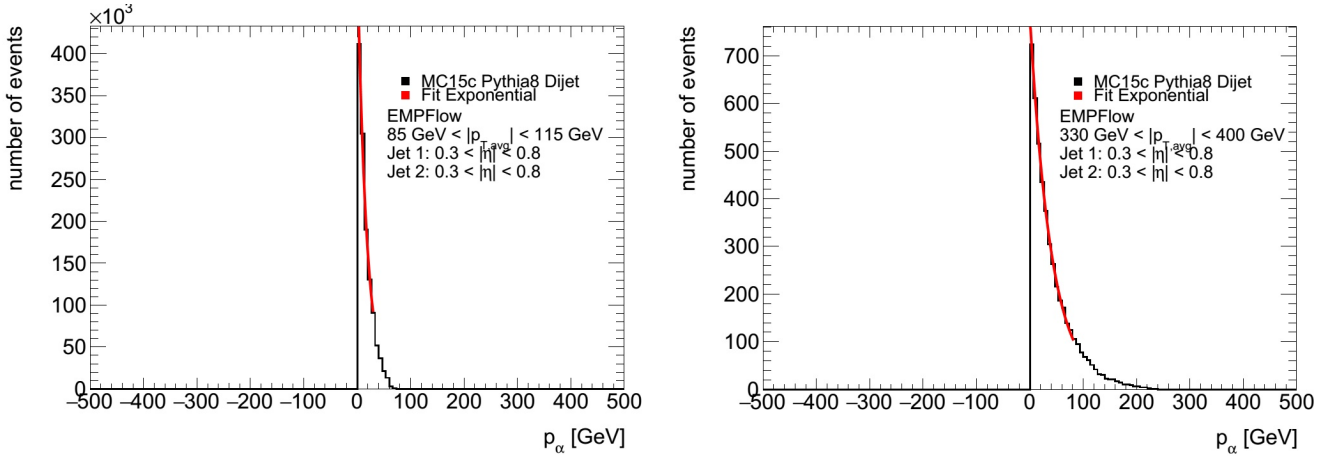

Figure 5.7: p_T^α fitted with an exponential.

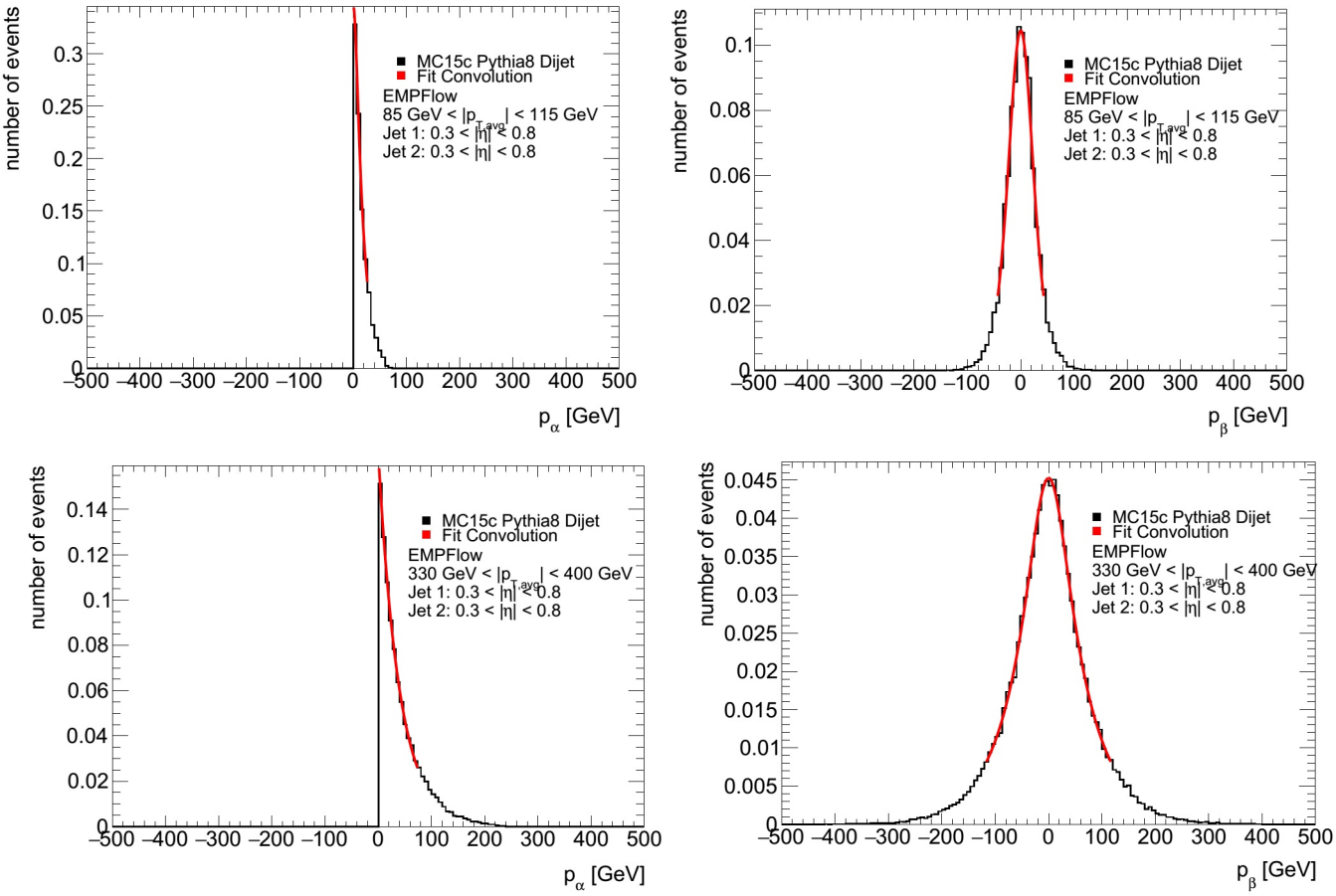

Figure 5.8: p_T^α and p_T^β fitted with a convolution of a Gaussian and an exponential.

Convolution II: Same decay parameter

In order to have a definition of the variance comparable with the one from a Gaussian fit a new strategy is used. The basis of the JER formula 4.29 is the variance of p_T^β without the variance of p_T^α. In the previous strategies this is obtained by a subtraction of both. The new idea is now to describe p_T^β as a distribution which contains both contributions, the variance of p_T^α and the variance that gives the JER. This is the applied strategy:

1. fit an exponential to the distribution of p_T^α and extract the decay parameter, τ.
2. fix the obtained decay parameter, τ.
3. convolute the fitted exponential (with fixed τ) with a Gaussian.
4. fit the distribution of p_T^β with the obtained function.
   - τ remains fixed.
   - σ is the only free parameter that is associated with the width of p_T^β.

$\Rightarrow$ σ^2 can be used as the variance.

With this strategy σ resembles the variance of p_T^β without the variance of p_T^α. Some distributions fitted with this strategy can be seen in figure 5.9. Unfortunately p_T^α has also some Gaussian component at high $p_\mathbf{T}$ and also the modelling of p_T^β with the decay parameter of p_T^α fails sometimes. This brings us to the next approach

Convolution III: "advanced convolution"

In order to combine the well defined variance with good modelling the previous method is adapted. Instead of just fitting an exponential to p_T^α a convolution of an exponential with a Gaussian is used. As a consequence p_T^β has to be fitted with the convolution of two Gaussians and an exponential, where the parameters of the exponential and one Gaussian are fixed. The free σ is then used to define the variance. In total the procedure looks like this:

1. fit p_T^α with a convolution of an exponential and a Gaussian.
2. fix the obtained decay parameter τ and standard deviation σ_α.
3. convolute the function that has been fitted previously (with fixed τ and σ_α) with a Gaussian.
4. fit p_T^β with the obtained function.
   - τ and σ_α remain fixed.
   - σ_β of the second Gaussian is the only free parameter associated to the width of. p_T^β

$\Rightarrow$ σ_β^2 can be used as the variance.

In figure 5.11 the fits to some distributions can be seen. In order to check the quality of the fits the χ^2 has been calculated. In figure 5.10 $\frac{\chi^2}{\text{degrees of freedom}}$ of some fits can be seen. The fits model the distributions well in general. Because of the high numbers of fits that are performed some tend to fail. In principle slight tuning of initialization values of the fit parameters and the fit range can make each fit perform. The challenge is to tune the parameters in a way that all fits perform.[3] In the appendix a table with the used fit parameters can be found.

5.2.3 JER

To calculate the jet energy resolution (equations 4.29) four inputs are needed. How $\sigma_\beta^2 - \sigma_\alpha^2$ is obtained has been explained in detail in section 5.2.2. The cosine part is obtained as the mean of the distribution shown in section 5.2.1. For $p_\mathbf{T}$ the lower border of the used $\overline{p_T}$ bin is used. Since the JER distribution is expected to be falling this may assign a higher JER for most of the spectrum. On the other hand this is the most conservative choice. For reasons of visibility the points are still drawn in the middle though. A possible alternative could be drawing and calculating the JER w.r.t. the mean of each bin.

Calculate the JER for all $|\eta|$-regions

The jet energy resolution is calculated for different $|\eta|$-bins. But as depicted in section 4.3.2 the strategy needed to obtain a JER from a set of events where both jets had been in different $|\eta|$- regions is a bit more complicated. In order to obtain the JER for a single $|\eta|$-region it is needed to subtract the contribution of the other $|\eta|$-region. So we are left with two different approaches:

[3] the number of fits per jet-collection is $n_{\text{bins}} \cdot 2 = 1920$

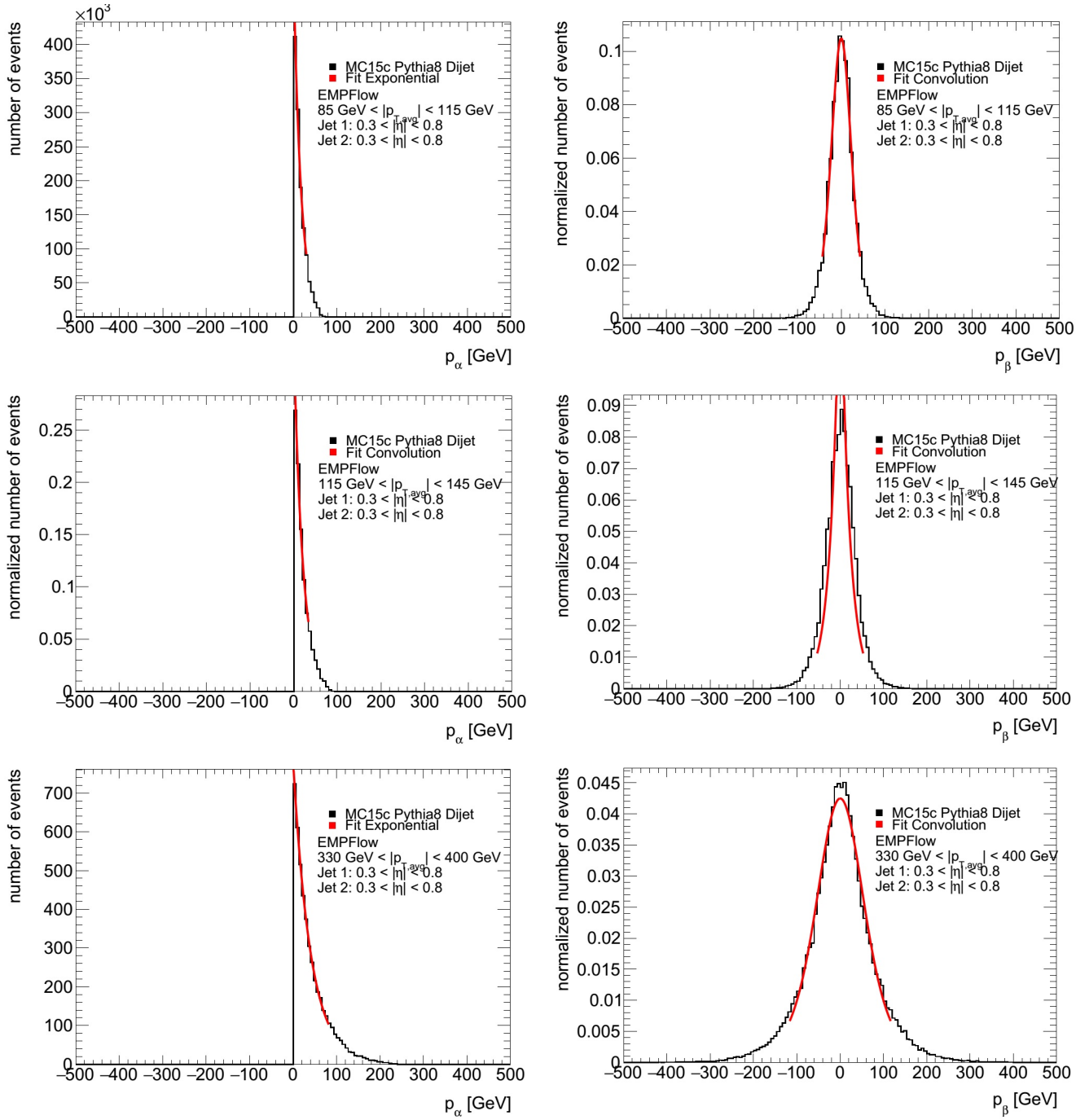

Figure 5.9: p_T^α fitted with an exponential and p_T^β fitted with a convolution of a Gaussian and an exponential with the same decay parameter as used in p_T^α. The middle plot is a typical example for a failing fit with this method.

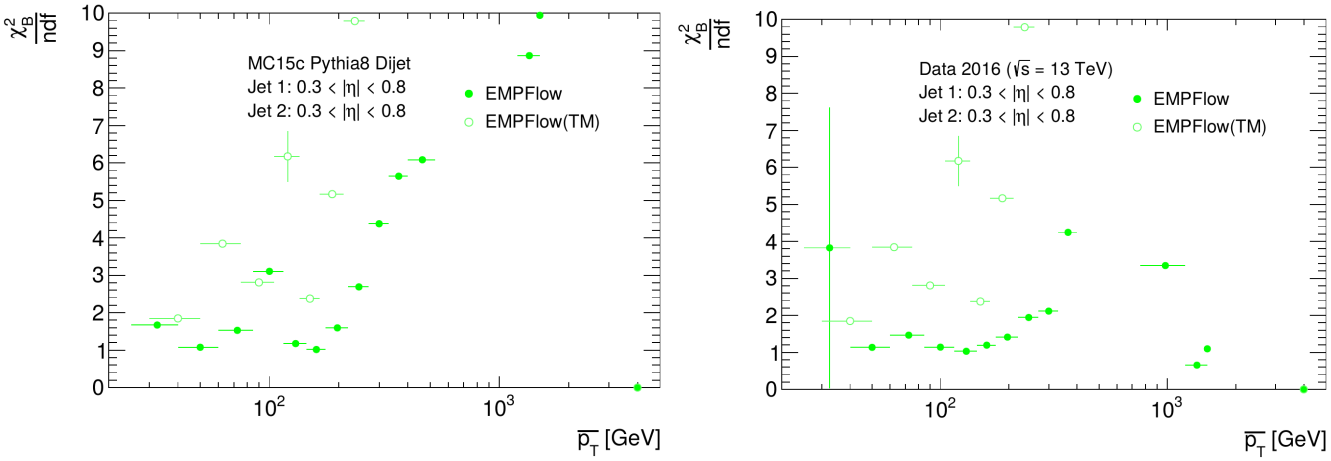

Figure 5.10: χ^2 as a function of $p_{\mathbf{T}}$ for data and MC.

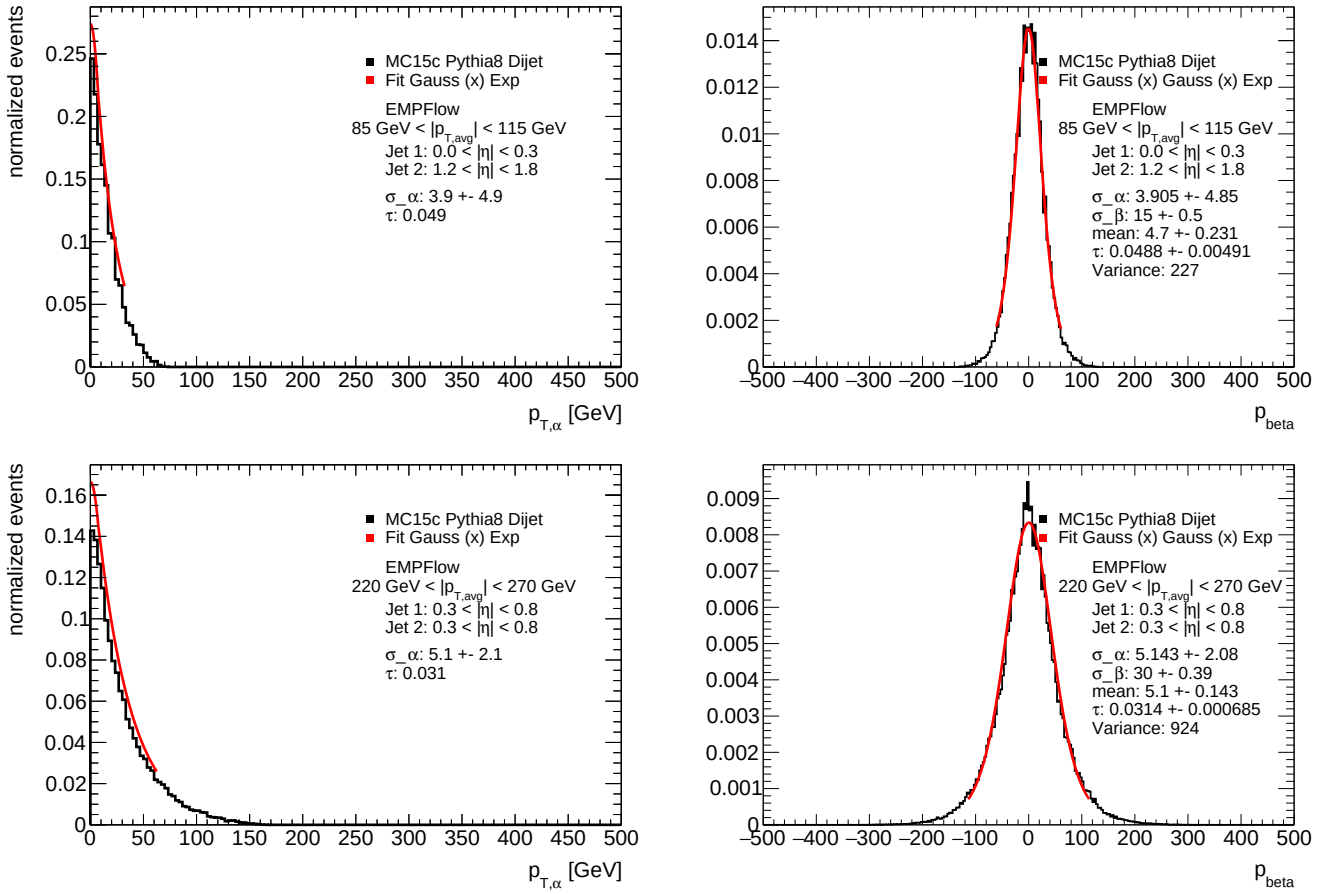

Figure 5.11: p_T^{α} and p_T^{β} fitted with the advanced convolution method.

- use only events where both jets are measured in the same $|\eta|$-region
- use events where one jet is in the region being probed and the other one is in a reference region that had been measured previously by the other method

In order to decide which strategy to take and in case of the second strategy to decide which region is the reference region a statistics plot has been produced. A good result requires histograms with good statistics so a sensible fit can be performed. So the strategy with most statistics should be chosen. In figure 5.12 the statistics for each bin in some $\overline{p_T}$-regions can be seen. The diagonal contains the bins that would be fitted with the first strategy. The statistics in these bins are high but not as high as in the bins containing a jet in $0.3 \leq |\eta| \leq 0.8$. These bins have the highest statistics for each $\overline{p_T}$ and $|\eta|$ of the other jet. So the second region with $0.3 \leq |\eta| \leq 0.8$ as the reference region is the obvious choice for obtaining the highest statistics possible. There are other requirements a reference region should fulfil. On the one hand the JER in this region should be well measured which is possible since the bin with both jets in this region has actually the best statistics. On the other hand the resolution in this region should be good in order to have as least bias as possible in the sample. Fortunately this region lies also in the region of the tracker so it is one of the best understood regions with the best resolutions. This choice is also consistent with reference regions picked by other JER-strategies as the direct balance method.

5.2.4 Particle-level correction

As described in section 4.3.3 the JER has to be corrected to particle-level. This particle-level correction is performed by determining the JER for a truth collection with the same strategy as for reconstructed events. The truth events are chosen by applying the event selection to reconstructed events and then matching the leading and subleading jet in the truth jet collection with the jets from the reconstructed events. The geometrical matching requirement is $\Delta R \leq 0.3$.

If there are no jets that fulfil this requirement the event is discarded. Since there are no truth jets for data the truth JER for MC is used to perform the particle level subtraction. In figure 5.13 some fits for the truth-matched collections can be seen. As expected the distributions are narrower since they contain fewer sources for mismeasurements and thus also the obtained variance is smaller than for the distributions based on reconstructed events.

5.2.5 JER with particle-level correction

In figure 5.14 the JER for reconstructed events and truth-matched events as well as the quadratically subtracted value can be seen. In general the JER for the truth-matched distributions are a bit smaller than the ones obtained from reconstructed events. If this is not the case the fits for either of them failed. Then determining the JER fails. The drawn errors are obtained from fitting or error propagation respectively. It can be seen that the errors obtained from the fits in the first place are reasonable, but the errors on the quadratic difference are high. This accounts for the small difference between both, corresponding to the Gaussian error propagation term of a quadratic difference:

$$z = \sqrt{x^2 - y^2} \tag{5.20}$$

$$\Delta z = \frac{2\sqrt{(\Delta x \cdot x)^2 + (\Delta y \cdot y)^2}}{z} \tag{5.21}$$

By dividing a number of the order of 0.1 the error is scaled up. If the second strategy for different η-regions (see section 5.2.3) is used the error is enlarged by this effect twice. Nevertheless it is possible

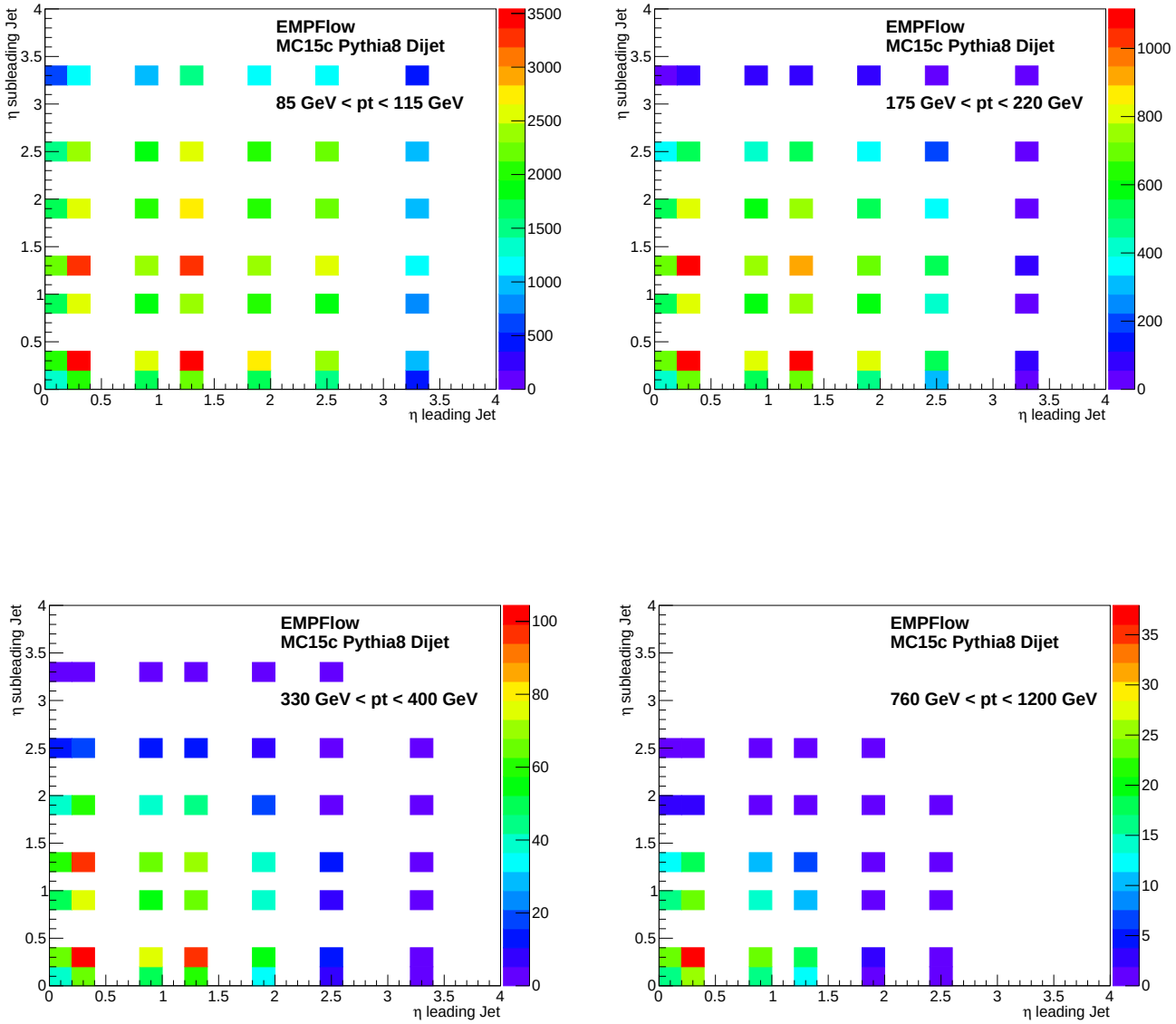

Figure 5.12: Statistics in different η-regions for different p_{T}-regions.

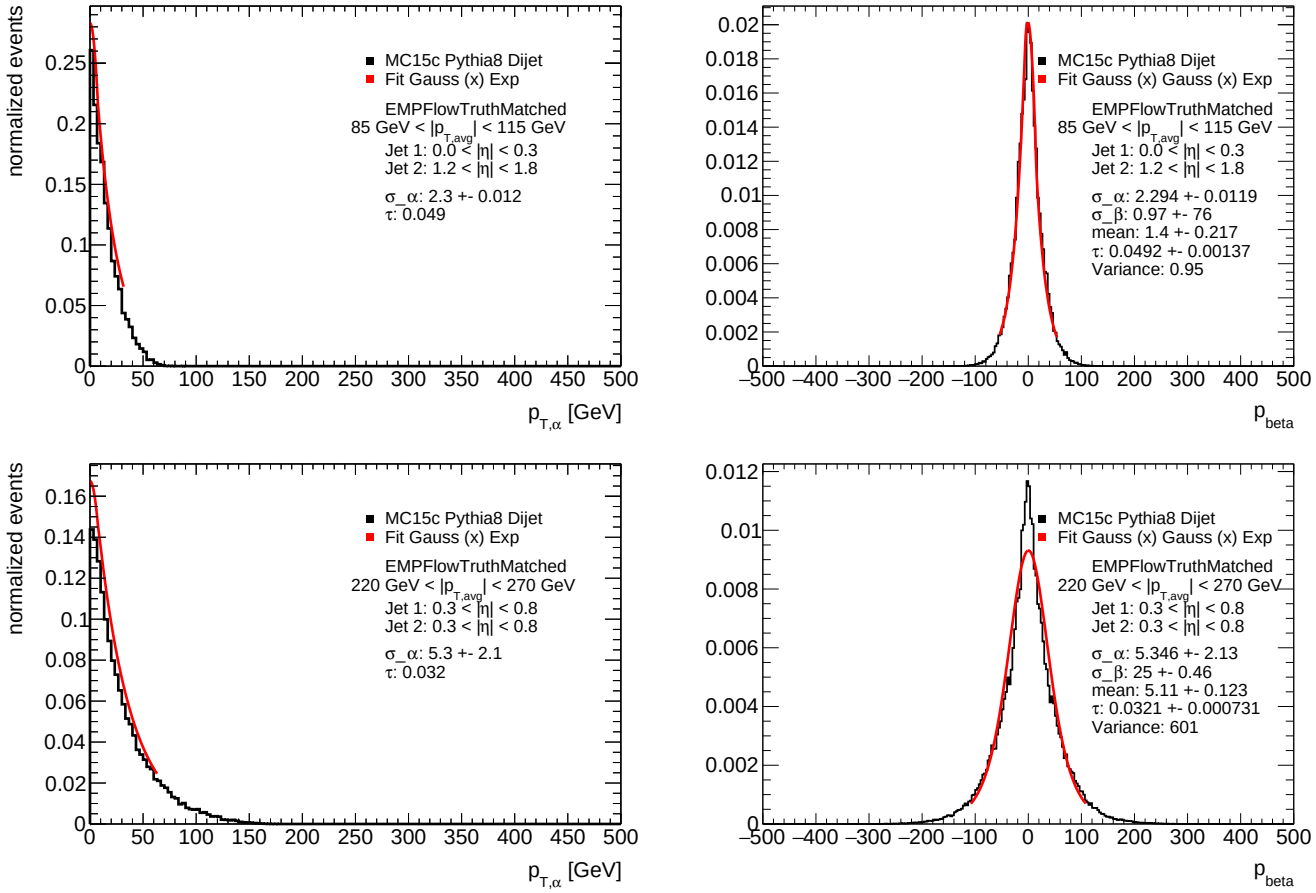

Figure 5.13: p_T^α and p_T^β from truth events fitted with the advanced convolution method.

that the errors obtained from the fitting are in fact not correct, but some statistical effect as the weighted dataset has not been taken into account correctly. More studies will go into cross-checking this.

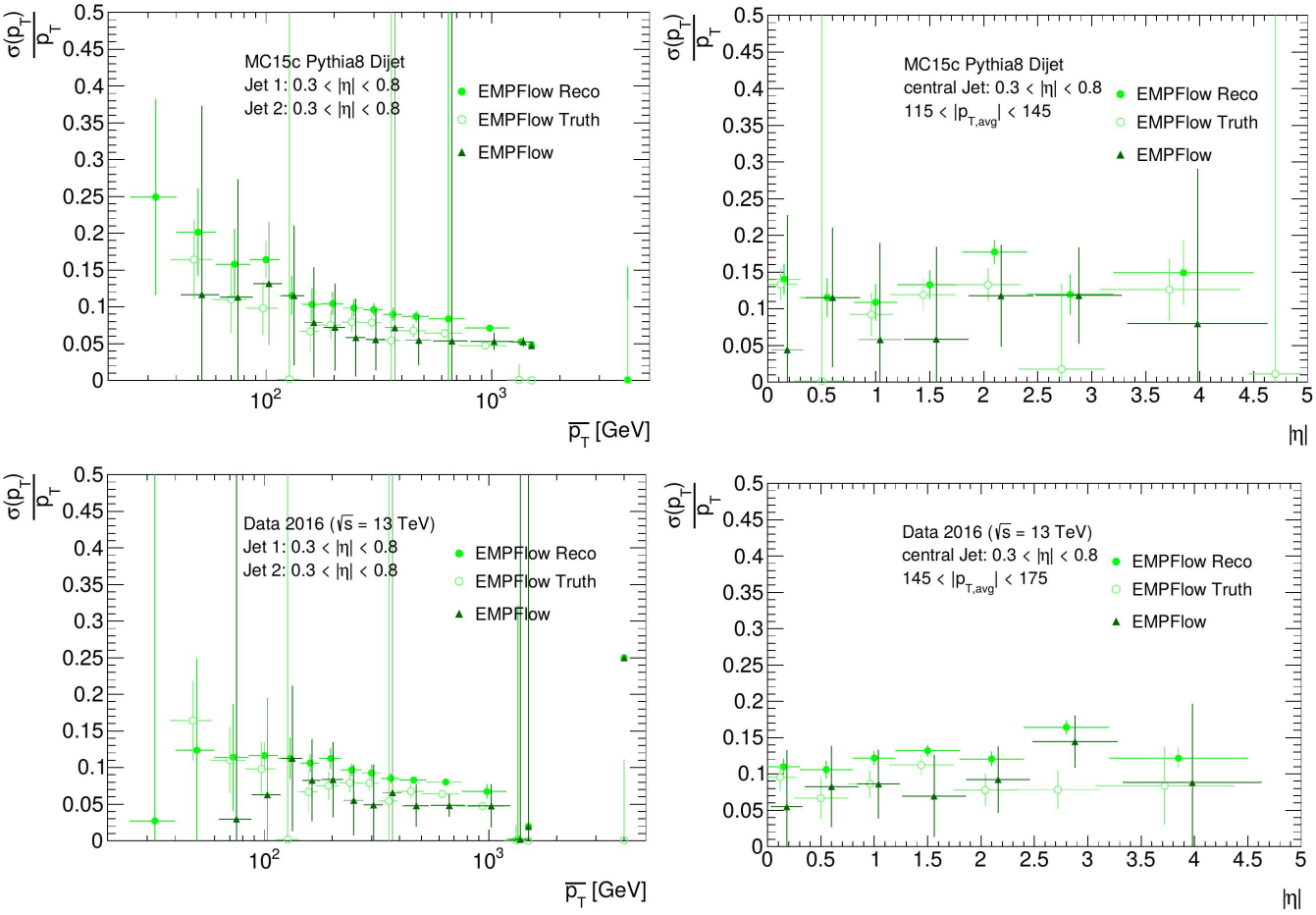

Figure 5.14: The JER obtained from reconstructed jets as well as truth jets is shown. By subtracting these the final JER (dark green triangles) is obtained. This is shown for both MC and data as well as in dependence of $p_{\mathbf{T}}$ and $|\eta|$. The two big uncertainties originate in an error obtaining the uncertainties.

CHAPTER 6

Results

6.1 JER determined with the bisector method

In this chapter the jet energy resolution obtained with the bisector method will be presented and compared to the 8 TeV results.

6.1.1 p_{T} dependence

The JER is expected to fall as a function of p_{T} as described in section 4.3.4. In figure 6.1 the JER dependence of p_{T} can be seen for different $|\eta|$-regions with the fitted function. The noise component has been fixed in the region where the random cone method has measured it for the EM-scale: 1.5 to 1.6[28]. In general the distribution follows the expectation, but not all fits are optimized yet. For some points p_T^{α} and p_T^{β} are not fitted well and thus the points do not appear in the plots. Especially the fits at lower p_{T} tend to be unstable. In unstable cases also the errors are higher then expected.

6.1.2 Different jet collections

In the previous plots just the PFlow results have been shown. But the same procedure has been applied to the other jet collections. In figure 6.1 the overlaid JER for all three jet collections is shown. In general it can be seen that all jet collections agree well inside the uncertainties. It is expected that for $|\eta| \geq 2.1$ the behaviour of PFlow is similar to the EMTopo collection, also this is in agreement inside the given uncertainties. The fact that some fits fail for some jet collections while they are stable for others in the same kinematic region is not believed to originate from an underlying difference of the jet collections, but rather from the fitting or statistical fluctuations.

6.1.3 $|\eta|$ dependence

As described earlier the JER changes with $|\eta|$ since the detector changes. The plots as a function of η can be seen in figure 6.2. In general the JER as a function of $|\eta|$ is pretty stable which is a nice feature of the ATLAS detector and a cross-check for the performance of the bisector method. But there are some small dependencies. The lowest JER is obtained in the most central part of the detector. This is expected since the detector is best in this region. For higher $|\eta|$ the obtained JER gets higher and is especially high at $1.2 \leq |\eta| \leq 2.1$ where the transition between central and forward detectors take place.

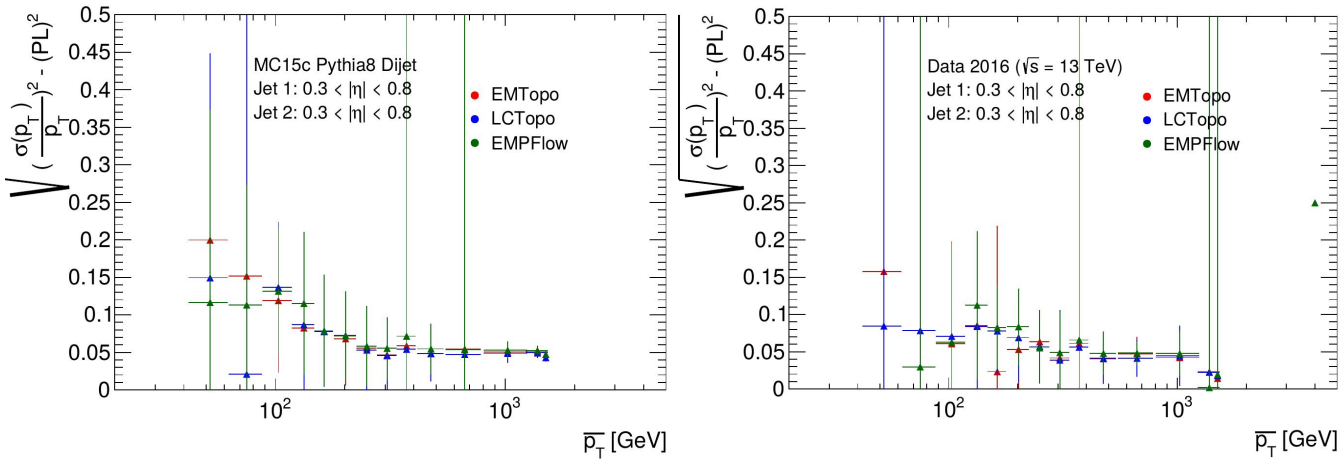

Figure 6.1: The JER in dependence of p_{T} for all three jet collections. It is shown for both MC and data.

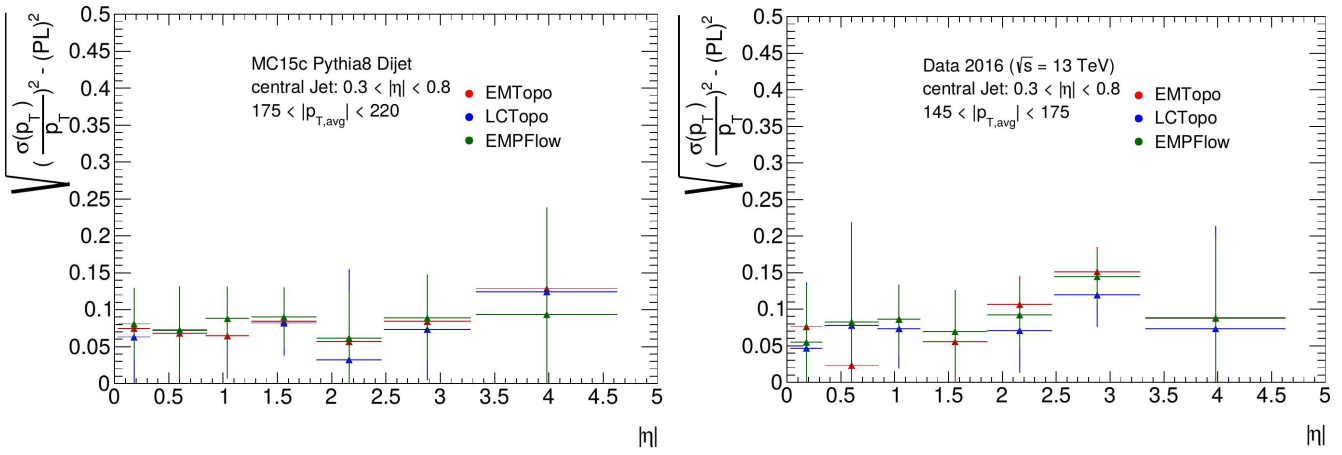

Figure 6.2: The JER in dependence of $|\eta|$ for all three jet collections. It is shown for both MC and data.

6.2 Comparison with 8 TeV results

In order to compare the performance of the bisector method method with the expectations it is compared with the previously performed direct balance and bisector method results. In figure 6.3 the results from 8 TeV can be seen. In general the results are comparable although the errors are larger. Additionally this time the JER is calculated over a broader kinematic range.

6.3 Outlook

The JER has been derived with the bisector method, but there are some things that still need to be done before the JER obtained by the bisector method can be used in a physics analysis:

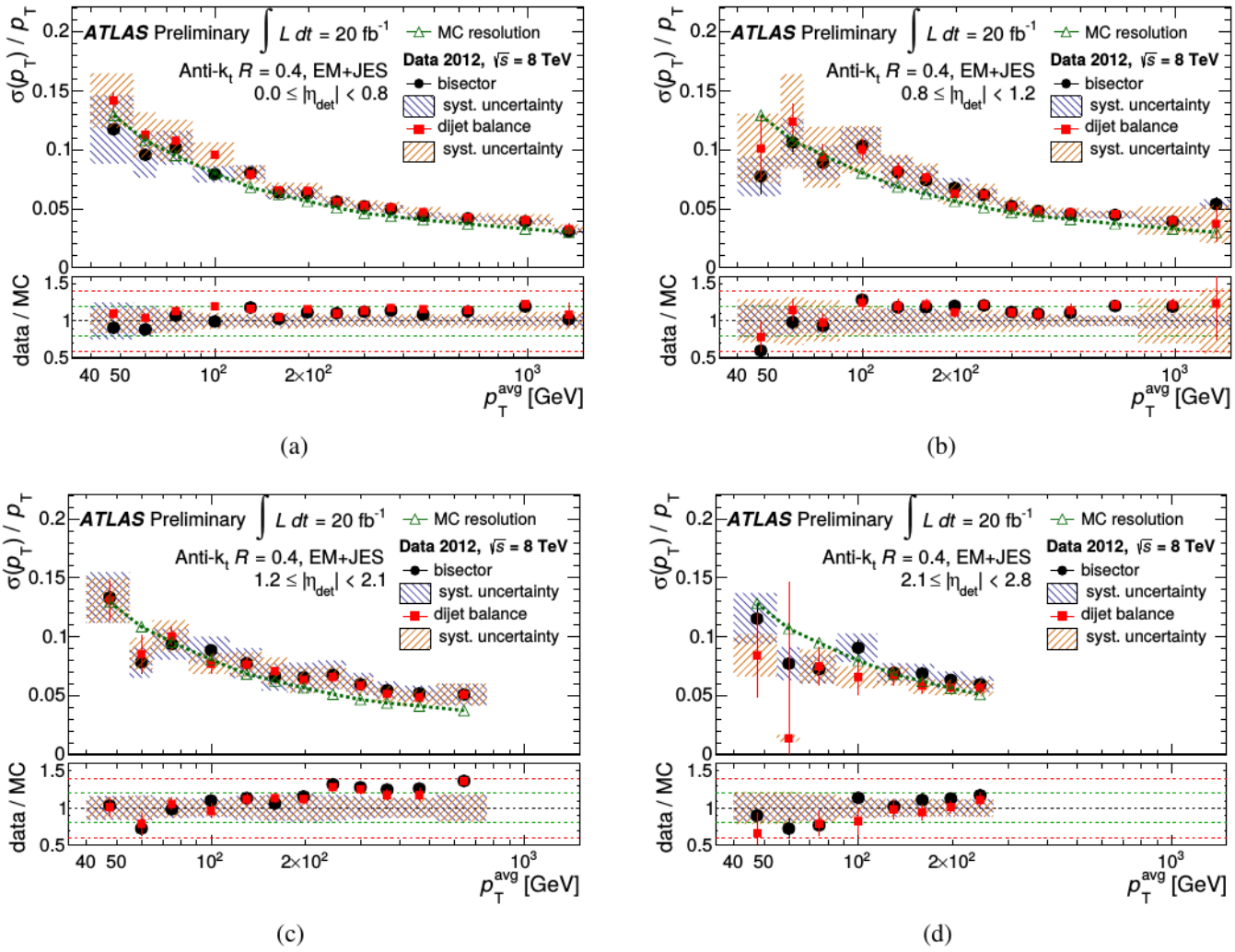

Figure 6.3: The JER as a function of p_{T} as obtained at 8 TeV for both the direct balance and the bisector method.[2]

6.3.1 Systematic uncertainties

The errors on the JER shown in this thesis only include uncertainties from fitting which uses the statistical uncertainties as an input. In general each step of the analysis has influence on the selected events and thus on the final result. To obtain the systematic uncertainties associated to it each cut could be varied and the results obtained from the dataset with the varied cut combined using the so-called bootstrap method. This is the list of possible sources for systematic uncertainties and the planned variation that could be used for the determination of the systematic uncertainties and the planned variations as well as possible ways to determine other systematic uncertainties:

- jet selection
  - $p_{T3} \leq 0.4\overline{p_T}$: vary the cut by 0.1
  - JVT: vary the cut by 0.1
- MC generator: try different MC generators such as Sherpa
- fit procedure:
  - range: vary the fit range for
    - $\boldsymbol{p_T^{\alpha}}$: $0.1 \cdot$ mean
    - $\boldsymbol{p_T^{\beta}}$: $0.1 \cdot$ width
  - truth matching: use ghost association

Additionally a closure test is needed. It determines the errors that were made in the general assumptions of the method. Therefore the obtained JER is applied to truth MC events and from these the JER is extracted as usual. In principle it should be the same as the applied JER. The difference between both is called the closure uncertainty.

6.3.2 Moving to Release 21 ATLAS software and including 2017 data

As mentioned before this thesis uses software and MC derived with release 20.7. During the time of this thesis the new release 21 has been produced. It should be possible to transfer the whole analysis as it is to release 21 and obtain the JER using the newest software update.

The data taken in 2017 has also been processed with software from release 21 so an update would also allow a determination of the JER for the newest dataset.

CHAPTER 7

Summary

In this thesis the implementation of the bisector method at ATLAS has been presented. It is based on calibrated jets and allows the resolution of the energy measurement due to detector effects to be determined. Dijet events are selected and studied in the transverse plane. The imbalances that occur here can be separated by geometrical considerations into a part that contains purely physics sources, σ_α, and a part that contains additionally detector and reconstruction effects, σ_β. By subtracting one from the other one can separate the detector contribution. To also get rid off imbalance sources that originate in the reconstruction a particle level correction is performed. Therefore this quantity is also derived for simulated jets that did not undergo a detector simulation. This should only include the jet reconstruction errors so it is subtracted in quadrature from the quantity derived for data or fully simulated Monte Carlo events. Therefore the pure detector uncertainty is obtained.

Obtaining the resolution of the two components α and β is done by first fitting a function to p_T^α and then convoluting it with a Gaussian and fitting p_T^β with just one free parameter which is the σ of this Gaussian.

This procedure provides a jet energy resolution that is consistent with and even slightly smaller than other methods such as the direct balance method. The advantage of this method is that it is mostly data-driven and thus does not heavily rely on simulations, except for the particle level corrections. A downside is that due to the shapes that have to be fitted in the process the fitting procedure is rather complicated. Nevertheless a method that provides consistent results has been found . The jet energy resolution for three jet collections has been computed. The results are shown versus $p_\mathbf{T}$ and $|\eta|$. One expectation was that the JER is falling with $p_\mathbf{T}$. This has been shown by fitting the assumed falling JER curve to it. Another expectation is that the shape of the detector is resembled by the dependence on $|\eta|$. Both expectations are fulfilled.

Bibliography

[1] ATLAS Collaboration,
Jet energy measurement with the ATLAS detector in proton–proton collisions at $\sqrt{s} = 7$ *TeV*,
Eur. Phys. J. C **73** (2013) 2304, arXiv: 1112.6426 [hep-ex] (cit. on pp. 1, 45, 46).

[2] ATLAS Collaboration, *Data-driven determination of the energy scale and resolution of jets reconstructed in the ATLAS calorimeters using dijet and multijet events at* $\sqrt{s} = 8$ *TeV*,
ATLAS-CONF-2015-017, 2015, URL: https://cds.cern.ch/record/2008678
(cit. on pp. 1, 61).

[3] M. Thomson, *Modern particle physics*, Cambridge University Press, 2013, ISBN: 9781107034266,
URL: http://www-spires.fnal.gov/spires/find/books/www?cl=QC793.2.T46::2013
(cit. on pp. 3, 7, 11).

[4] ATLAS Collaboration, *Observation of a new particle in the search for the Standard Model Higgs boson with the ATLAS detector at the LHC*, Phys. Lett. B **716** (2012) 1,
arXiv: 1207.7214 [hep-ex] (cit. on p. 4).

[5] CMS Collaboration,
Observation of a new boson at a mass of 125 GeV with the CMS experiment at the LHC,
Phys. Lett. B **716** (2012) 30, arXiv: 1207.7235 [hep-ex] (cit. on p. 4).

[6] C. Grupen, *Astroparticle Physics*, (2005) (cit. on p. 4).

[7] J. J. Thomson M.A. F.R.S., *XL. Cathode Rays*, The London, Edinburgh, and Dublin Philosophical Magazine and Journal of Science **44** (1897) 293,
eprint: https://doi.org/10.1080/14786449708621070,
URL: https://doi.org/10.1080/14786449708621070 (cit. on p. 4).

[8] W. Pauli, *Wissenschaftlicher Briefwechsel mit Bohr, Einstein, Heisenberg u.a. / Scientific Correspondence with Bohr, Einstein, Heisenberg a.o. -Band/Volume IV Teil/Part IV: 1957-1958*, (2005) (cit. on p. 4).

[9] M. E. Peskin and D. V. Schroeder, *An introduction to quantum field theory*, Includes exercises, Westview, 1995, URL: https://cds.cern.ch/record/257493 (cit. on p. 5).

[10] R. P. Feynman, *Space-Time Approach to Quantum Electrodynamics*, Phys. Rev. **76** (6 1949) 769,
URL: https://link.aps.org/doi/10.1103/PhysRev.76.769 (cit. on p. 5).

[11] Y. Fukuda et al., *Evidence for Oscillation of Atmospheric Neutrinos*,
Phys. Rev. Lett. **81** (8 1998) 1562,
URL: https://link.aps.org/doi/10.1103/PhysRevLett.81.1562 (cit. on p. 7).

[12] A. Zee, *Group Theory in a Nutshell for Physicists*, In a nutshell, Princeton University Press, 2016,
ISBN: 9780691162690, URL: https://books.google.de/books?id=FWkujgEACAAJ
(cit. on p. 8).

[13] S. Bethke, *The 2009 world average of α s*, The European Physical Journal C **64** (2009) 689, ISSN: 1434-6052, URL: https://doi.org/10.1140/epjc/s10052-009-1173-1 (cit. on p. 10).

[14] L. A. Harland-Lang et al., *Parton distributions in the LHC era: MMHT 2014 PDFs*, Eur. Phys. J. **C75** (2015) 204, arXiv: 1412.3989 [hep-ph] (cit. on p. 11).

[15] K. Rabbertz, *Jet Physics at the LHC*, Springer Tracts Mod. Phys. **268** (2017) pp.1 (cit. on pp. 9, 27).

[16] C. Patrignani et al., *Review of Particle Physics*, Chin. Phys. **C40** (2016) 100001 (cit. on pp. 13, 14).

[17] L. Evans and P. Bryant, *LHC Machine*, JINST **3** (2008) S08001 (cit. on pp. 13, 15).

[18] URL: http://www.lhc-facts.ch/ (cit. on p. 13).

[19] URL: https://lhc-machine-outreach.web.cern.ch/lhc-machine-outreach/lhc_in_pictures.htm (cit. on pp. 14, 15).

[20] URL: https://atlas.web.cern.ch/Atlas/GROUPS/DATAPREPARATION/PublicPlots/2016/DataSummary/figs/sumLumiByDay.png (cit. on p. 15).

[21] ATLAS Collaboration, *The ATLAS Experiment at the CERN Large Hadron Collider*, JINST **3** (2008) S08003 (cit. on p. 16).

[22] K. Sliwa, ""ATLAS Overview and Main Results"", *Proceedings, International School on High Energy Physics : Workshop on High Energy Physics in the near Future. (LISHEP 2013): Rio de Janeiro, Brazil, March 17-24, 2013*, 2013, arXiv: 1305.4551 [hep-ex], URL: http://inspirehep.net/record/1234234/files/arXiv:1305.4551.pdf (cit. on p. 16).

[23] URL: https://inspirehep.net/record/1294662/files/Figures%5C_T%5C_Coordinate.png (cit. on p. 17).

[24] J. Jentzsch, *Pixel detector modules performance for ATLAS IBL and future pixel detectors*, PhD thesis: Tech. U., Dortmund (main), 2015-03-27, URL: http://dx.doi.org/10.17877/DE290R-16400 (cit. on p. 18).

[25] M. A. Aginian, K. A. Ispirian and M. Ispiryan, *Gamma Ray Cherenkov-Transition Radiation*, EPL **104** (2013) 24002, arXiv: 1302.5208 [physics.ins-det] (cit. on p. 18).

[26] H. Kolanowski and N. Wermes, *Teilchendetektoren, Grundlagen und Anwendungen*, Springer Spektrum, 2016 (cit. on p. 18).

[27] ATLAS Collaboration, *The Run-2 ATLAS Trigger System*, tech. rep. ATL-DAQ-PROC-2016-003, CERN, 2016, URL: https://cds.cern.ch/record/2133909 (cit. on p. 20).

[28] ATLAS Collaboration, *Monte Carlo Calibration and Combination of In-situ Measurements of Jet Energy Scale, Jet Energy Resolution and Jet Mass in ATLAS*, ATLAS-CONF-2015-037, 2015, URL: https://cds.cern.ch/record/2044941 (cit. on pp. 22, 30, 59).

[29] T. Sjostrand, "Monte Carlo Tools", *Proceedings, 65th Scottish Universities Summer School in Physics: LHC Physics (SUSSP65): St. Andrews, UK, August 16-29, 2009*, 2009 309, arXiv: 0911.5286 [hep-ph], URL: https://inspirehep.net/record/838269/files/arXiv:0911.5286.pdf (cit. on p. 22).

[30] Sjöstrand, Torbjorn and Mrenna, Stephen and Skands, Peter Z., *A Brief Introduction to PYTHIA 8.1*, Comput. Phys. Commun. **178** (2008) 852, arXiv: 0710.3820 [hep-ph] (cit. on p. 22).

[31] S. Agostinelli et al., *GEANT4: A Simulation toolkit*, Nucl. Instrum. Meth. A **506** (2003) 250 (cit. on p. 22).

[32] S. Höche, "Introduction to parton-shower event generators", *Proceedings, Theoretical Advanced Study Institute in Elementary Particle Physics: Journeys Through the Precision Frontier: Amplitudes for Colliders (TASI 2014): Boulder, Colorado, June 2-27, 2014*, 2015 235, arXiv: 1411.4085 [hep-ph], URL: http://inspirehep.net/record/1328513/files/arXiv:1411.4085.pdf (cit. on p. 22).

[33] M. Cacciari, G. P. Salam and G. Soyez, *FastJet User Manual*, Eur. Phys. J. C **72** (2012) 1896, arXiv: 1111.6097 [hep-ph] (cit. on pp. 27, 31).

[34] ATLAS Collaboration, *Jet energy scale measurements and their systematic uncertainties in proton–proton collisions at $\sqrt{s}$ = 13 TeV with the ATLAS detector*, Phys. Rev. D **96** (2017) 072002, arXiv: 1703.09665 [hep-ex] (cit. on p. 27).

[35] M. Cacciari, G. P. Salam and G. Soyez, *The anti-k_t jet clustering algorithm*, JHEP **04** (2008) 063, arXiv: 0802.1189 [hep-ph] (cit. on p. 27).

[36] ATLAS Collaboration, *Topological cell clustering in the ATLAS calorimeters and its performance in LHC Run 1*, Eur. Phys. J. C **77** (2017) 490, arXiv: 1603.02934 [hep-ex] (cit. on pp. 28, 29).

[37] ATLAS Collaboration, *Jet reconstruction and performance using particle flow with the ATLAS Detector*, Eur. Phys. J. C **77** (2017) 466, arXiv: 1703.10485 [hep-ex] (cit. on pp. 29, 30).

[38] ATLAS Collaboration, *Tagging and suppression of pileup jets with the ATLAS detector*, ATLAS-CONF-2014-018, 2014, URL: https://cds.cern.ch/record/1700870 (cit. on p. 31).

[39] V. Lendermann et al., *Combining Triggers in HEP Data Analysis*, Nucl. Instrum. Meth. **A604** (2009) 707, arXiv: 0901.4118 [hep-ex] (cit. on p. 40).

[40] URL: https://atlas-lumicalc.cern.ch/ (cit. on p. 42).

[41] W. R. Inc., *Mathematica, Version 11.3*, Champaign, IL, 2018 (cit. on p. 48).

APPENDIX A

Additional information on the used datasets

All events are labeled with different "ptags" which makes it easier to select events based on the status of the reconstruction. The ptags used can be found in table A.1.

datataking periods	2016 B-L			
ptags data	p2667	p2689	p2769	p2840
ptag MC	p2666			

Table A.1: Information on the used datasets.

GRL	data16_13TeV.periodAllYear_DetStatus-v88-pro20-21_DQDefects-00-02-04_ PHYS_StandardGRL_All_Good_25ns.xml
AntiKt4LCTopo.Config:	JES_data2016_data2015_Recommendation_Dec2016.config
AntiKt4LCTopo.CalibSeq:	JetArea_Residual_Origin_EtaJES_GSC
AntiKt4EMTopo.Config:	JES_data2016_data2015_Recommendation_Dec2016.config
AntiKt4EMTopo.CalibSeq:	JetArea_Residual_Origin_EtaJES_GSC
AntiKt4EMPFlow.Config:	JES_MC15cRecommendation_PFlow_Aug2016.config
AntiKt4EMPFlow.CalibSeq:	JetArea_Residual_EtaJES_GSC

Table A.2: Information on the used configuration files and good run list.

JZ	filter efficiency	n events created	cross-section	weight
0	9.8132×10^{-1}	1 999 400	7.8420×10^{7}	1.26552×10^{6}
1	6.7075×10^{-4}	1 999 000	7.8420×10^{7}	865.18
2	3.3432×10^{-4}	1 994 600	2.433×10^{6}	13.4085
3	3.2012×10^{-4}	7 884 500	2.6454×10^{4}	0.0353152
4	5.3156×10^{-4}	7 979 800	2.5463×10^{2}	0.000557701
5	9.2440×10^{-4}	7 977 600	4.553	1.73467×10^{-5}
6	9.4071×10^{-4}	1 893 400	2.5753×10^{-1}	4.207×10^{-6}
7	3.9280×10^{-4}	1 770 200	1.6215×10^{-2}	1.18304×10^{-7}
8	1.0176×10^{-2}	1 743 200	6.2502×10^{-4}	1.19965×10^{-7}
9	1.2076×10^{-2}	1 813 200	1.9639×10^{-5}	4.3006×10^{-9}
10	5.9087×10^{-3}	1 996 000	1.196×10^{-6}	1.16411×10^{-10}
11	2.6761×10^{-3}	1 993 200	4.2258×10^{-8}	1.86549×10^{-12}
12	4.2592×10^{-4}	1 974 600	1.0370×10^{-9}	7.35461×10^{-15}

Table A.3: Information on the used weights for MC.

APPENDIX **B**

Data/MC-comparison

In this appendix more comparisons of $\cos(\Phi_{i,j})$ between data and MC can be seen.

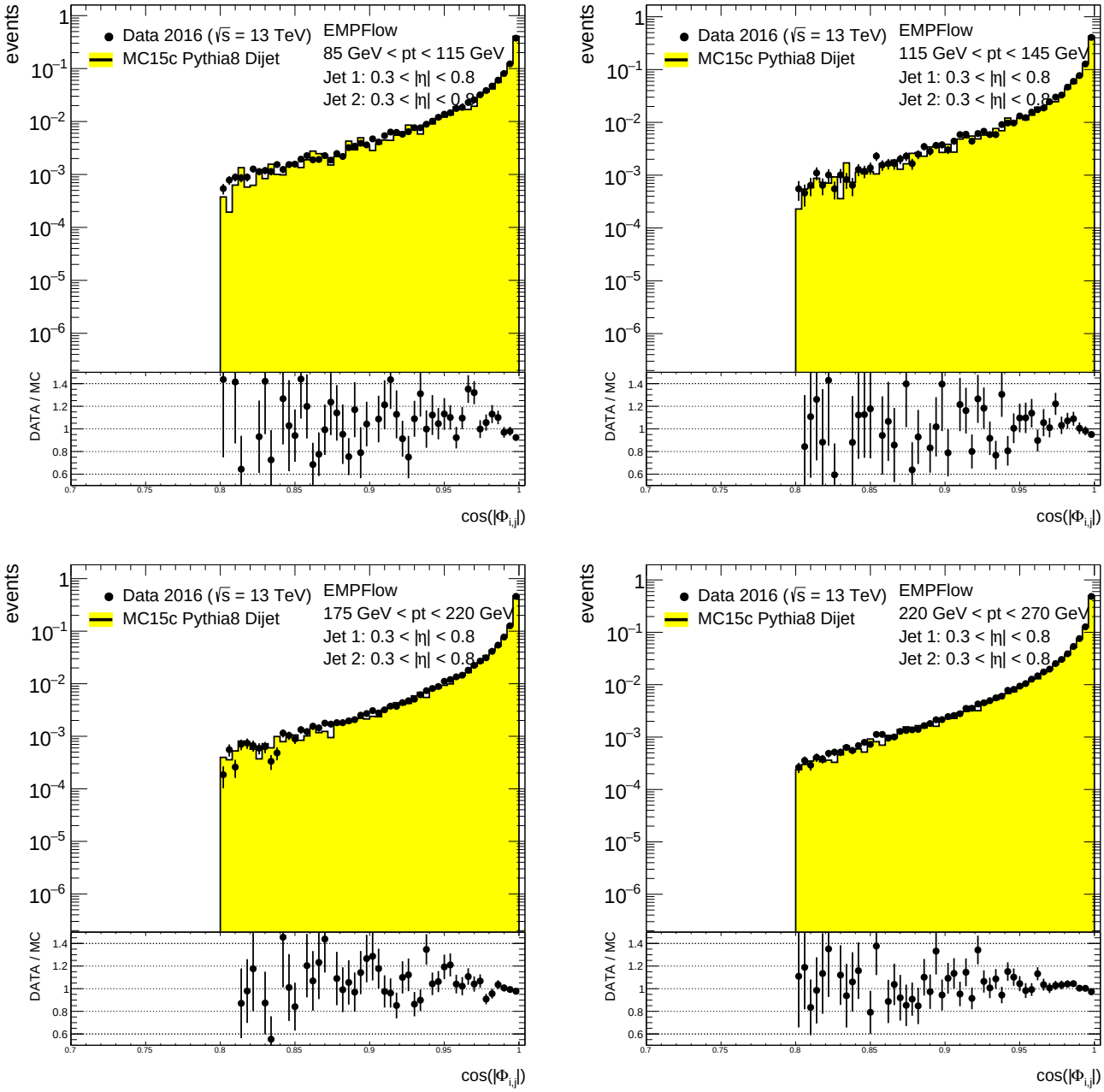

Figure B.1: Data MC comparisons of $\cos(\Phi_{i,j})$ for different $p_{\mathbf{T}}$ regions.

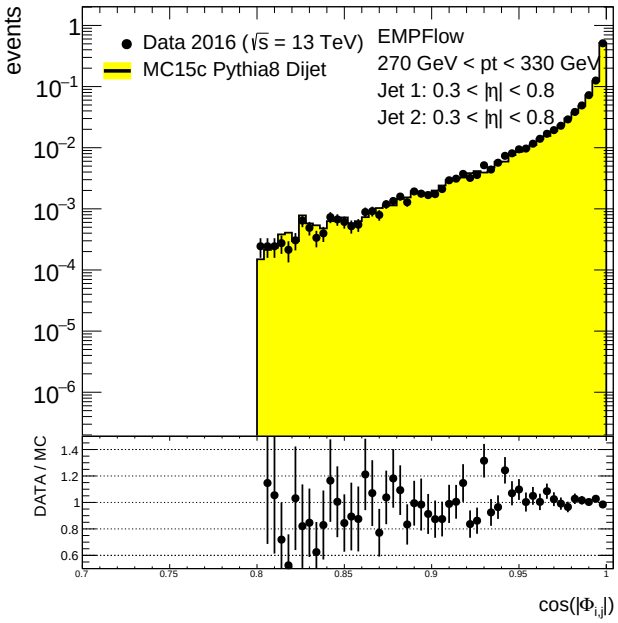
Data 2016 (√s = 13 TeV)
MC15c Pythia8 Dijet
EMPFlow
270 GeV < pt < 330 GeV
Jet 1: 0.3 < |η| < 0.8
Jet 2: 0.3 < |η| < 0.8
events
DATA / MC
cos(|Φ_{i,j}|)

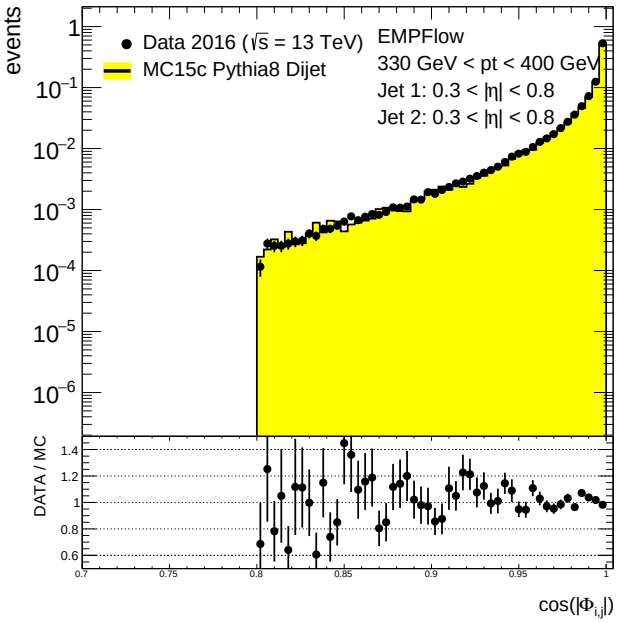
Data 2016 (√s = 13 TeV)
MC15c Pythia8 Dijet
EMPFlow
330 GeV < pt < 400 GeV
Jet 1: 0.3 < |η| < 0.8
Jet 2: 0.3 < |η| < 0.8
events
DATA / MC
cos(|Φ_{i,j}|)

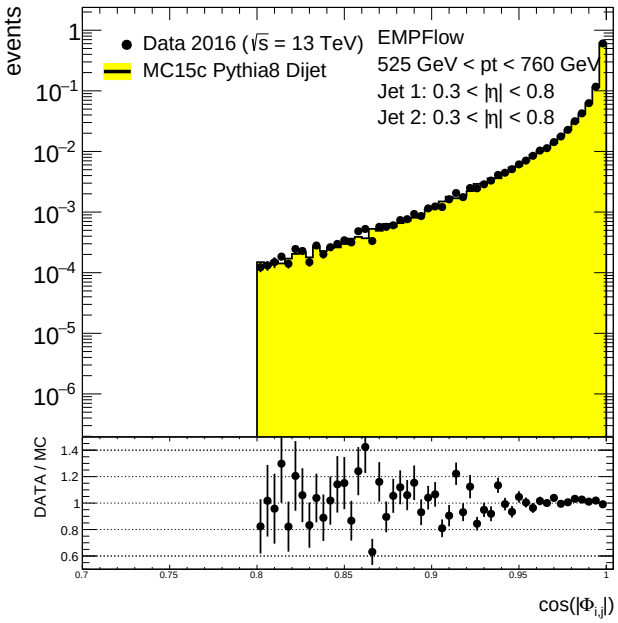
Data 2016 (√s = 13 TeV)
MC15c Pythia8 Dijet
EMPFlow
525 GeV < pt < 760 GeV
Jet 1: 0.3 < |η| < 0.8
Jet 2: 0.3 < |η| < 0.8
events
DATA / MC
cos(|Φ_{i,j}|)

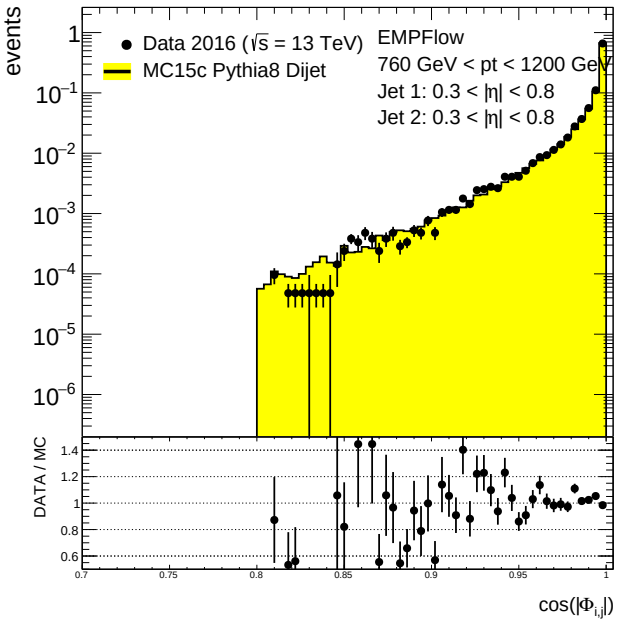
Data 2016 (√s = 13 TeV)
MC15c Pythia8 Dijet
EMPFlow
760 GeV < pt < 1200 GeV
Jet 1: 0.3 < |η| < 0.8
Jet 2: 0.3 < |η| < 0.8
events
DATA / MC
cos(|Φ_{i,j}|)

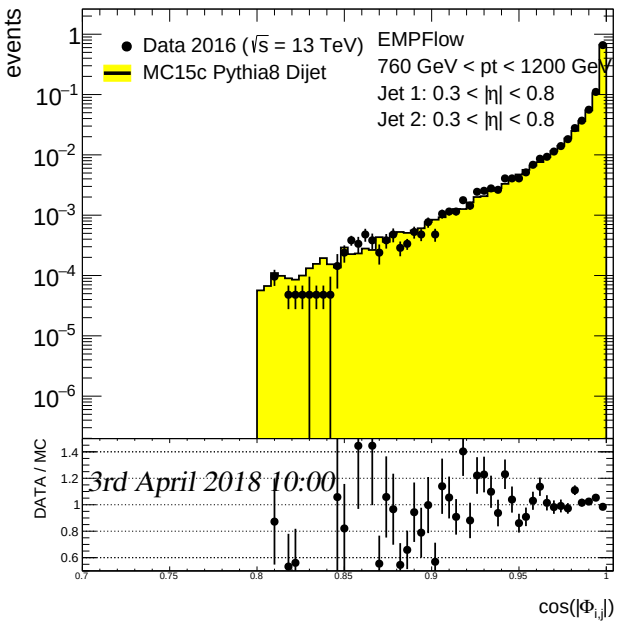
Data 2016 (√s = 13 TeV)
MC15c Pythia8 Dijet
EMPFlow
760 GeV < pt < 1200 GeV
Jet 1: 0.3 < |η| < 0.8
Jet 2: 0.3 < |η| < 0.8
events
DATA / MC
cos(|Φ_{i,j}|)

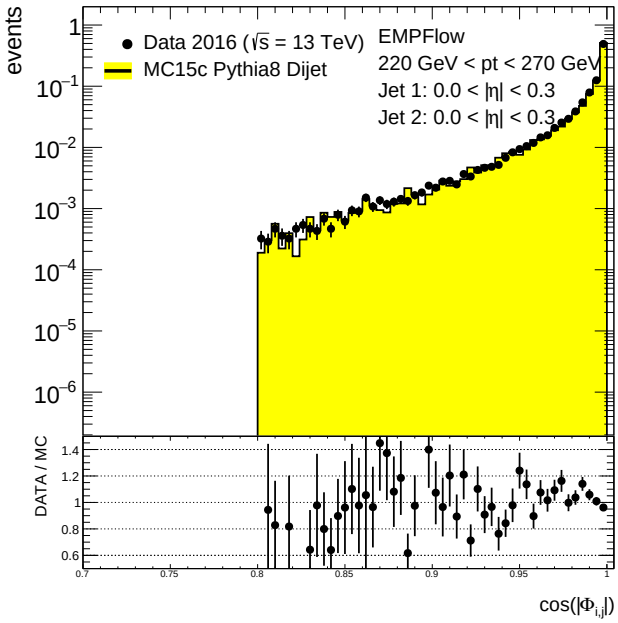
Data 2016 (√s = 13 TeV)
MC15c Pythia8 Dijet
EMPFlow
220 GeV < pt < 270 GeV
Jet 1: 0.0 < |η| < 0.3
Jet 2: 0.0 < |η| < 0.3
events
DATA / MC
cos(|Φ_{i,j}|)

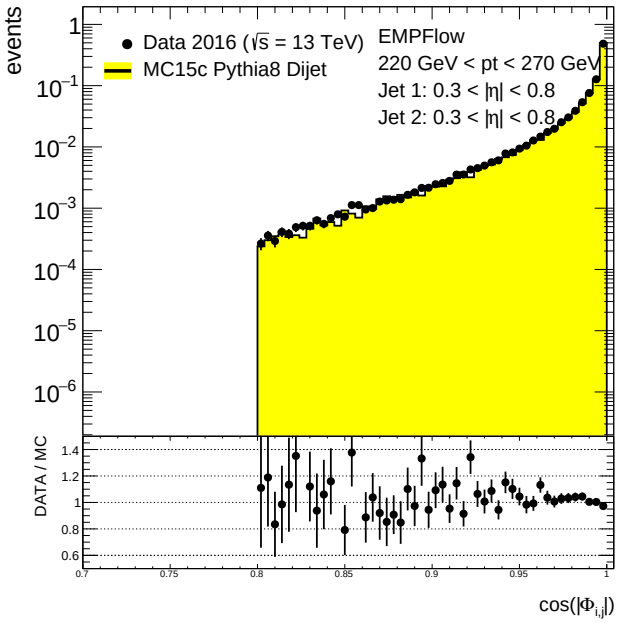
Data 2016 (√s = 13 TeV)
MC15c Pythia8 Dijet
EMPFlow
220 GeV < pt < 270 GeV
Jet 1: 0.3 < |η| < 0.8
Jet 2: 0.3 < |η| < 0.8
events
DATA / MC
cos(|Φ_{i,j}|)

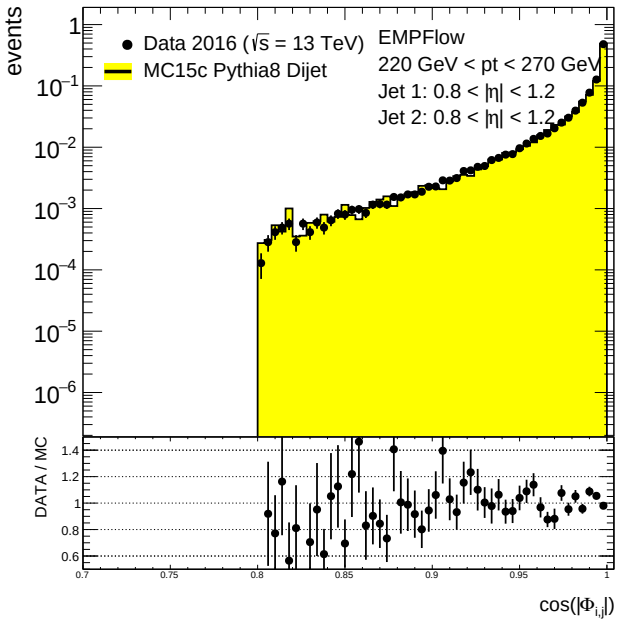
Data 2016 (√s = 13 TeV)
MC15c Pythia8 Dijet
EMPFlow
220 GeV < pt < 270 GeV
Jet 1: 0.8 < |η| < 1.2
Jet 2: 0.8 < |η| < 1.2
events
DATA / MC
cos(|Φ_{i,j}|)

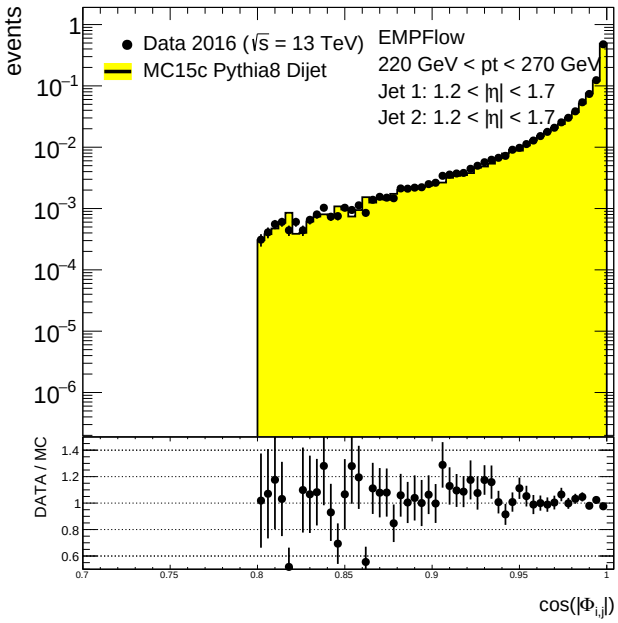
Data 2016 (√s = 13 TeV)
MC15c Pythia8 Dijet
EMPFlow
220 GeV < pt < 270 GeV
Jet 1: 1.2 < |η| < 1.7
Jet 2: 1.2 < |η| < 1.7
events
DATA / MC
cos(|Φ_{i,j}|)

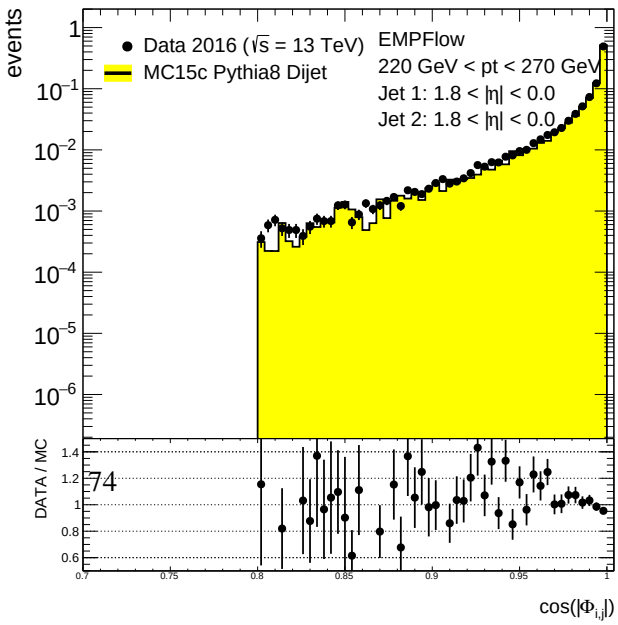
Data 2016 (√s = 13 TeV)
MC15c Pythia8 Dijet
EMPFlow
220 GeV < pt < 270 GeV
Jet 1: 1.8 < |η| < 0.0
Jet 2: 1.8 < |η| < 0.0
events
DATA / MC
cos(|Φ_{i,j}|)

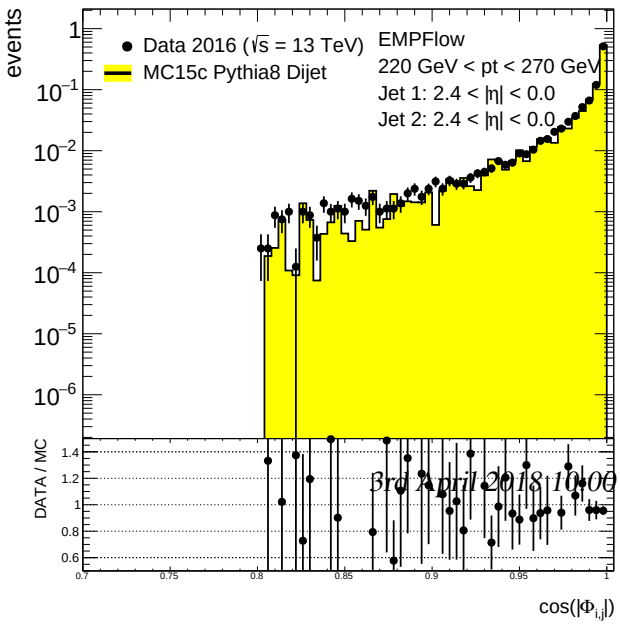
Data 2016 (√s = 13 TeV)
MC15c Pythia8 Dijet
EMPFlow
220 GeV < pt < 270 GeV
Jet 1: 2.4 < |η| < 0.0
Jet 2: 2.4 < |η| < 0.0
events
DATA / MC
cos(|Φ_{i,j}|)

APPENDIX C

Additional fits

In this appendix fits for all jet collections can be seen for data and MC.

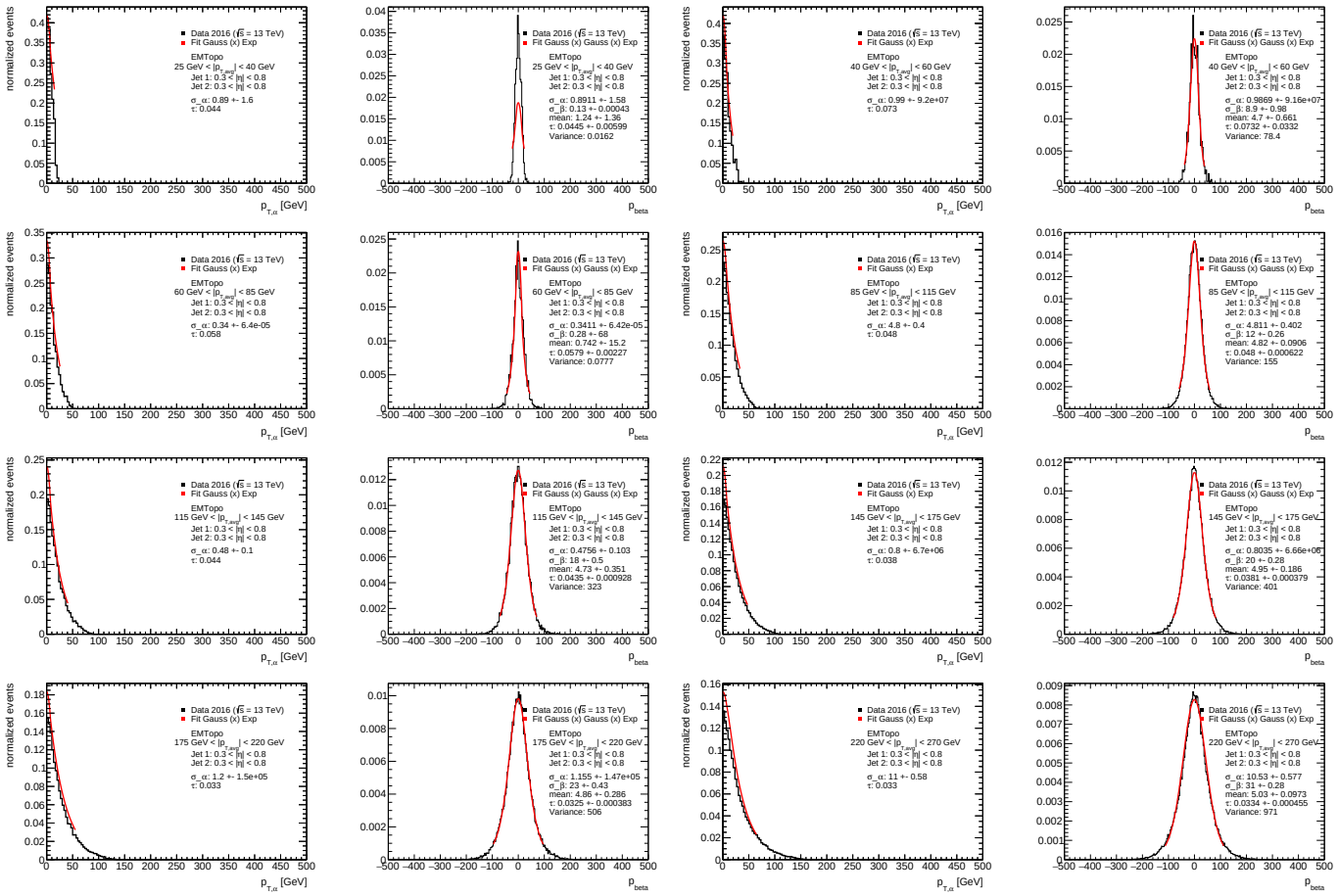

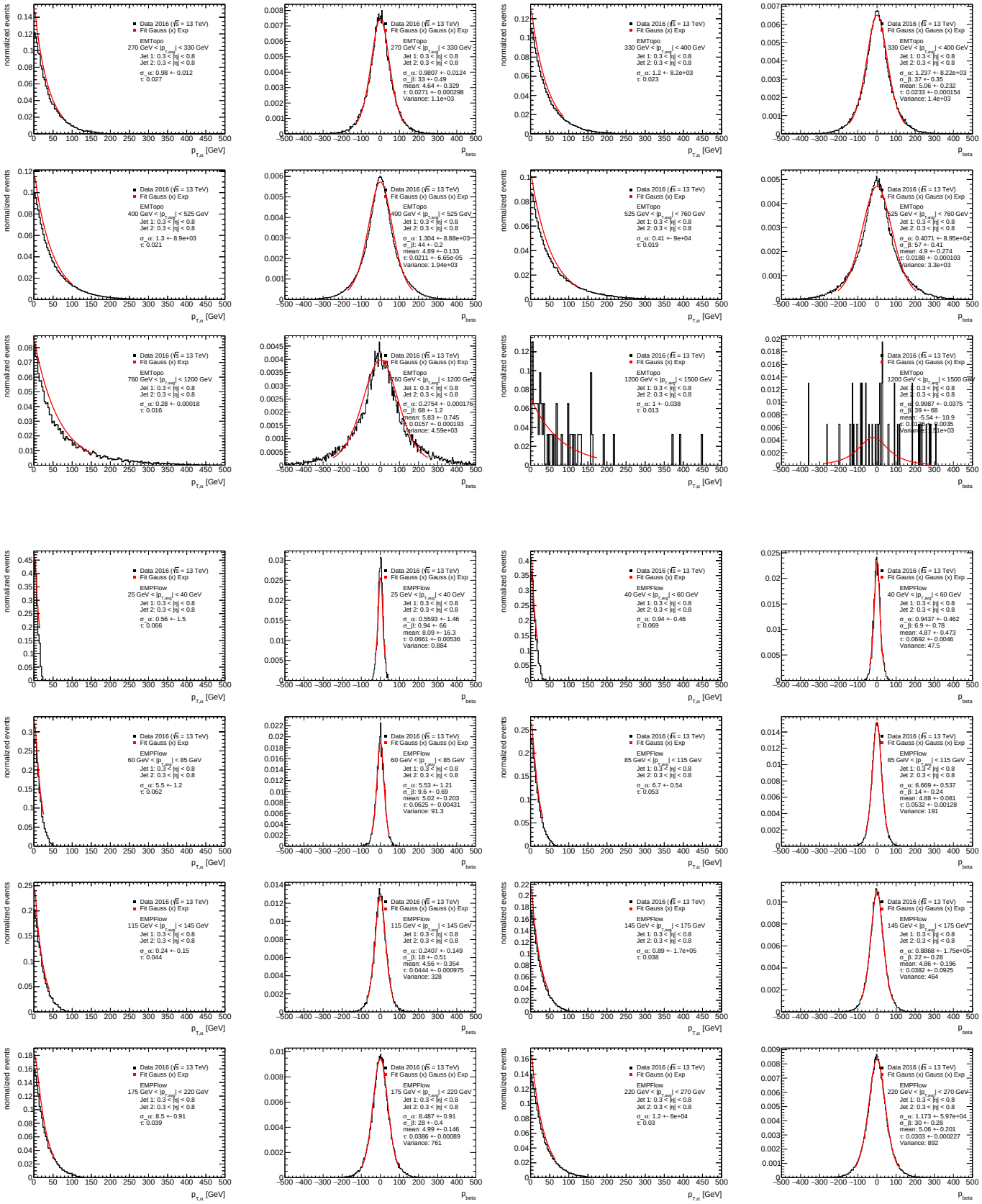
normalized events
Data 2016 (√s = 13 TeV)
Fit Gauss (x) Exp
Fit Gauss (x) Gauss (x) Exp
EMTopo
EMPFlow
Jet 1: 0.3 < |η| < 0.8
Jet 2: 0.3 < |η| < 0.8
p_T,jet [GeV]
p_beta

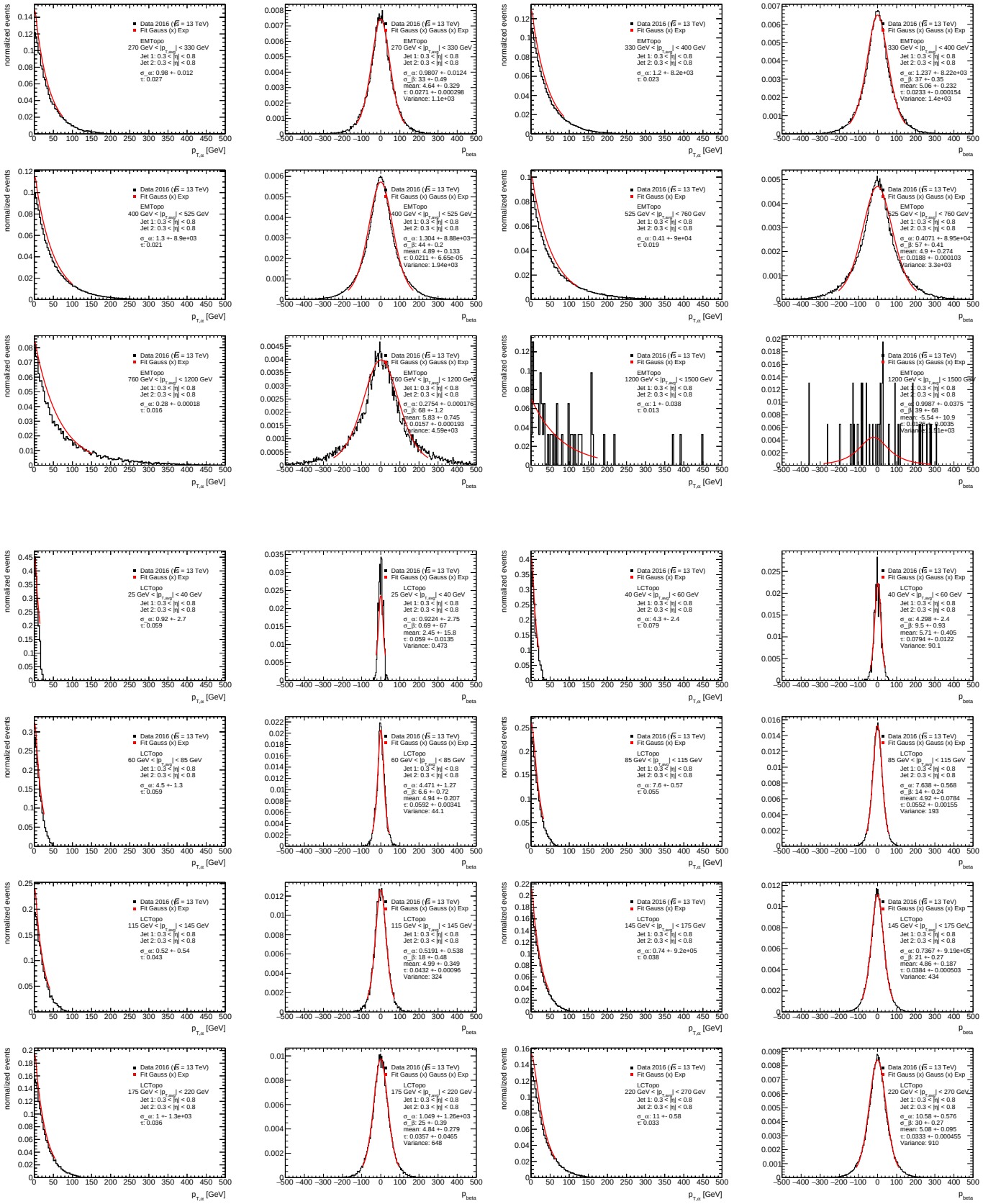
normalized events
Data 2016 (√s = 13 TeV)
Fit Gauss (x) Exp
Fit Gauss (x) Gauss (x) Exp
EMTopo
LCTopo
Jet 1: 0.3 < |η| < 0.8
Jet 2: 0.3 < |η| < 0.8
p_T,α [GeV]
p_beta

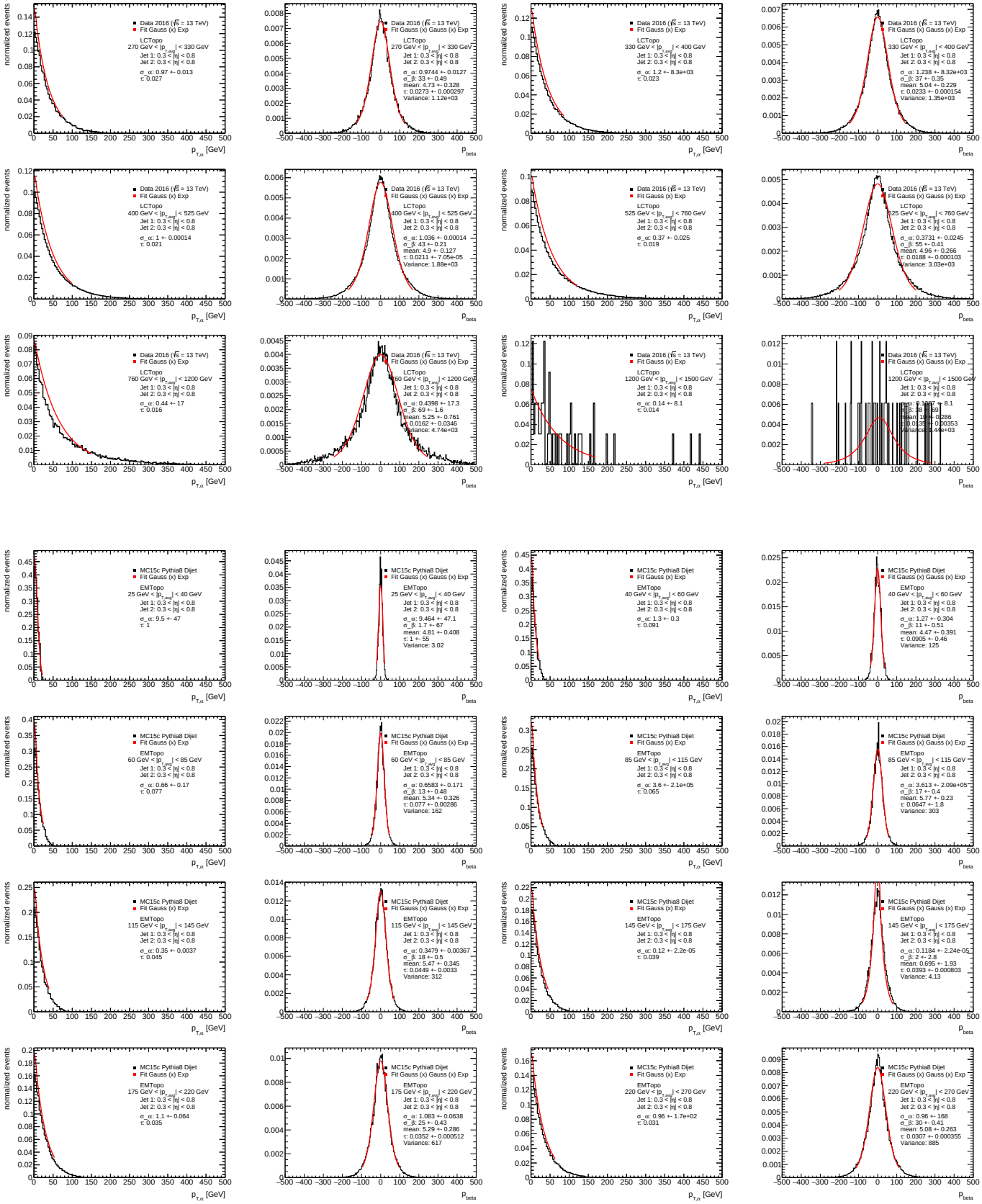
Data 2016 (√s = 13 TeV)
Fit Gauss (x) Exp
LCTopo
270 GeV < |p_T,avg| < 330 GeV
Jet 1: 0.3 < |η| < 0.8
Jet 2: 0.3 < |η| < 0.8
σ_α: 0.97 +- 0.013
τ: 0.027
Data 2016 (√s = 13 TeV)
Fit Gauss (x) Gauss (x) Exp
LCTopo
270 GeV < |p_T,avg| < 330 GeV
Jet 1: 0.3 < |η| < 0.8
Jet 2: 0.3 < |η| < 0.8
σ_α: 0.9744 +- 0.0127
σ_β: 33 +- 0.49
mean: 4.73 +- 0.328
τ: 0.0273 +- 0.000297
Variance: 1.12e+03
Data 2016 (√s = 13 TeV)
Fit Gauss (x) Exp
LCTopo
330 GeV < |p_T,avg| < 400 GeV
Jet 1: 0.3 < |η| < 0.8
Jet 2: 0.3 < |η| < 0.8
σ_α: 1.2 +- 8.3e+03
τ: 0.023
Data 2016 (√s = 13 TeV)
Fit Gauss (x) Gauss (x) Exp
LCTopo
330 GeV < |p_T,avg| < 400 GeV
Jet 1: 0.3 < |η| < 0.8
Jet 2: 0.3 < |η| < 0.8
σ_α: 1.238 +- 8.32e+03
σ_β: 37 +- 0.35
mean: 5.04 +- 0.229
τ: 0.0233 +- 0.000154
Variance: 1.35e+03
Data 2016 (√s = 13 TeV)
Fit Gauss (x) Exp
LCTopo
400 GeV < |p_T,avg| < 525 GeV
Jet 1: 0.3 < |η| < 0.8
Jet 2: 0.3 < |η| < 0.8
σ_α: 1 +- 0.00014
τ: 0.021
Data 2016 (√s = 13 TeV)
Fit Gauss (x) Gauss (x) Exp
LCTopo
400 GeV < |p_T,avg| < 525 GeV
Jet 1: 0.3 < |η| < 0.8
Jet 2: 0.3 < |η| < 0.8
σ_α: 1.036 +- 0.00014
σ_β: 43 +- 0.21
mean: 4.9 +- 0.127
τ: 0.0211 +- 7.05e-05
Variance: 1.88e+03
Data 2016 (√s = 13 TeV)
Fit Gauss (x) Exp
LCTopo
525 GeV < |p_T,avg| < 760 GeV
Jet 1: 0.3 < |η| < 0.8
Jet 2: 0.3 < |η| < 0.8
σ_α: 0.37 +- 0.025
τ: 0.019
Data 2016 (√s = 13 TeV)
Fit Gauss (x) Gauss (x) Exp
LCTopo
525 GeV < |p_T,avg| < 760 GeV
Jet 1: 0.3 < |η| < 0.8
Jet 2: 0.3 < |η| < 0.8
σ_α: 0.3731 +- 0.0245
σ_β: 55 +- 0.41
mean: 4.96 +- 0.266
τ: 0.0188 +- 0.000103
Variance: 3.03e+03
Data 2016 (√s = 13 TeV)
Fit Gauss (x) Exp
LCTopo
760 GeV < |p_T,avg| < 1200 GeV
Jet 1: 0.3 < |η| < 0.8
Jet 2: 0.3 < |η| < 0.8
σ_α: 0.44 +- 17
τ: 0.016
Data 2016 (√s = 13 TeV)
Fit Gauss (x) Gauss (x) Exp
LCTopo
760 GeV < |p_T,avg| < 1200 GeV
Jet 1: 0.3 < |η| < 0.8
Jet 2: 0.3 < |η| < 0.8
σ_α: 0.4398 +- 17.3
σ_β: 69 +- 1.6
mean: 5.25 +- 0.761
τ: 0.0162 +- 0.0346
Variance: 4.74e+03
Data 2016 (√s = 13 TeV)
Fit Gauss (x) Exp
LCTopo
1200 GeV < |p_T,avg| < 1500 GeV
Jet 1: 0.3 < |η| < 0.8
Jet 2: 0.3 < |η| < 0.8
σ_α: 0.14 +- 8.1
τ: 0.014
Data 2016 (√s = 13 TeV)
Fit Gauss (x) Gauss (x) Exp
LCTopo
1200 GeV < |p_T,avg| < 1500 GeV
Jet 1: 0.3 < |η| < 0.8
Jet 2: 0.3 < |η| < 0.8
σ_α: 0.1807 +- 8.1
σ_β: 88 +- 89
mean: 1.84 +- 0.286
τ: 0.0135 +- 0.00353
Variance: 2.44e+03
MC15c Pythia8 Dijet
Fit Gauss (x) Exp
EMTopo
25 GeV < |p_T,avg| < 40 GeV
Jet 1: 0.3 < |η| < 0.8
Jet 2: 0.3 < |η| < 0.8
σ_α: 9.5 +- 47
τ: 1
MC15c Pythia8 Dijet
Fit Gauss (x) Gauss (x) Exp
EMTopo
25 GeV < |p_T,avg| < 40 GeV
Jet 1: 0.3 < |η| < 0.8
Jet 2: 0.3 < |η| < 0.8
σ_α: 9.464 +- 47.1
σ_β: 1.7 +- 67
mean: 4.81 +- 0.408
τ: 1 +- 55
Variance: 3.02
MC15c Pythia8 Dijet
Fit Gauss (x) Exp
EMTopo
40 GeV < |p_T,avg| < 60 GeV
Jet 1: 0.3 < |η| < 0.8
Jet 2: 0.3 < |η| < 0.8
σ_α: 1.3 +- 0.3
τ: 0.091
MC15c Pythia8 Dijet
Fit Gauss (x) Gauss (x) Exp
EMTopo
40 GeV < |p_T,avg| < 60 GeV
Jet 1: 0.3 < |η| < 0.8
Jet 2: 0.3 < |η| < 0.8
σ_α: 1.27 +- 0.304
σ_β: 11 +- 0.51
mean: 4.47 +- 0.391
τ: 0.0905 +- 0.46
Variance: 125
MC15c Pythia8 Dijet
Fit Gauss (x) Exp
EMTopo
60 GeV < |p_T,avg| < 85 GeV
Jet 1: 0.3 < |η| < 0.8
Jet 2: 0.3 < |η| < 0.8
σ_α: 0.66 +- 0.17
τ: 0.077
MC15c Pythia8 Dijet
Fit Gauss (x) Gauss (x) Exp
EMTopo
60 GeV < |p_T,avg| < 85 GeV
Jet 1: 0.3 < |η| < 0.8
Jet 2: 0.3 < |η| < 0.8
σ_α: 0.6583 +- 0.171
σ_β: 13 +- 0.48
mean: 5.34 +- 0.326
τ: 0.077 +- 0.00286
Variance: 162
MC15c Pythia8 Dijet
Fit Gauss (x) Exp
EMTopo
85 GeV < |p_T,avg| < 115 GeV
Jet 1: 0.3 < |η| < 0.8
Jet 2: 0.3 < |η| < 0.8
σ_α: 3.6 +- 2.1e+05
τ: 0.065
MC15c Pythia8 Dijet
Fit Gauss (x) Gauss (x) Exp
EMTopo
85 GeV < |p_T,avg| < 115 GeV
Jet 1: 0.3 < |η| < 0.8
Jet 2: 0.3 < |η| < 0.8
σ_α: 3.613 +- 2.09e+05
σ_β: 17 +- 0.4
mean: 5.77 +- 0.23
τ: 0.0647 +- 1.8
Variance: 303
MC15c Pythia8 Dijet
Fit Gauss (x) Exp
EMTopo
115 GeV < |p_T,avg| < 145 GeV
Jet 1: 0.3 < |η| < 0.8
Jet 2: 0.3 < |η| < 0.8
σ_α: 0.35 +- 0.0037
τ: 0.045
MC15c Pythia8 Dijet
Fit Gauss (x) Gauss (x) Exp
EMTopo
115 GeV < |p_T,avg| < 145 GeV
Jet 1: 0.3 < |η| < 0.8
Jet 2: 0.3 < |η| < 0.8
σ_α: 0.3479 +- 0.00367
σ_β: 18 +- 0.5
mean: 5.47 +- 0.345
τ: 0.0449 +- 0.0033
Variance: 312
MC15c Pythia8 Dijet
Fit Gauss (x) Exp
EMTopo
145 GeV < |p_T,avg| < 175 GeV
Jet 1: 0.3 < |η| < 0.8
Jet 2: 0.3 < |η| < 0.8
σ_α: 0.12 +- 2.2e-05
τ: 0.039
MC15c Pythia8 Dijet
Fit Gauss (x) Gauss (x) Exp
EMTopo
145 GeV < |p_T,avg| < 175 GeV
Jet 1: 0.3 < |η| < 0.8
Jet 2: 0.3 < |η| < 0.8
σ_α: 0.1184 +- 2.24e-05
σ_β: 2 +- 2.8
mean: 0.695 +- 1.93
τ: 0.0393 +- 0.000803
Variance: 4.13
MC15c Pythia8 Dijet
Fit Gauss (x) Exp
EMTopo
175 GeV < |p_T,avg| < 220 GeV
Jet 1: 0.3 < |η| < 0.8
Jet 2: 0.3 < |η| < 0.8
σ_α: 1.1 +- 0.064
τ: 0.035
MC15c Pythia8 Dijet
Fit Gauss (x) Gauss (x) Exp
EMTopo
175 GeV < |p_T,avg| < 220 GeV
Jet 1: 0.3 < |η| < 0.8
Jet 2: 0.3 < |η| < 0.8
σ_α: 1.083 +- 0.0638
σ_β: 25 +- 0.43
mean: 5.29 +- 0.286
τ: 0.0352 +- 0.000512
Variance: 617
MC15c Pythia8 Dijet
Fit Gauss (x) Exp
EMTopo
220 GeV < |p_T,avg| < 270 GeV
Jet 1: 0.3 < |η| < 0.8
Jet 2: 0.3 < |η| < 0.8
σ_α: 0.96 +- 1.7e+02
τ: 0.031
MC15c Pythia8 Dijet
Fit Gauss (x) Gauss (x) Exp
EMTopo
220 GeV < |p_T,avg| < 270 GeV
Jet 1: 0.3 < |η| < 0.8
Jet 2: 0.3 < |η| < 0.8
σ_α: 0.96 +- 168
σ_β: 30 +- 0.41
mean: 5.08 +- 0.263
τ: 0.0307 +- 0.000355
Variance: 885
normalized events
p_T,jet [GeV]
p_beta

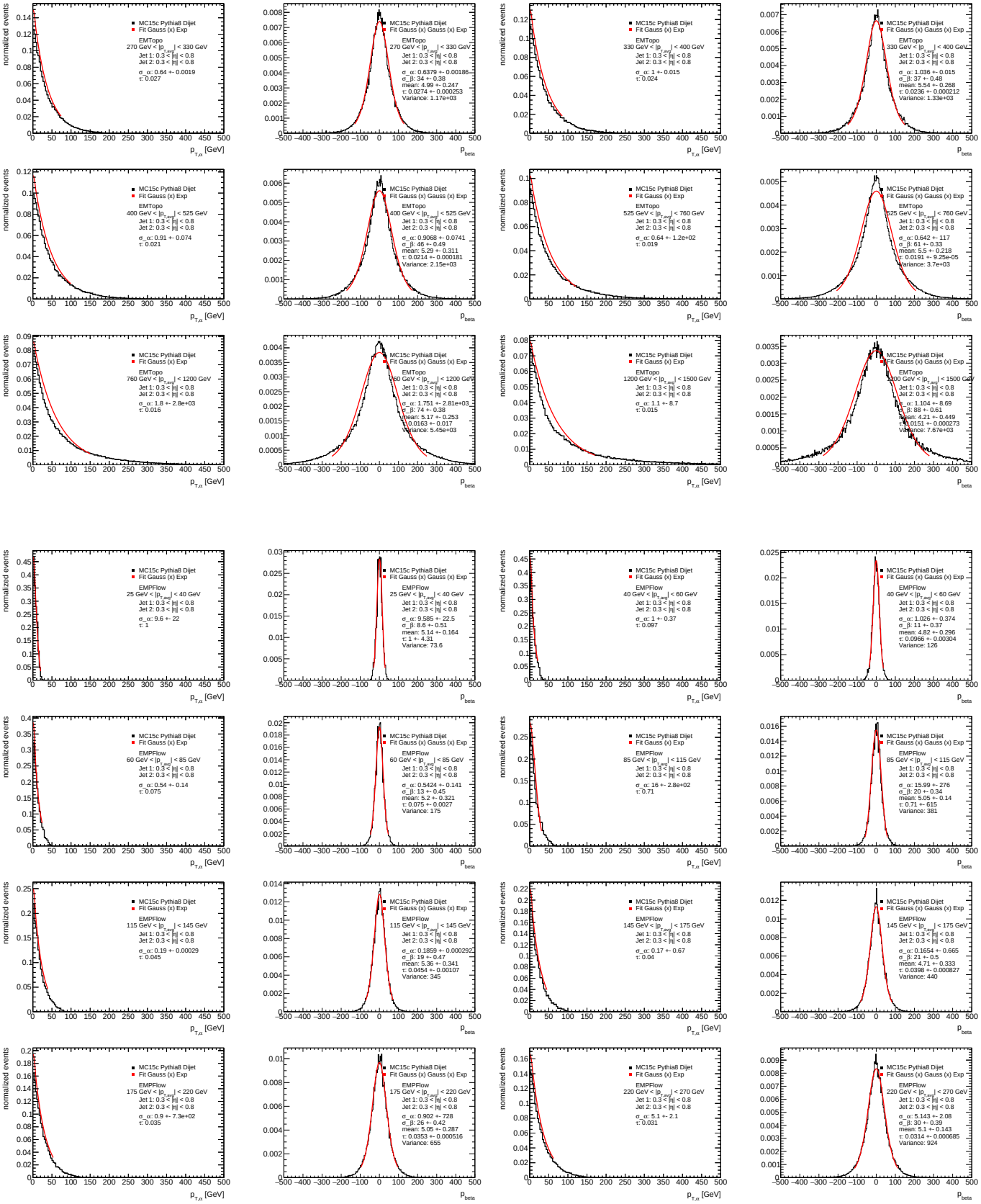
normalized events
MC15c Pythia8 Dijet
Fit Gauss (x) Exp
EMTopo
270 GeV < |p_T,avg| < 330 GeV
Jet 1: 0.3 < |η| < 0.8
Jet 2: 0.3 < |η| < 0.8
σ_α: 0.64 +- 0.0019
τ: 0.027
p_T,α [GeV]
MC15c Pythia8 Dijet
Fit Gauss (x) Gauss (x) Exp
EMTopo
270 GeV < |p_T,avg| < 330 GeV
Jet 1: 0.3 < |η| < 0.8
Jet 2: 0.3 < |η| < 0.8
σ_α: 0.6379 +- 0.00186
σ_β: 34 +- 0.38
mean: 4.99 +- 0.247
τ: 0.0274 +- 0.000253
Variance: 1.17e+03
p_beta
MC15c Pythia8 Dijet
Fit Gauss (x) Exp
EMTopo
330 GeV < |p_T,avg| < 400 GeV
Jet 1: 0.3 < |η| < 0.8
Jet 2: 0.3 < |η| < 0.8
σ_α: 1 +- 0.015
τ: 0.024
p_T,α [GeV]
MC15c Pythia8 Dijet
Fit Gauss (x) Gauss (x) Exp
EMTopo
330 GeV < |p_T,avg| < 400 GeV
Jet 1: 0.3 < |η| < 0.8
Jet 2: 0.3 < |η| < 0.8
σ_α: 1.036 +- 0.015
σ_β: 37 +- 0.48
mean: 5.54 +- 0.268
τ: 0.0236 +- 0.000212
Variance: 1.33e+03
p_beta
MC15c Pythia8 Dijet
Fit Gauss (x) Exp
EMTopo
400 GeV < |p_T,avg| < 525 GeV
Jet 1: 0.3 < |η| < 0.8
Jet 2: 0.3 < |η| < 0.8
σ_α: 0.91 +- 0.074
τ: 0.021
p_T,α [GeV]
MC15c Pythia8 Dijet
Fit Gauss (x) Gauss (x) Exp
EMTopo
400 GeV < |p_T,avg| < 525 GeV
Jet 1: 0.3 < |η| < 0.8
Jet 2: 0.3 < |η| < 0.8
σ_α: 0.9068 +- 0.0741
σ_β: 46 +- 0.49
mean: 5.29 +- 0.311
τ: 0.0214 +- 0.000181
Variance: 2.15e+03
p_beta
MC15c Pythia8 Dijet
Fit Gauss (x) Exp
EMTopo
525 GeV < |p_T,avg| < 760 GeV
Jet 1: 0.3 < |η| < 0.8
Jet 2: 0.3 < |η| < 0.8
σ_α: 0.64 +- 1.2e+02
τ: 0.019
p_T,α [GeV]
MC15c Pythia8 Dijet
Fit Gauss (x) Gauss (x) Exp
EMTopo
525 GeV < |p_T,avg| < 760 GeV
Jet 1: 0.3 < |η| < 0.8
Jet 2: 0.3 < |η| < 0.8
σ_α: 0.642 +- 117
σ_β: 61 +- 0.33
mean: 5.5 +- 0.218
τ: 0.0191 +- 9.25e-05
Variance: 3.7e+03
p_beta
MC15c Pythia8 Dijet
Fit Gauss (x) Exp
EMTopo
760 GeV < |p_T,avg| < 1200 GeV
Jet 1: 0.3 < |η| < 0.8
Jet 2: 0.3 < |η| < 0.8
σ_α: 1.8 +- 2.8e+03
τ: 0.016
p_T,α [GeV]
MC15c Pythia8 Dijet
Fit Gauss (x) Gauss (x) Exp
EMTopo
760 GeV < |p_T,avg| < 1200 GeV
Jet 1: 0.3 < |η| < 0.8
Jet 2: 0.3 < |η| < 0.8
σ_α: 1.751 +- 2.81e+03
σ_β: 74 +- 0.38
mean: 5.17 +- 0.253
τ: 0.0163 +- 0.017
Variance: 5.45e+03
p_beta
MC15c Pythia8 Dijet
Fit Gauss (x) Exp
EMTopo
1200 GeV < |p_T,avg| < 1500 GeV
Jet 1: 0.3 < |η| < 0.8
Jet 2: 0.3 < |η| < 0.8
σ_α: 1.1 +- 8.7
τ: 0.015
p_T,α [GeV]
MC15c Pythia8 Dijet
Fit Gauss (x) Gauss (x) Exp
EMTopo
1200 GeV < |p_T,avg| < 1500 GeV
Jet 1: 0.3 < |η| < 0.8
Jet 2: 0.3 < |η| < 0.8
σ_α: 1.104 +- 8.69
σ_β: 88 +- 0.61
mean: 4.21 +- 0.449
τ: 0.0151 +- 0.000273
Variance: 7.67e+03
p_beta
MC15c Pythia8 Dijet
Fit Gauss (x) Exp
EMPFlow
25 GeV < |p_T,avg| < 40 GeV
Jet 1: 0.3 < |η| < 0.8
Jet 2: 0.3 < |η| < 0.8
σ_α: 9.6 +- 22
τ: 1
p_T,α [GeV]
MC15c Pythia8 Dijet
Fit Gauss (x) Gauss (x) Exp
EMPFlow
25 GeV < |p_T,avg| < 40 GeV
Jet 1: 0.3 < |η| < 0.8
Jet 2: 0.3 < |η| < 0.8
σ_α: 0.585 +- 22.5
σ_β: 8.6 +- 0.51
mean: 5.14 +- 0.164
τ: 1 +- 4.31
Variance: 73.6
p_beta
MC15c Pythia8 Dijet
Fit Gauss (x) Exp
EMPFlow
40 GeV < |p_T,avg| < 60 GeV
Jet 1: 0.3 < |η| < 0.8
Jet 2: 0.3 < |η| < 0.8
σ_α: 1 +- 0.37
τ: 0.097
p_T,α [GeV]
MC15c Pythia8 Dijet
Fit Gauss (x) Gauss (x) Exp
EMPFlow
40 GeV < |p_T,avg| < 60 GeV
Jet 1: 0.3 < |η| < 0.8
Jet 2: 0.3 < |η| < 0.8
σ_α: 1.026 +- 0.374
σ_β: 11 +- 0.37
mean: 4.82 +- 0.296
τ: 0.0966 +- 0.00304
Variance: 126
p_beta
MC15c Pythia8 Dijet
Fit Gauss (x) Exp
EMPFlow
60 GeV < |p_T,avg| < 85 GeV
Jet 1: 0.3 < |η| < 0.8
Jet 2: 0.3 < |η| < 0.8
σ_α: 0.54 +- 0.14
τ: 0.075
p_T,α [GeV]
MC15c Pythia8 Dijet
Fit Gauss (x) Gauss (x) Exp
EMPFlow
60 GeV < |p_T,avg| < 85 GeV
Jet 1: 0.3 < |η| < 0.8
Jet 2: 0.3 < |η| < 0.8
σ_α: 0.5424 +- 0.141
σ_β: 13 +- 0.45
mean: 5.2 +- 0.321
τ: 0.075 +- 0.0027
Variance: 175
p_beta
MC15c Pythia8 Dijet
Fit Gauss (x) Exp
EMPFlow
85 GeV < |p_T,avg| < 115 GeV
Jet 1: 0.3 < |η| < 0.8
Jet 2: 0.3 < |η| < 0.8
σ_α: 16 +- 2.8e+02
τ: 0.71
p_T,α [GeV]
MC15c Pythia8 Dijet
Fit Gauss (x) Gauss (x) Exp
EMPFlow
85 GeV < |p_T,avg| < 115 GeV
Jet 1: 0.3 < |η| < 0.8
Jet 2: 0.3 < |η| < 0.8
σ_α: 15.99 +- 276
σ_β: 20 +- 0.34
mean: 5.05 +- 0.14
τ: 0.71 +- 615
Variance: 381
p_beta
MC15c Pythia8 Dijet
Fit Gauss (x) Exp
EMPFlow
115 GeV < |p_T,avg| < 145 GeV
Jet 1: 0.3 < |η| < 0.8
Jet 2: 0.3 < |η| < 0.8
σ_α: 0.19 +- 0.00029
τ: 0.045
p_T,α [GeV]
MC15c Pythia8 Dijet
Fit Gauss (x) Gauss (x) Exp
EMPFlow
115 GeV < |p_T,avg| < 145 GeV
Jet 1: 0.3 < |η| < 0.8
Jet 2: 0.3 < |η| < 0.8
σ_α: 0.1859 +- 0.000292
σ_β: 19 +- 0.47
mean: 5.36 +- 0.341
τ: 0.0454 +- 0.00107
Variance: 345
p_beta
MC15c Pythia8 Dijet
Fit Gauss (x) Exp
EMPFlow
145 GeV < |p_T,avg| < 175 GeV
Jet 1: 0.3 < |η| < 0.8
Jet 2: 0.3 < |η| < 0.8
σ_α: 0.17 +- 0.67
τ: 0.04
p_T,α [GeV]
MC15c Pythia8 Dijet
Fit Gauss (x) Gauss (x) Exp
EMPFlow
145 GeV < |p_T,avg| < 175 GeV
Jet 1: 0.3 < |η| < 0.8
Jet 2: 0.3 < |η| < 0.8
σ_α: 0.1654 +- 0.665
σ_β: 21 +- 0.5
mean: 4.71 +- 0.333
τ: 0.0398 +- 0.000827
Variance: 440
p_beta
MC15c Pythia8 Dijet
Fit Gauss (x) Exp
EMPFlow
175 GeV < |p_T,avg| < 220 GeV
Jet 1: 0.3 < |η| < 0.8
Jet 2: 0.3 < |η| < 0.8
σ_α: 0.9 +- 7.3e+02
τ: 0.035
p_T,α [GeV]
MC15c Pythia8 Dijet
Fit Gauss (x) Gauss (x) Exp
EMPFlow
175 GeV < |p_T,avg| < 220 GeV
Jet 1: 0.3 < |η| < 0.8
Jet 2: 0.3 < |η| < 0.8
σ_α: 0.902 +- 728
σ_β: 26 +- 0.42
mean: 5.05 +- 0.287
τ: 0.0353 +- 0.000516
Variance: 655
p_beta
MC15c Pythia8 Dijet
Fit Gauss (x) Exp
EMPFlow
220 GeV < |p_T,avg| < 270 GeV
Jet 1: 0.3 < |η| < 0.8
Jet 2: 0.3 < |η| < 0.8
σ_α: 5.1 +- 2.1
τ: 0.031
p_T,α [GeV]
MC15c Pythia8 Dijet
Fit Gauss (x) Gauss (x) Exp
EMPFlow
220 GeV < |p_T,avg| < 270 GeV
Jet 1: 0.3 < |η| < 0.8
Jet 2: 0.3 < |η| < 0.8
σ_α: 5.143 +- 2.08
σ_β: 30 +- 0.39
mean: 5.1 +- 0.143
τ: 0.0314 +- 0.000685
Variance: 924
p_beta

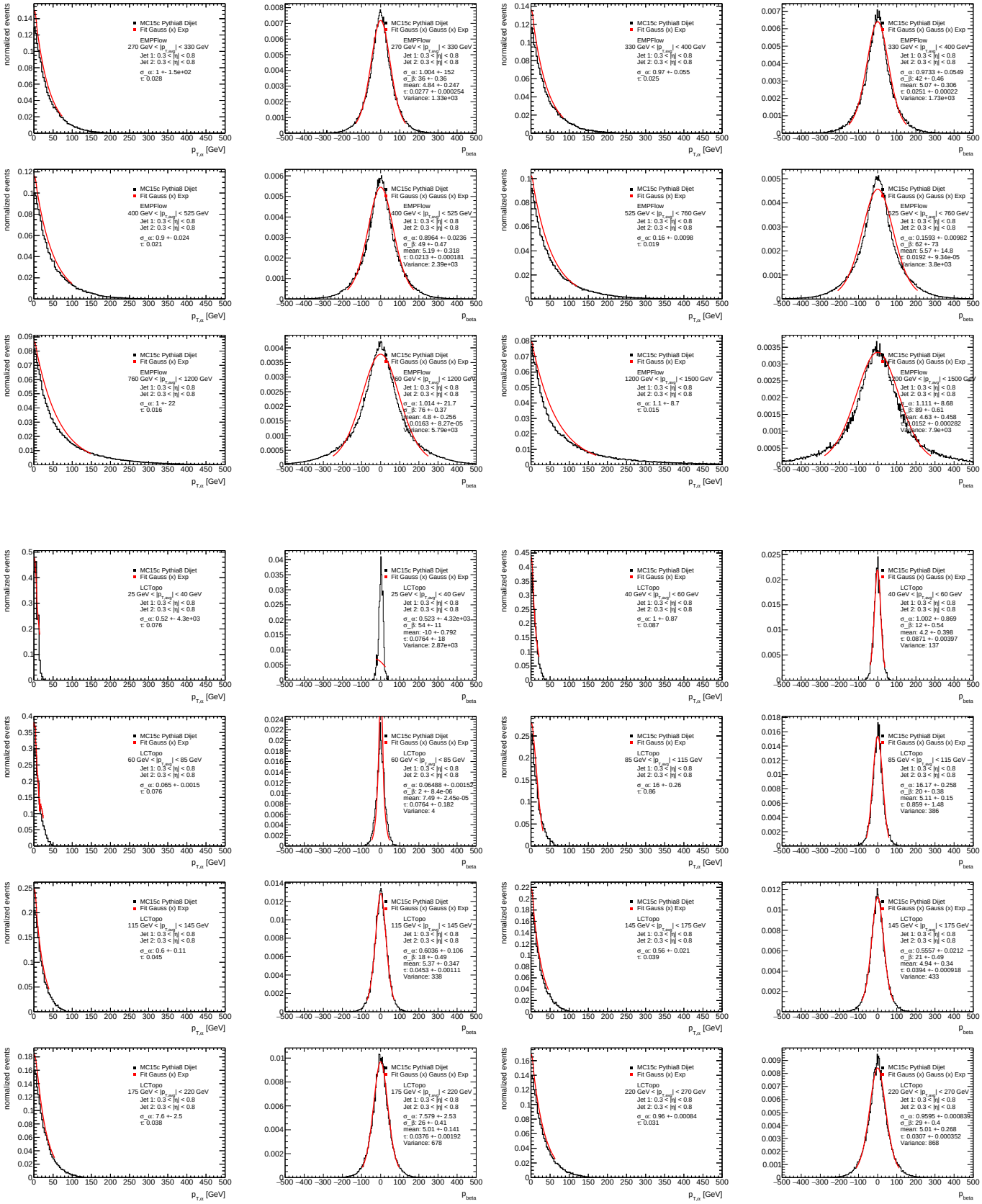
MC15c Pythia8 Dijet
Fit Gauss (x) Exp
Fit Gauss (x) Gauss (x) Exp
normalized events
$p_{T,\alpha}$ [GeV]
p_{beta}

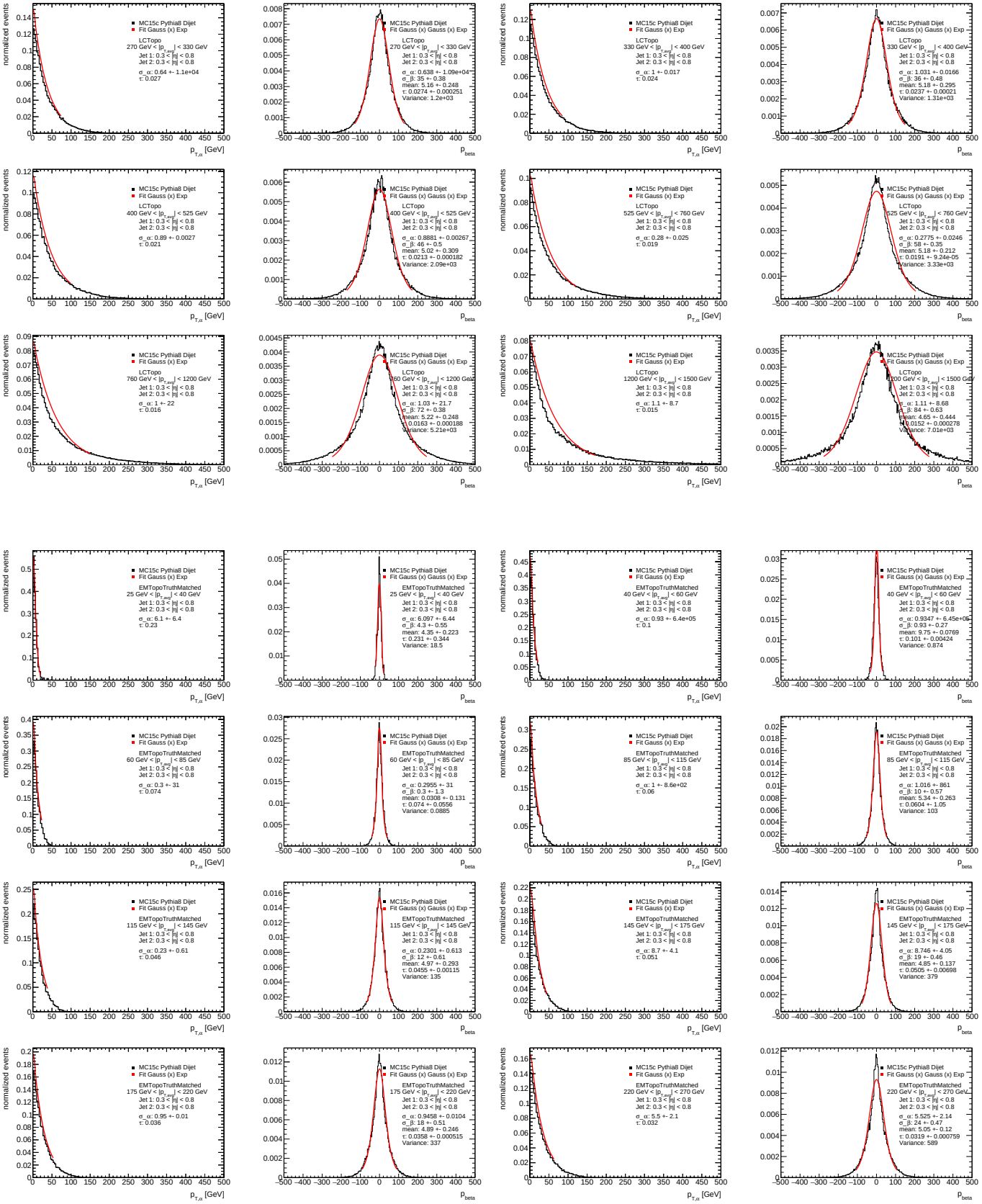
MC15c Pythia8 Dijet
Fit Gauss (x) Exp
LCTopo
270 GeV < |p_T,avg| < 330 GeV
Jet 1: 0.3 < |η| < 0.8
Jet 2: 0.3 < |η| < 0.8
σ_α: 0.64 +- 1.1e+04
τ: 0.027
MC15c Pythia8 Dijet
Fit Gauss (x) Gauss (x) Exp
LCTopo
270 GeV < |p_T,avg| < 330 GeV
Jet 1: 0.3 < |η| < 0.8
Jet 2: 0.3 < |η| < 0.8
σ_α: 0.638 +- 1.09e+04
σ_β: 35 +- 0.38
mean: 5.16 +- 0.248
τ: 0.0274 +- 0.000251
Variance: 1.2e+03
MC15c Pythia8 Dijet
Fit Gauss (x) Exp
LCTopo
330 GeV < |p_T,avg| < 400 GeV
Jet 1: 0.3 < |η| < 0.8
Jet 2: 0.3 < |η| < 0.8
σ_α: 1 +- 0.017
τ: 0.024
MC15c Pythia8 Dijet
Fit Gauss (x) Gauss (x) Exp
LCTopo
330 GeV < |p_T,avg| < 400 GeV
Jet 1: 0.3 < |η| < 0.8
Jet 2: 0.3 < |η| < 0.8
σ_α: 1.031 +- 0.0166
σ_β: 36 +- 0.48
mean: 5.18 +- 0.295
τ: 0.0237 +- 0.00021
Variance: 1.31e+03
MC15c Pythia8 Dijet
Fit Gauss (x) Exp
LCTopo
400 GeV < |p_T,avg| < 525 GeV
Jet 1: 0.3 < |η| < 0.8
Jet 2: 0.3 < |η| < 0.8
σ_α: 0.89 +- 0.0027
τ: 0.021
MC15c Pythia8 Dijet
Fit Gauss (x) Gauss (x) Exp
LCTopo
400 GeV < |p_T,avg| < 525 GeV
Jet 1: 0.3 < |η| < 0.8
Jet 2: 0.3 < |η| < 0.8
σ_α: 0.8881 +- 0.00267
σ_β: 46 +- 0.5
mean: 5.02 +- 0.309
τ: 0.0213 +- 0.000182
Variance: 2.09e+03
MC15c Pythia8 Dijet
Fit Gauss (x) Exp
LCTopo
525 GeV < |p_T,avg| < 760 GeV
Jet 1: 0.3 < |η| < 0.8
Jet 2: 0.3 < |η| < 0.8
σ_α: 0.28 +- 0.025
τ: 0.019
MC15c Pythia8 Dijet
Fit Gauss (x) Gauss (x) Exp
LCTopo
525 GeV < |p_T,avg| < 760 GeV
Jet 1: 0.3 < |η| < 0.8
Jet 2: 0.3 < |η| < 0.8
σ_α: 0.2775 +- 0.0246
σ_β: 58 +- 0.35
mean: 5.18 +- 0.212
τ: 0.0191 +- 9.24e-05
Variance: 3.33e+03
MC15c Pythia8 Dijet
Fit Gauss (x) Exp
LCTopo
760 GeV < |p_T,avg| < 1200 GeV
Jet 1: 0.3 < |η| < 0.8
Jet 2: 0.3 < |η| < 0.8
σ_α: 1 +- 22
τ: 0.016
MC15c Pythia8 Dijet
Fit Gauss (x) Gauss (x) Exp
LCTopo
760 GeV < |p_T,avg| < 1200 GeV
Jet 1: 0.3 < |η| < 0.8
Jet 2: 0.3 < |η| < 0.8
σ_α: 1.03 +- 21.7
σ_β: 72 +- 0.38
mean: 5.22 +- 0.248
τ: 0.0163 +- 0.000188
Variance: 5.21e+03
MC15c Pythia8 Dijet
Fit Gauss (x) Exp
LCTopo
1200 GeV < |p_T,avg| < 1500 GeV
Jet 1: 0.3 < |η| < 0.8
Jet 2: 0.3 < |η| < 0.8
σ_α: 1.1 +- 8.7
τ: 0.015
MC15c Pythia8 Dijet
Fit Gauss (x) Gauss (x) Exp
LCTopo
1200 GeV < |p_T,avg| < 1500 GeV
Jet 1: 0.3 < |η| < 0.8
Jet 2: 0.3 < |η| < 0.8
σ_α: 1.11 +- 8.68
σ_β: 84 +- 0.63
mean: 4.65 +- 0.444
τ: 0.0152 +- 0.000278
Variance: 7.01e+03
MC15c Pythia8 Dijet
Fit Gauss (x) Exp
EMTopoTruthMatched
25 GeV < |p_T,avg| < 40 GeV
Jet 1: 0.3 < |η| < 0.8
Jet 2: 0.3 < |η| < 0.8
σ_α: 6.1 +- 6.4
τ: 0.23
MC15c Pythia8 Dijet
Fit Gauss (x) Gauss (x) Exp
EMTopoTruthMatched
25 GeV < |p_T,avg| < 40 GeV
Jet 1: 0.3 < |η| < 0.8
Jet 2: 0.3 < |η| < 0.8
σ_α: 6.44
σ_β: 4.3 +- 0.55
mean: 4.35 +- 0.223
τ: 0.231 +- 0.344
Variance: 18.5
MC15c Pythia8 Dijet
Fit Gauss (x) Exp
EMTopoTruthMatched
40 GeV < |p_T,avg| < 60 GeV
Jet 1: 0.3 < |η| < 0.8
Jet 2: 0.3 < |η| < 0.8
σ_α: 0.93 +- 6.4e+05
τ: 0.1
MC15c Pythia8 Dijet
Fit Gauss (x) Gauss (x) Exp
EMTopoTruthMatched
40 GeV < |p_T,avg| < 60 GeV
Jet 1: 0.3 < |η| < 0.8
Jet 2: 0.3 < |η| < 0.8
σ_α: 0.9347 +- 6.45e+05
σ_β: 0.93 +- 0.27
mean: 9.75 +- 0.0769
τ: 0.101 +- 0.00424
Variance: 0.874
MC15c Pythia8 Dijet
Fit Gauss (x) Exp
EMTopoTruthMatched
60 GeV < |p_T,avg| < 85 GeV
Jet 1: 0.3 < |η| < 0.8
Jet 2: 0.3 < |η| < 0.8
σ_α: 0.3 +- 31
τ: 0.074
MC15c Pythia8 Dijet
Fit Gauss (x) Gauss (x) Exp
EMTopoTruthMatched
60 GeV < |p_T,avg| < 85 GeV
Jet 1: 0.3 < |η| < 0.8
Jet 2: 0.3 < |η| < 0.8
σ_α: 0.2955 +- 31
σ_β: 0.3 +- 1.3
mean: 0.0308 +- 0.131
τ: 0.074 +- 0.0556
Variance: 0.0885
MC15c Pythia8 Dijet
Fit Gauss (x) Exp
EMTopoTruthMatched
85 GeV < |p_T,avg| < 115 GeV
Jet 1: 0.3 < |η| < 0.8
Jet 2: 0.3 < |η| < 0.8
σ_α: 1 +- 8.6e+02
τ: 0.06
MC15c Pythia8 Dijet
Fit Gauss (x) Gauss (x) Exp
EMTopoTruthMatched
85 GeV < |p_T,avg| < 115 GeV
Jet 1: 0.3 < |η| < 0.8
Jet 2: 0.3 < |η| < 0.8
σ_α: 1.016 +- 861
σ_β: 10 +- 0.57
mean: 5.34 +- 0.263
τ: 0.0604 +- 1.05
Variance: 103
MC15c Pythia8 Dijet
Fit Gauss (x) Exp
EMTopoTruthMatched
115 GeV < |p_T,avg| < 145 GeV
Jet 1: 0.3 < |η| < 0.8
Jet 2: 0.3 < |η| < 0.8
σ_α: 0.23 +- 0.61
τ: 0.046
MC15c Pythia8 Dijet
Fit Gauss (x) Gauss (x) Exp
EMTopoTruthMatched
115 GeV < |p_T,avg| < 145 GeV
Jet 1: 0.3 < |η| < 0.8
Jet 2: 0.3 < |η| < 0.8
σ_α: 0.2301 +- 0.613
σ_β: 12 +- 0.61
mean: 4.97 +- 0.293
τ: 0.0455 +- 0.00115
Variance: 135
MC15c Pythia8 Dijet
Fit Gauss (x) Exp
EMTopoTruthMatched
145 GeV < |p_T,avg| < 175 GeV
Jet 1: 0.3 < |η| < 0.8
Jet 2: 0.3 < |η| < 0.8
σ_α: 8.7 +- 4.1
τ: 0.051
MC15c Pythia8 Dijet
Fit Gauss (x) Gauss (x) Exp
EMTopoTruthMatched
145 GeV < |p_T,avg| < 175 GeV
Jet 1: 0.3 < |η| < 0.8
Jet 2: 0.3 < |η| < 0.8
σ_α: 8.746 +- 4.05
σ_β: 19 +- 0.46
mean: 4.85 +- 0.137
τ: 0.0505 +- 0.00698
Variance: 379
MC15c Pythia8 Dijet
Fit Gauss (x) Exp
EMTopoTruthMatched
175 GeV < |p_T,avg| < 220 GeV
Jet 1: 0.3 < |η| < 0.8
Jet 2: 0.3 < |η| < 0.8
σ_α: 0.95 +- 0.01
τ: 0.036
MC15c Pythia8 Dijet
Fit Gauss (x) Gauss (x) Exp
EMTopoTruthMatched
175 GeV < |p_T,avg| < 220 GeV
Jet 1: 0.3 < |η| < 0.8
Jet 2: 0.3 < |η| < 0.8
σ_α: 0.9458 +- 0.0104
σ_β: 18 +- 0.51
mean: 4.89 +- 0.246
τ: 0.0358 +- 0.000515
Variance: 337
MC15c Pythia8 Dijet
Fit Gauss (x) Exp
EMTopoTruthMatched
220 GeV < |p_T,avg| < 270 GeV
Jet 1: 0.3 < |η| < 0.8
Jet 2: 0.3 < |η| < 0.8
σ_α: 5.5 +- 2.1
τ: 0.032
MC15c Pythia8 Dijet
Fit Gauss (x) Gauss (x) Exp
EMTopoTruthMatched
220 GeV < |p_T,avg| < 270 GeV
Jet 1: 0.3 < |η| < 0.8
Jet 2: 0.3 < |η| < 0.8
σ_α: 5.525 +- 2.14
σ_β: 24 +- 0.47
mean: 5.05 +- 0.12
τ: 0.0319 +- 0.000759
Variance: 589
normalized events
p_T,αt [GeV]
p_beta

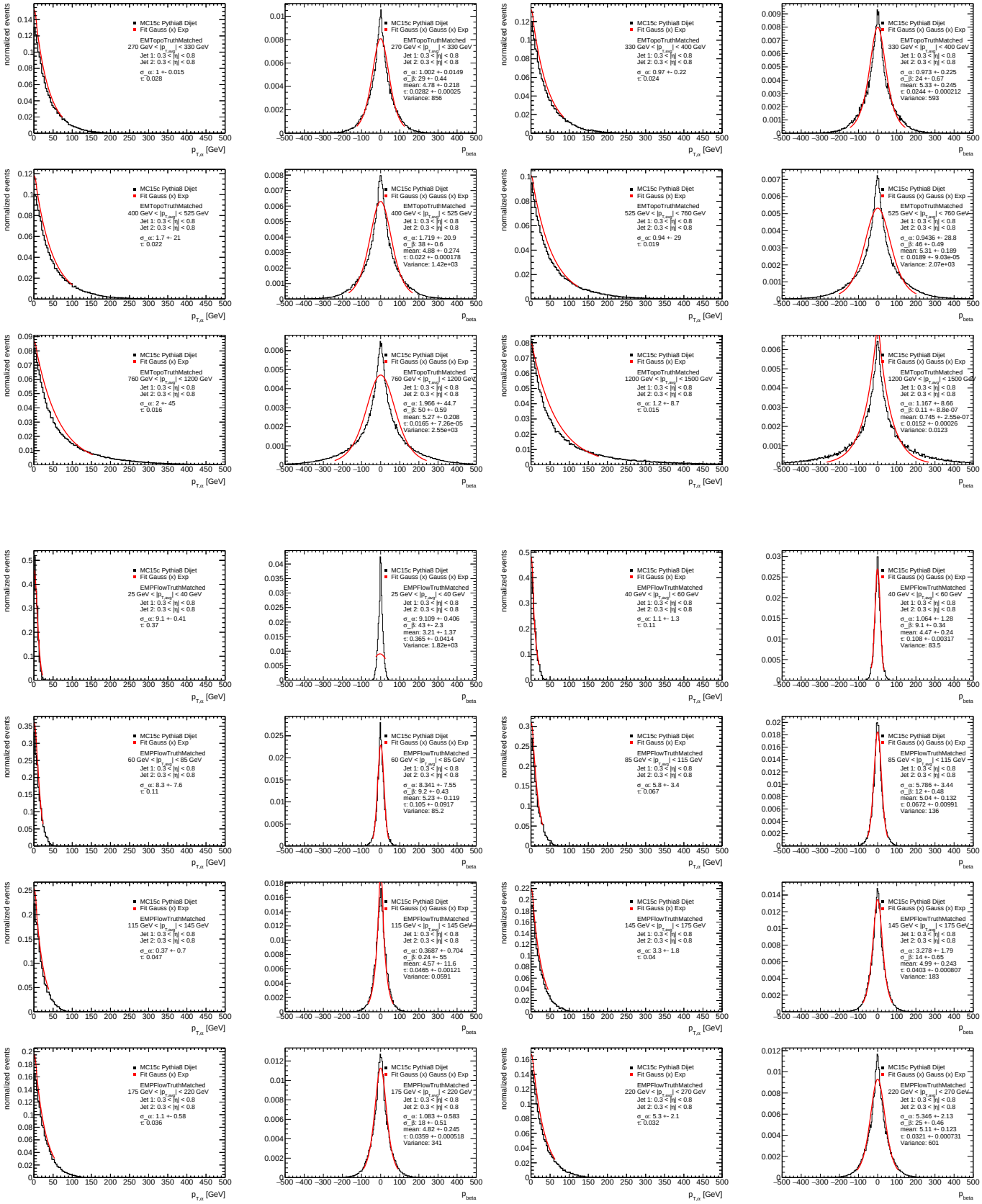
MC15c Pythia8 Dijet
Fit Gauss (x) Exp
EMTopoTruthMatched
270 GeV < |p_T,avg| < 330 GeV
Jet 1: 0.3 < |η| < 0.8
Jet 2: 0.3 < |η| < 0.8
σ_α: 1 +- 0.015
τ: 0.028
MC15c Pythia8 Dijet
Fit Gauss (x) Gauss (x) Exp
EMTopoTruthMatched
270 GeV < |p_T,avg| < 330 GeV
Jet 1: 0.3 < |η| < 0.8
Jet 2: 0.3 < |η| < 0.8
σ_α: 1.002 +- 0.0149
σ_β: 29 +- 0.44
mean: 4.79 +- 0.218
τ: 0.0282 +- 0.00025
Variance: 856
MC15c Pythia8 Dijet
Fit Gauss (x) Exp
EMTopoTruthMatched
330 GeV < |p_T,avg| < 400 GeV
Jet 1: 0.3 < |η| < 0.8
Jet 2: 0.3 < |η| < 0.8
σ_α: 0.97 +- 0.22
τ: 0.024
MC15c Pythia8 Dijet
Fit Gauss (x) Gauss (x) Exp
EMTopoTruthMatched
330 GeV < |p_T,avg| < 400 GeV
Jet 1: 0.3 < |η| < 0.8
Jet 2: 0.3 < |η| < 0.8
σ_α: 0.973 +- 0.225
σ_β: 24 +- 0.67
mean: 5.33 +- 0.245
τ: 0.0244 +- 0.000212
Variance: 593
MC15c Pythia8 Dijet
Fit Gauss (x) Exp
EMTopoTruthMatched
400 GeV < |p_T,avg| < 525 GeV
Jet 1: 0.3 < |η| < 0.8
Jet 2: 0.3 < |η| < 0.8
σ_α: 1.7 +- 21
τ: 0.022
MC15c Pythia8 Dijet
Fit Gauss (x) Gauss (x) Exp
EMTopoTruthMatched
400 GeV < |p_T,avg| < 525 GeV
Jet 1: 0.3 < |η| < 0.8
Jet 2: 0.3 < |η| < 0.8
σ_α: 1.719 +- 20.9
σ_β: 38 +- 0.6
mean: 4.88 +- 0.274
τ: 0.022 +- 0.000178
Variance: 1.42e+03
MC15c Pythia8 Dijet
Fit Gauss (x) Exp
EMTopoTruthMatched
525 GeV < |p_T,avg| < 760 GeV
Jet 1: 0.3 < |η| < 0.8
Jet 2: 0.3 < |η| < 0.8
σ_α: 0.94 +- 29
τ: 0.019
MC15c Pythia8 Dijet
Fit Gauss (x) Gauss (x) Exp
EMTopoTruthMatched
525 GeV < |p_T,avg| < 760 GeV
Jet 1: 0.3 < |η| < 0.8
Jet 2: 0.3 < |η| < 0.8
σ_α: 0.9436 +- 28.8
σ_β: 46 +- 0.49
mean: 5.31 +- 0.189
τ: 0.0189 +- 9.03e-05
Variance: 2.07e+03
MC15c Pythia8 Dijet
Fit Gauss (x) Exp
EMTopoTruthMatched
760 GeV < |p_T,avg| < 1200 GeV
Jet 1: 0.3 < |η| < 0.8
Jet 2: 0.3 < |η| < 0.8
σ_α: 2 +- 45
τ: 0.016
MC15c Pythia8 Dijet
Fit Gauss (x) Gauss (x) Exp
EMTopoTruthMatched
760 GeV < |p_T,avg| < 1200 GeV
Jet 1: 0.3 < |η| < 0.8
Jet 2: 0.3 < |η| < 0.8
σ_α: 1.966 +- 44.7
σ_β: 50 +- 0.59
mean: 5.27 +- 0.208
τ: 0.0165 +- 7.26e-05
Variance: 2.55e+03
MC15c Pythia8 Dijet
Fit Gauss (x) Exp
EMTopoTruthMatched
1200 GeV < |p_T,avg| < 1500 GeV
Jet 1: 0.3 < |η| < 0.8
Jet 2: 0.3 < |η| < 0.8
σ_α: 1.2 +- 8.7
τ: 0.015
MC15c Pythia8 Dijet
Fit Gauss (x) Gauss (x) Exp
EMTopoTruthMatched
1200 GeV < |p_T,avg| < 1500 GeV
Jet 1: 0.3 < |η| < 0.8
Jet 2: 0.3 < |η| < 0.8
σ_α: 1.167 +- 8.66
σ_β: 0.11 +- 8.8e-07
mean: 0.745 +- 2.55e-07
τ: 0.0152 +- 0.00026
Variance: 0.0123
MC15c Pythia8 Dijet
Fit Gauss (x) Exp
EMPFlowTruthMatched
25 GeV < |p_T,avg| < 40 GeV
Jet 1: 0.3 < |η| < 0.8
Jet 2: 0.3 < |η| < 0.8
σ_α: 9.1 +- 0.41
τ: 0.37
MC15c Pythia8 Dijet
Fit Gauss (x) Gauss (x) Exp
EMPFlowTruthMatched
25 GeV < |p_T,avg| < 40 GeV
Jet 1: 0.3 < |η| < 0.8
Jet 2: 0.3 < |η| < 0.8
σ_α: 9.109 +- 0.406
σ_β: 43 +- 2.3
mean: 3.21 +- 1.37
τ: 0.365 +- 0.0414
Variance: 1.82e+03
MC15c Pythia8 Dijet
Fit Gauss (x) Exp
EMPFlowTruthMatched
40 GeV < |p_T,avg| < 60 GeV
Jet 1: 0.3 < |η| < 0.8
Jet 2: 0.3 < |η| < 0.8
σ_α: 1.1 +- 1.3
τ: 0.11
MC15c Pythia8 Dijet
Fit Gauss (x) Gauss (x) Exp
EMPFlowTruthMatched
40 GeV < |p_T,avg| < 60 GeV
Jet 1: 0.3 < |η| < 0.8
Jet 2: 0.3 < |η| < 0.8
σ_α: 1.064 +- 1.28
σ_β: 9.1 +- 0.34
mean: 4.47 +- 0.24
τ: 0.108 +- 0.000317
Variance: 83.5
MC15c Pythia8 Dijet
Fit Gauss (x) Exp
EMPFlowTruthMatched
60 GeV < |p_T,avg| < 85 GeV
Jet 1: 0.3 < |η| < 0.8
Jet 2: 0.3 < |η| < 0.8
σ_α: 8.3 +- 7.6
τ: 0.11
MC15c Pythia8 Dijet
Fit Gauss (x) Gauss (x) Exp
EMPFlowTruthMatched
60 GeV < |p_T,avg| < 85 GeV
Jet 1: 0.3 < |η| < 0.8
Jet 2: 0.3 < |η| < 0.8
σ_α: 8.341 +- 7.55
σ_β: 9.2 +- 0.43
mean: 5.23 +- 0.119
τ: 0.105 +- 0.0917
Variance: 85.2
MC15c Pythia8 Dijet
Fit Gauss (x) Exp
EMPFlowTruthMatched
85 GeV < |p_T,avg| < 115 GeV
Jet 1: 0.3 < |η| < 0.8
Jet 2: 0.3 < |η| < 0.8
σ_α: 5.8 +- 3.4
τ: 0.067
MC15c Pythia8 Dijet
Fit Gauss (x) Gauss (x) Exp
EMPFlowTruthMatched
85 GeV < |p_T,avg| < 115 GeV
Jet 1: 0.3 < |η| < 0.8
Jet 2: 0.3 < |η| < 0.8
σ_α: 5.786 +- 3.44
σ_β: 12 +- 0.48
mean: 5.04 +- 0.132
τ: 0.0672 +- 0.00991
Variance: 136
MC15c Pythia8 Dijet
Fit Gauss (x) Exp
EMPFlowTruthMatched
115 GeV < |p_T,avg| < 145 GeV
Jet 1: 0.3 < |η| < 0.8
Jet 2: 0.3 < |η| < 0.8
σ_α: 0.37 +- 0.7
τ: 0.047
MC15c Pythia8 Dijet
Fit Gauss (x) Gauss (x) Exp
EMPFlowTruthMatched
115 GeV < |p_T,avg| < 145 GeV
Jet 1: 0.3 < |η| < 0.8
Jet 2: 0.3 < |η| < 0.8
σ_α: 0.3687 +- 0.704
σ_β: 0.24 +- 55
mean: 4.57 +- 11.6
τ: 0.0465 +- 0.00121
Variance: 0.0591
MC15c Pythia8 Dijet
Fit Gauss (x) Exp
EMPFlowTruthMatched
145 GeV < |p_T,avg| < 175 GeV
Jet 1: 0.3 < |η| < 0.8
Jet 2: 0.3 < |η| < 0.8
σ_α: 3.3 +- 1.8
τ: 0.04
MC15c Pythia8 Dijet
Fit Gauss (x) Gauss (x) Exp
EMPFlowTruthMatched
145 GeV < |p_T,avg| < 175 GeV
Jet 1: 0.3 < |η| < 0.8
Jet 2: 0.3 < |η| < 0.8
σ_α: 3.278 +- 1.79
σ_β: 14 +- 0.65
mean: 4.99 +- 0.243
τ: 0.0403 +- 0.000807
Variance: 183
MC15c Pythia8 Dijet
Fit Gauss (x) Exp
EMPFlowTruthMatched
175 GeV < |p_T,avg| < 220 GeV
Jet 1: 0.3 < |η| < 0.8
Jet 2: 0.3 < |η| < 0.8
σ_α: 1.1 +- 0.58
τ: 0.036
MC15c Pythia8 Dijet
Fit Gauss (x) Gauss (x) Exp
EMPFlowTruthMatched
175 GeV < |p_T,avg| < 220 GeV
Jet 1: 0.3 < |η| < 0.8
Jet 2: 0.3 < |η| < 0.8
σ_α: 1.083 +- 0.583
σ_β: 18 +- 0.51
mean: 4.82 +- 0.245
τ: 0.0359 +- 0.000518
Variance: 341
MC15c Pythia8 Dijet
Fit Gauss (x) Exp
EMPFlowTruthMatched
220 GeV < |p_T,avg| < 270 GeV
Jet 1: 0.3 < |η| < 0.8
Jet 2: 0.3 < |η| < 0.8
σ_α: 5.3 +- 2.1
τ: 0.032
MC15c Pythia8 Dijet
Fit Gauss (x) Gauss (x) Exp
EMPFlowTruthMatched
220 GeV < |p_T,avg| < 270 GeV
Jet 1: 0.3 < |η| < 0.8
Jet 2: 0.3 < |η| < 0.8
σ_α: 5.346 +- 2.13
σ_β: 25 +- 0.46
mean: 5.11 +- 0.123
τ: 0.0321 +- 0.000731
Variance: 601
normalized events
p_T,jet [GeV]
p_beta

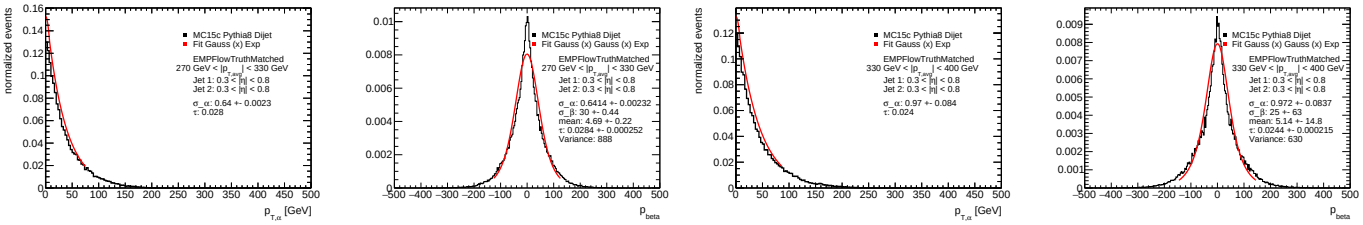
normalized events
MC15c Pythia8 Dijet
Fit Gauss (x) Exp
EMPFlowTruthMatched
270 GeV < |p_T,avg| < 330 GeV
Jet 1: 0.3 < |η| < 0.8
Jet 2: 0.3 < |η| < 0.8
σ_α: 0.64 +- 0.0023
τ: 0.028
p_T,α [GeV]
MC15c Pythia8 Dijet
Fit Gauss (x) Gauss (x) Exp
EMPFlowTruthMatched
270 GeV < |p_T,avg| < 330 GeV
Jet 1: 0.3 < |η| < 0.8
Jet 2: 0.3 < |η| < 0.8
σ_α: 0.6414 +- 0.00232
σ_β: 30 +- 0.44
mean: 4.69 +- 0.22
τ: 0.0284 +- 0.000252
Variance: 888
p_beta
MC15c Pythia8 Dijet
Fit Gauss (x) Exp
EMPFlowTruthMatched
330 GeV < |p_T,avg| < 400 GeV
Jet 1: 0.3 < |η| < 0.8
Jet 2: 0.3 < |η| < 0.8
σ_α: 0.97 +- 0.084
τ: 0.024
p_T,α [GeV]
MC15c Pythia8 Dijet
Fit Gauss (x) Gauss (x) Exp
EMPFlowTruthMatched
330 GeV < |p_T,avg| < 400 GeV
Jet 1: 0.3 < |η| < 0.8
Jet 2: 0.3 < |η| < 0.8
σ_α: 0.972 +- 0.0837
σ_β: 25 +- 63
mean: 5.14 +- 14.8
τ: 0.0244 +- 0.000215
Variance: 630
p_beta

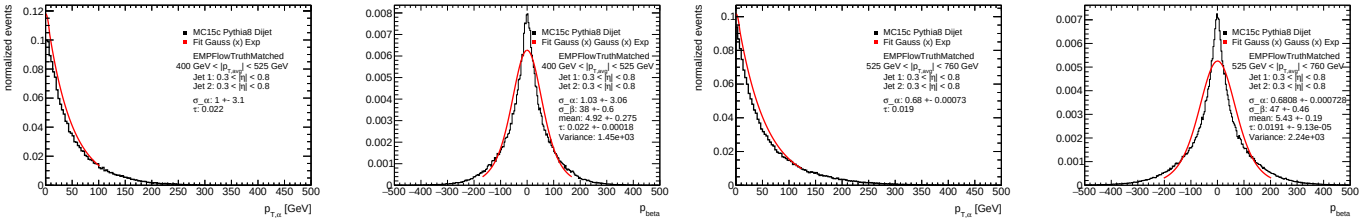
normalized events
MC15c Pythia8 Dijet
Fit Gauss (x) Exp
EMPFlowTruthMatched
400 GeV < |p_T,avg| < 525 GeV
Jet 1: 0.3 < |η| < 0.8
Jet 2: 0.3 < |η| < 0.8
σ_α: 1 +- 3.1
τ: 0.022
p_T,α [GeV]
MC15c Pythia8 Dijet
Fit Gauss (x) Gauss (x) Exp
EMPFlowTruthMatched
400 GeV < |p_T,avg| < 525 GeV
Jet 1: 0.3 < |η| < 0.8
Jet 2: 0.3 < |η| < 0.8
σ_α: 1.03 +- 3.06
σ_β: 38 +- 0.6
mean: 4.92 +- 0.275
τ: 0.022 +- 0.00018
Variance: 1.45e+03
p_beta
MC15c Pythia8 Dijet
Fit Gauss (x) Exp
EMPFlowTruthMatched
525 GeV < |p_T,avg| < 760 GeV
Jet 1: 0.3 < |η| < 0.8
Jet 2: 0.3 < |η| < 0.8
σ_α: 0.68 +- 0.00073
τ: 0.019
p_T,α [GeV]
MC15c Pythia8 Dijet
Fit Gauss (x) Gauss (x) Exp
EMPFlowTruthMatched
525 GeV < |p_T,avg| < 760 GeV
Jet 1: 0.3 < |η| < 0.8
Jet 2: 0.3 < |η| < 0.8
σ_α: 0.6808 +- 0.000728
σ_β: 47 +- 0.46
mean: 5.43 +- 0.19
τ: 0.0191 +- 9.13e-05
Variance: 2.24e+03
p_beta

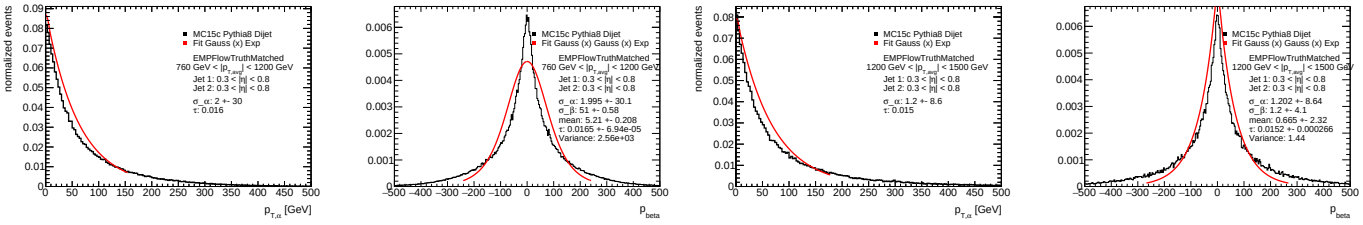
normalized events
MC15c Pythia8 Dijet
Fit Gauss (x) Exp
EMPFlowTruthMatched
760 GeV < |p_T,avg| < 1200 GeV
Jet 1: 0.3 < |η| < 0.8
Jet 2: 0.3 < |η| < 0.8
σ_α: 2 +- 30
τ: 0.016
p_T,α [GeV]
MC15c Pythia8 Dijet
Fit Gauss (x) Gauss (x) Exp
EMPFlowTruthMatched
760 GeV < |p_T,avg| < 1200 GeV
Jet 1: 0.3 < |η| < 0.8
Jet 2: 0.3 < |η| < 0.8
σ_α: 1.995 +- 30.1
σ_β: 51 +- 0.58
mean: 5.21 +- 0.208
τ: 0.0165 +- 6.94e-05
Variance: 2.56e+03
p_beta
MC15c Pythia8 Dijet
Fit Gauss (x) Exp
EMPFlowTruthMatched
1200 GeV < |p_T,avg| < 1500 GeV
Jet 1: 0.3 < |η| < 0.8
Jet 2: 0.3 < |η| < 0.8
σ_α: 1.2 +- 8.6
τ: 0.015
p_T,α [GeV]
MC15c Pythia8 Dijet
Fit Gauss (x) Gauss (x) Exp
EMPFlowTruthMatched
1200 GeV < |p_T,avg| < 1500 GeV
Jet 1: 0.3 < |η| < 0.8
Jet 2: 0.3 < |η| < 0.8
σ_α: 1.202 +- 8.64
σ_β: 1.2 +- 4.1
mean: 0.665 +- 2.32
τ: 0.0152 +- 0.000266
Variance: 1.44
p_beta

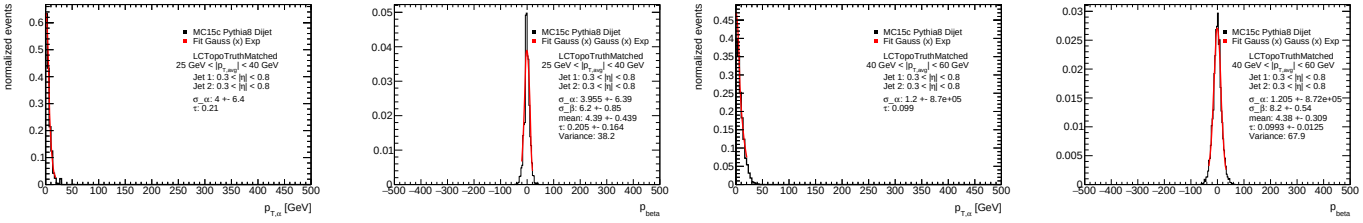
normalized events
MC15c Pythia8 Dijet
Fit Gauss (x) Exp
LCTopoTruthMatched
25 GeV < |p_T,avg| < 40 GeV
Jet 1: 0.3 < |η| < 0.8
Jet 2: 0.3 < |η| < 0.8
σ_α: 1.2 +- 6.4
τ: 0.21
p_T,α [GeV]
MC15c Pythia8 Dijet
Fit Gauss (x) Gauss (x) Exp
LCTopoTruthMatched
25 GeV < |p_T,avg| < 40 GeV
Jet 1: 0.3 < |η| < 0.8
Jet 2: 0.3 < |η| < 0.8
σ_α: 1.355 +- 6.39
σ_β: 6.2 +- 0.85
mean: 4.39 +- 0.439
τ: 0.205 +- 0.164
Variance: 38.2
p_beta
MC15c Pythia8 Dijet
Fit Gauss (x) Exp
LCTopoTruthMatched
40 GeV < |p_T,avg| < 60 GeV
Jet 1: 0.3 < |η| < 0.8
Jet 2: 0.3 < |η| < 0.8
σ_α: 1.2 +- 8.7e+05
τ: 0.099
p_T,α [GeV]
MC15c Pythia8 Dijet
Fit Gauss (x) Gauss (x) Exp
LCTopoTruthMatched
40 GeV < |p_T,avg| < 60 GeV
Jet 1: 0.3 < |η| < 0.8
Jet 2: 0.3 < |η| < 0.8
σ_α: 1.205 +- 8.72e+05
σ_β: 8.2 +- 0.54
mean: 4.38 +- 0.309
τ: 0.0993 +- 0.0125
Variance: 67.9
p_beta

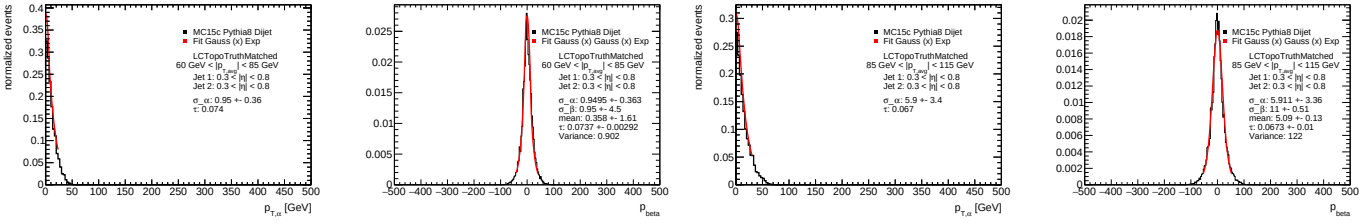
normalized events
MC15c Pythia8 Dijet
Fit Gauss (x) Exp
LCTopoTruthMatched
60 GeV < |p_T,avg| < 85 GeV
Jet 1: 0.3 < |η| < 0.8
Jet 2: 0.3 < |η| < 0.8
σ_α: 0.95 +- 0.36
τ: 0.074
p_T,α [GeV]
MC15c Pythia8 Dijet
Fit Gauss (x) Gauss (x) Exp
LCTopoTruthMatched
60 GeV < |p_T,avg| < 85 GeV
Jet 1: 0.3 < |η| < 0.8
Jet 2: 0.3 < |η| < 0.8
σ_α: 0.9495 +- 0.363
σ_β: 0.95 +- 4.5
mean: 0.358 +- 1.61
τ: 0.0737 +- 0.00292
Variance: 0.902
p_beta
MC15c Pythia8 Dijet
Fit Gauss (x) Exp
LCTopoTruthMatched
85 GeV < |p_T,avg| < 115 GeV
Jet 1: 0.3 < |η| < 0.8
Jet 2: 0.3 < |η| < 0.8
σ_α: 5.9 +- 3.4
τ: 0.067
p_T,α [GeV]
MC15c Pythia8 Dijet
Fit Gauss (x) Gauss (x) Exp
LCTopoTruthMatched
85 GeV < |p_T,avg| < 115 GeV
Jet 1: 0.3 < |η| < 0.8
Jet 2: 0.3 < |η| < 0.8
σ_α: 5.911 +- 3.36
σ_β: 11 +- 0.51
mean: 5.09 +- 0.13
τ: 0.0673 +- 0.01
Variance: 122
p_beta

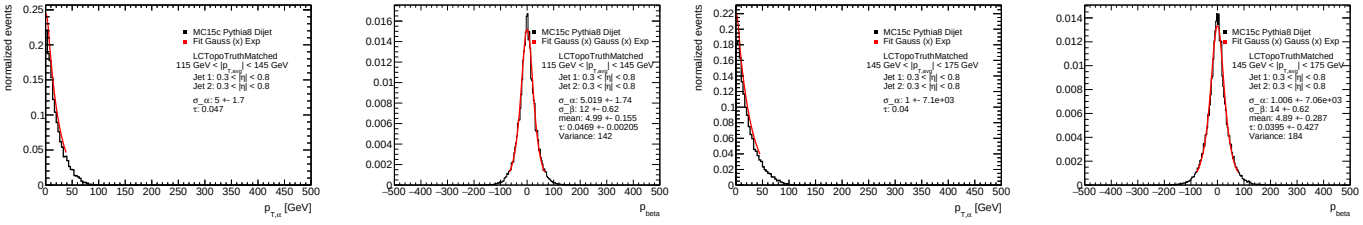
normalized events
MC15c Pythia8 Dijet
Fit Gauss (x) Exp
LCTopoTruthMatched
115 GeV < |p_T,avg| < 145 GeV
Jet 1: 0.3 < |η| < 0.8
Jet 2: 0.3 < |η| < 0.8
σ_α: 5 +- 1.7
τ: 0.047
p_T,α [GeV]
MC15c Pythia8 Dijet
Fit Gauss (x) Gauss (x) Exp
LCTopoTruthMatched
115 GeV < |p_T,avg| < 145 GeV
Jet 1: 0.3 < |η| < 0.8
Jet 2: 0.3 < |η| < 0.8
σ_α: 5.019 +- 1.74
σ_β: 12 +- 0.62
mean: 4.99 +- 0.155
τ: 0.0469 +- 0.00205
Variance: 142
p_beta
MC15c Pythia8 Dijet
Fit Gauss (x) Exp
LCTopoTruthMatched
145 GeV < |p_T,avg| < 175 GeV
Jet 1: 0.3 < |η| < 0.8
Jet 2: 0.3 < |η| < 0.8
σ_α: 1 +- 7.1e+03
τ: 0.04
p_T,α [GeV]
MC15c Pythia8 Dijet
Fit Gauss (x) Gauss (x) Exp
LCTopoTruthMatched
145 GeV < |p_T,avg| < 175 GeV
Jet 1: 0.3 < |η| < 0.8
Jet 2: 0.3 < |η| < 0.8
σ_α: 1.006 +- 7.06e+03
σ_β: 14 +- 0.62
mean: 4.89 +- 0.287
τ: 0.0395 +- 0.427
Variance: 184
p_beta

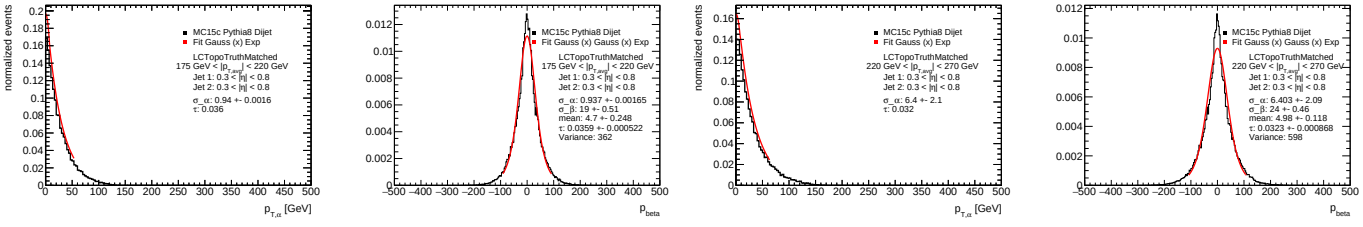
normalized events
MC15c Pythia8 Dijet
Fit Gauss (x) Exp
LCTopoTruthMatched
175 GeV < |p_T,avg| < 220 GeV
Jet 1: 0.3 < |η| < 0.8
Jet 2: 0.3 < |η| < 0.8
σ_α: 0.94 +- 0.0016
τ: 0.036
p_T,α [GeV]
MC15c Pythia8 Dijet
Fit Gauss (x) Gauss (x) Exp
LCTopoTruthMatched
175 GeV < |p_T,avg| < 220 GeV
Jet 1: 0.3 < |η| < 0.8
Jet 2: 0.3 < |η| < 0.8
σ_α: 0.937 +- 0.00165
σ_β: 19 +- 0.51
mean: 4.7 +- 0.248
τ: 0.0359 +- 0.000522
Variance: 362
p_beta
MC15c Pythia8 Dijet
Fit Gauss (x) Exp
LCTopoTruthMatched
220 GeV < |p_T,avg| < 270 GeV
Jet 1: 0.3 < |η| < 0.8
Jet 2: 0.3 < |η| < 0.8
σ_α: 6.4 +- 2.1
τ: 0.032
p_T,α [GeV]
MC15c Pythia8 Dijet
Fit Gauss (x) Gauss (x) Exp
LCTopoTruthMatched
220 GeV < |p_T,avg| < 270 GeV
Jet 1: 0.3 < |η| < 0.8
Jet 2: 0.3 < |η| < 0.8
σ_α: 6.403 +- 2.09
σ_β: 24 +- 0.46
mean: 4.98 +- 0.118
τ: 0.0323 +- 0.000868
Variance: 598
p_beta

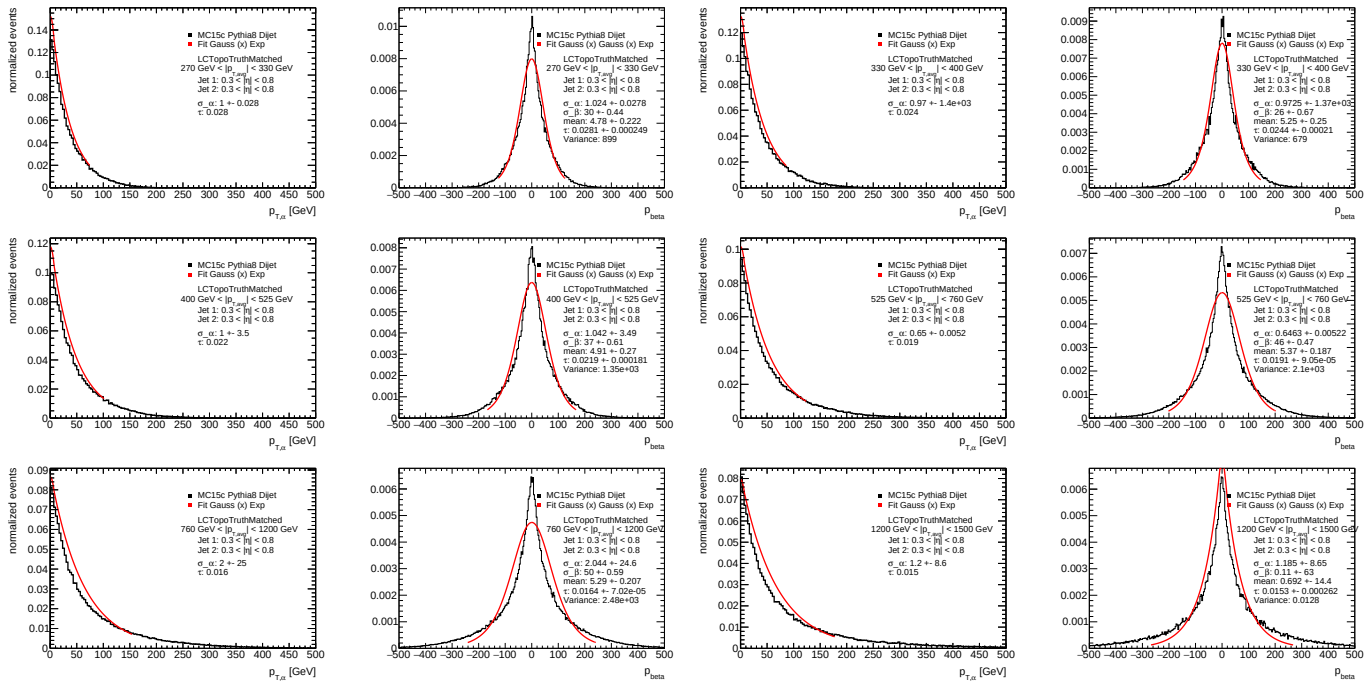
normalized events
MC15c Pythia8 Dijet
Fit Gauss (x) Exp
LCTopoTruthMatched
270 GeV < |p_T,avg| < 330 GeV
Jet 1: 0.3 < |η| < 0.8
Jet 2: 0.3 < |η| < 0.8
σ_α: 1 +- 0.028
τ: 0.028
p_T,jet [GeV]
MC15c Pythia8 Dijet
Fit Gauss (x) Gauss (x) Exp
LCTopoTruthMatched
270 GeV < |p_T,avg| < 330 GeV
Jet 1: 0.3 < |η| < 0.8
Jet 2: 0.3 < |η| < 0.8
σ_α: 1.024 +- 0.0278
σ_β: 30 +- 0.44
mean: 4.78 +- 0.222
τ: 0.0281 +- 0.000249
Variance: 899
p_beta
MC15c Pythia8 Dijet
Fit Gauss (x) Exp
LCTopoTruthMatched
330 GeV < |p_T,avg| < 400 GeV
Jet 1: 0.3 < |η| < 0.8
Jet 2: 0.3 < |η| < 0.8
σ_α: 0.97 +- 1.4e+03
τ: 0.024
p_T,jet [GeV]
MC15c Pythia8 Dijet
Fit Gauss (x) Gauss (x) Exp
LCTopoTruthMatched
330 GeV < |p_T,avg| < 400 GeV
Jet 1: 0.3 < |η| < 0.8
Jet 2: 0.3 < |η| < 0.8
σ_α: 0.9725 +- 1.37e+03
σ_β: 26 +- 0.67
mean: 5.25 +- 0.25
τ: 0.0244 +- 0.00021
Variance: 679
p_beta
normalized events
MC15c Pythia8 Dijet
Fit Gauss (x) Exp
LCTopoTruthMatched
400 GeV < |p_T,avg| < 525 GeV
Jet 1: 0.3 < |η| < 0.8
Jet 2: 0.3 < |η| < 0.8
σ_α: 1 +- 3.5
τ: 0.022
p_T,jet [GeV]
MC15c Pythia8 Dijet
Fit Gauss (x) Gauss (x) Exp
LCTopoTruthMatched
400 GeV < |p_T,avg| < 525 GeV
Jet 1: 0.3 < |η| < 0.8
Jet 2: 0.3 < |η| < 0.8
σ_α: 1.042 +- 3.49
σ_β: 37 +- 0.61
mean: 4.91 +- 0.27
τ: 0.0219 +- 0.000181
Variance: 1.35e+03
p_beta
MC15c Pythia8 Dijet
Fit Gauss (x) Exp
LCTopoTruthMatched
525 GeV < |p_T,avg| < 760 GeV
Jet 1: 0.3 < |η| < 0.8
Jet 2: 0.3 < |η| < 0.8
σ_α: 0.65 +- 0.0052
τ: 0.019
p_T,jet [GeV]
MC15c Pythia8 Dijet
Fit Gauss (x) Gauss (x) Exp
LCTopoTruthMatched
525 GeV < |p_T,avg| < 760 GeV
Jet 1: 0.3 < |η| < 0.8
Jet 2: 0.3 < |η| < 0.8
σ_α: 0.6463 +- 0.00522
σ_β: 46 +- 0.47
mean: 5.37 +- 0.187
τ: 0.0191 +- 9.05e-05
Variance: 2.1e+03
p_beta
normalized events
MC15c Pythia8 Dijet
Fit Gauss (x) Exp
LCTopoTruthMatched
760 GeV < |p_T,avg| < 1200 GeV
Jet 1: 0.3 < |η| < 0.8
Jet 2: 0.3 < |η| < 0.8
σ_α: 2 +- 25
τ: 0.016
p_T,jet [GeV]
MC15c Pythia8 Dijet
Fit Gauss (x) Gauss (x) Exp
LCTopoTruthMatched
760 GeV < |p_T,avg| < 1200 GeV
Jet 1: 0.3 < |η| < 0.8
Jet 2: 0.3 < |η| < 0.8
σ_α: 2.044 +- 24.6
σ_β: 50 +- 0.59
mean: 5.29 +- 0.207
τ: 0.0164 +- 7.02e-05
Variance: 2.48e+03
p_beta
MC15c Pythia8 Dijet
Fit Gauss (x) Exp
LCTopoTruthMatched
1200 GeV < |p_T,avg| < 1500 GeV
Jet 1: 0.3 < |η| < 0.8
Jet 2: 0.3 < |η| < 0.8
σ_α: 1.2 +- 8.6
τ: 0.015
p_T,jet [GeV]
MC15c Pythia8 Dijet
Fit Gauss (x) Gauss (x) Exp
LCTopoTruthMatched
1200 GeV < |p_T,avg| < 1500 GeV
Jet 1: 0.3 < |η| < 0.8
Jet 2: 0.3 < |η| < 0.8
σ_α: 1.185 +- 8.65
σ_β: 0.11 +- 63
mean: 0.692 +- 14.4
τ: 0.0153 +- 0.000262
Variance: 0.0128
p_beta

APPENDIX D

JER plots

In this appendix the JER for all jet collections and $p_{\mathbf{T}}$ as well as |*eta*|-ranges can be seen for data and MC.

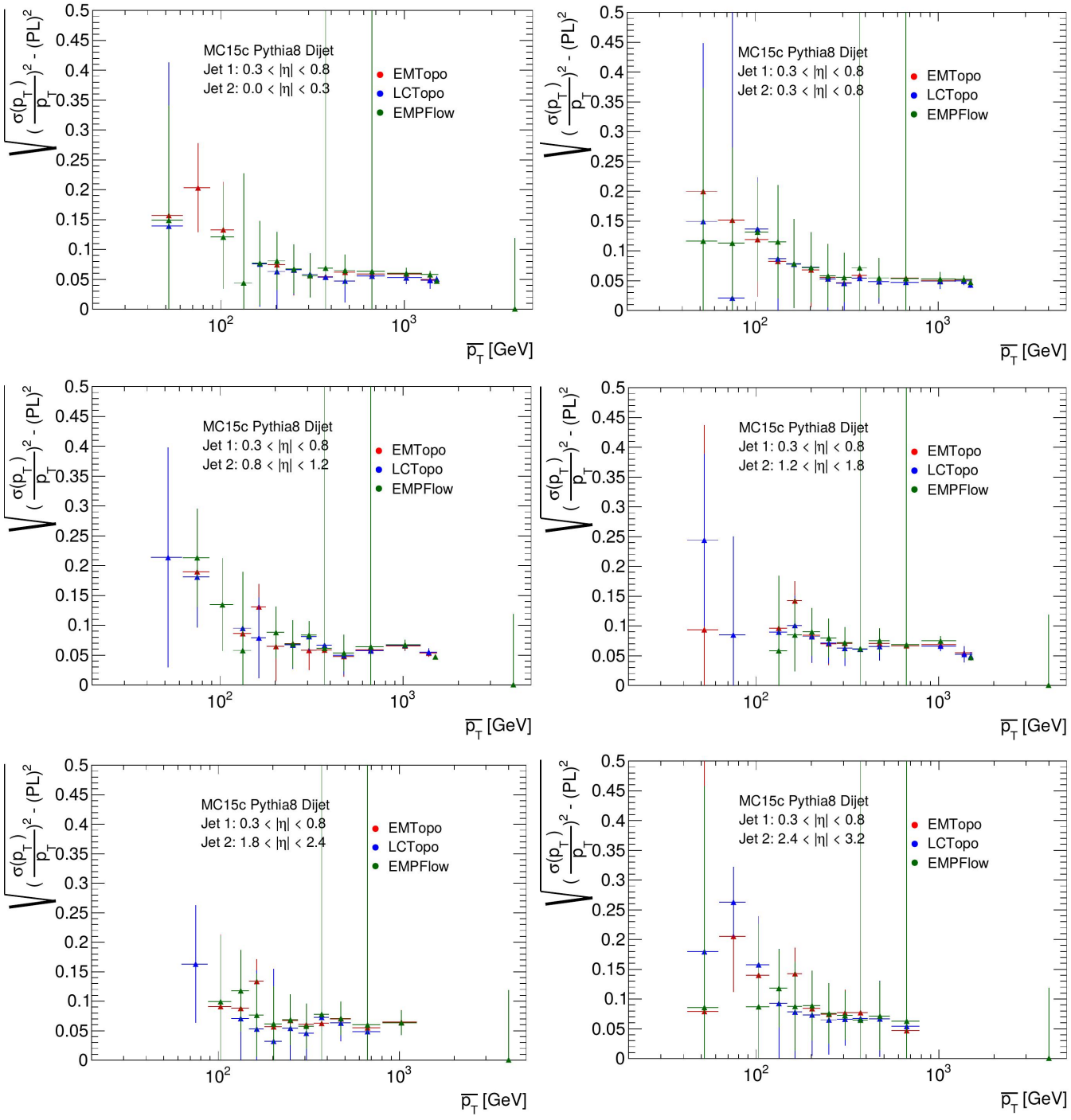

Figure D.1: The JER obtained from MC events as a function of $p_{\mathbf{T}}$.

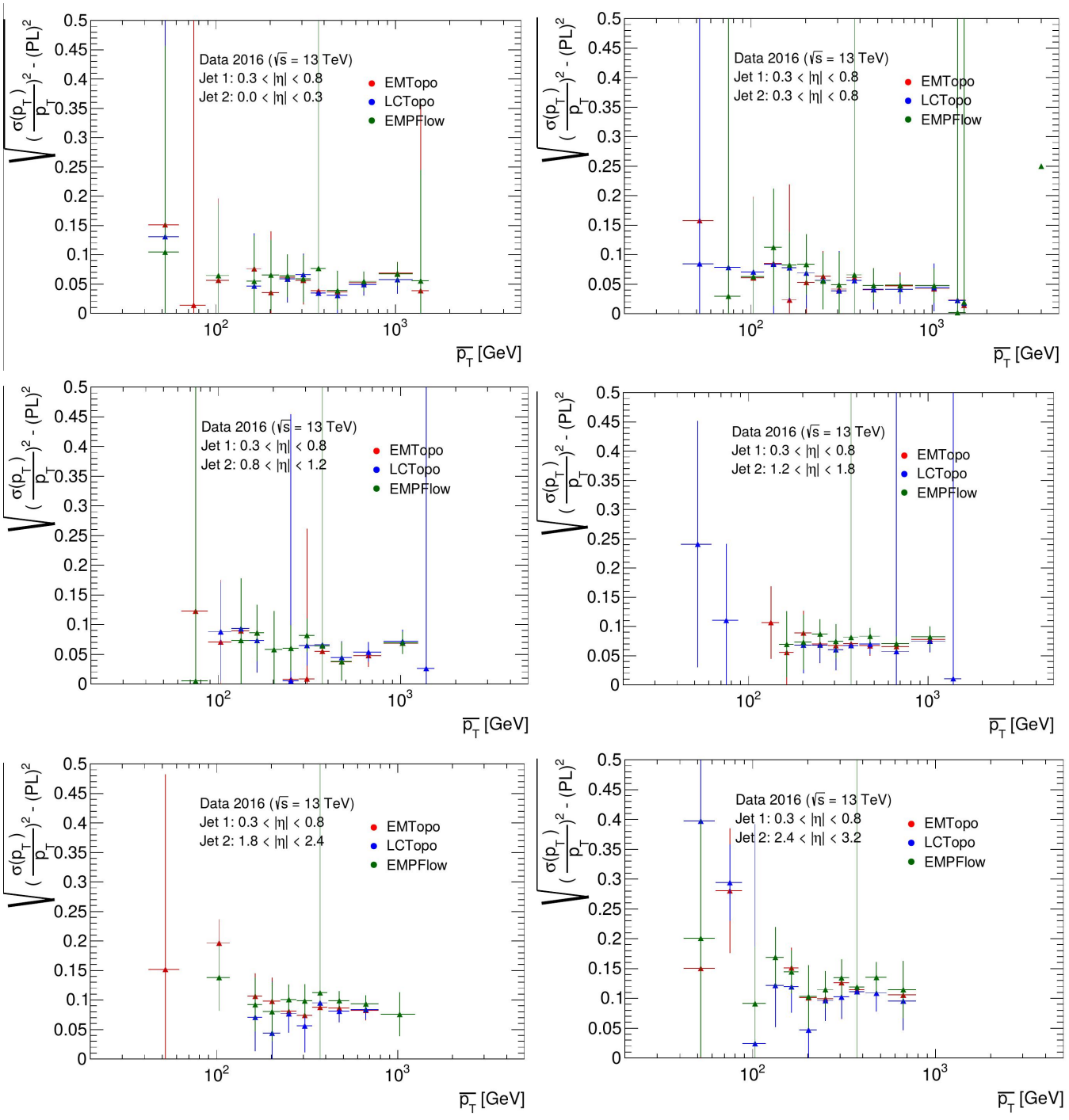

Figure D.2: The JER obtained from data events as a function of $p_{\mathbf{T}}$.

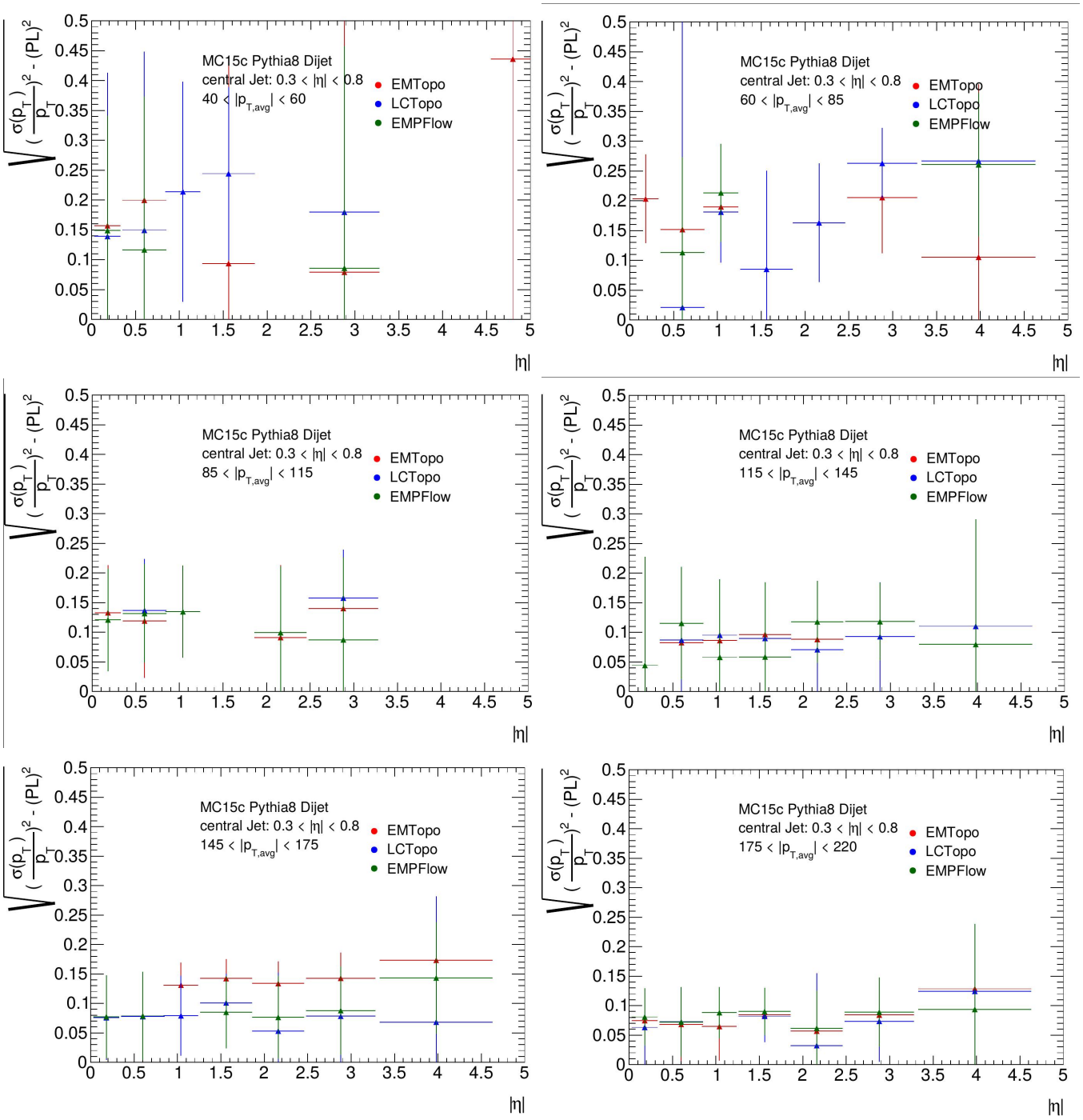

Figure D.3: The JER obtained from MC events as a function of $|\eta|$.

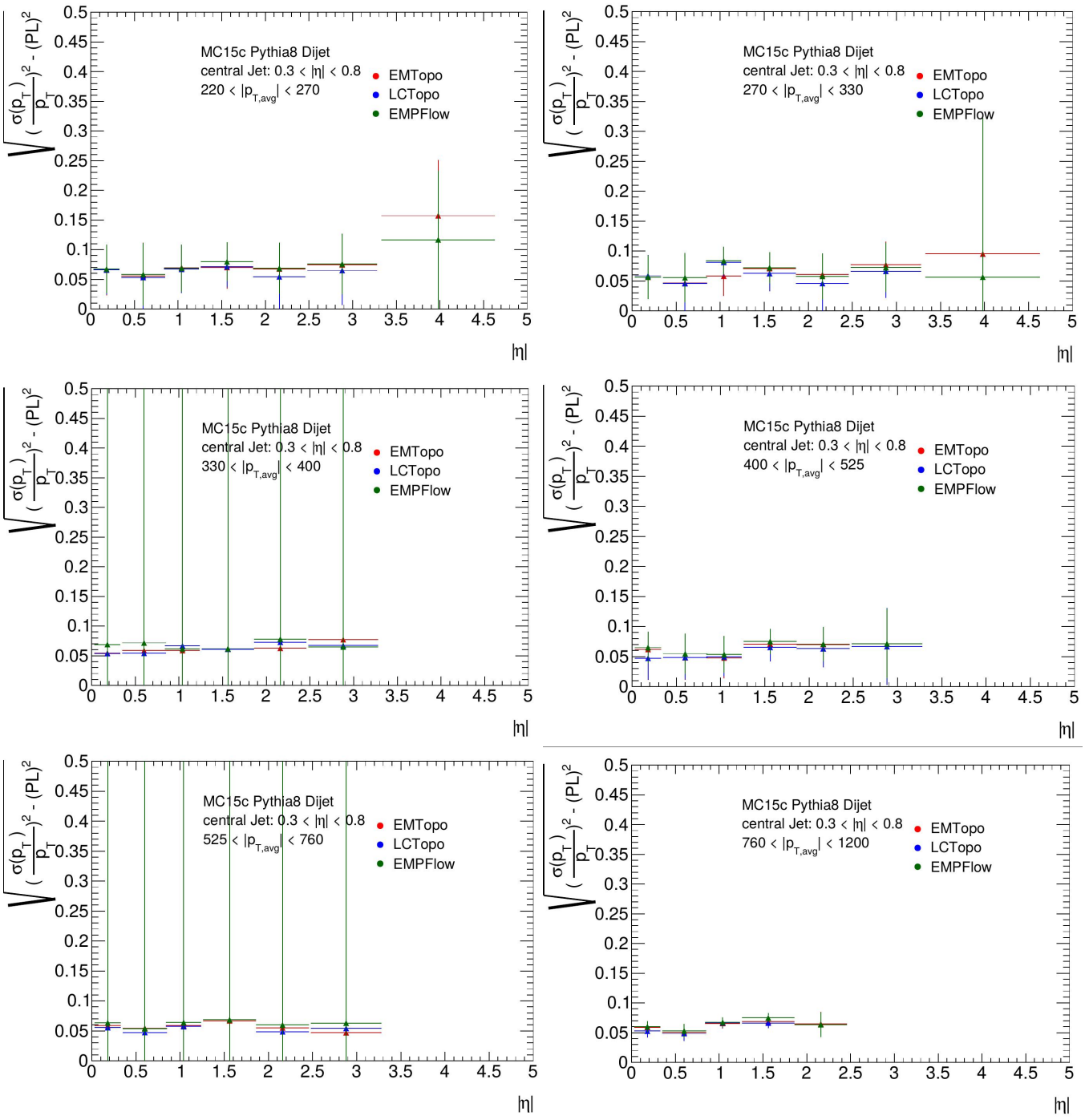

Figure D.4: The JER obtained from MC events as a function of $|\eta|$.

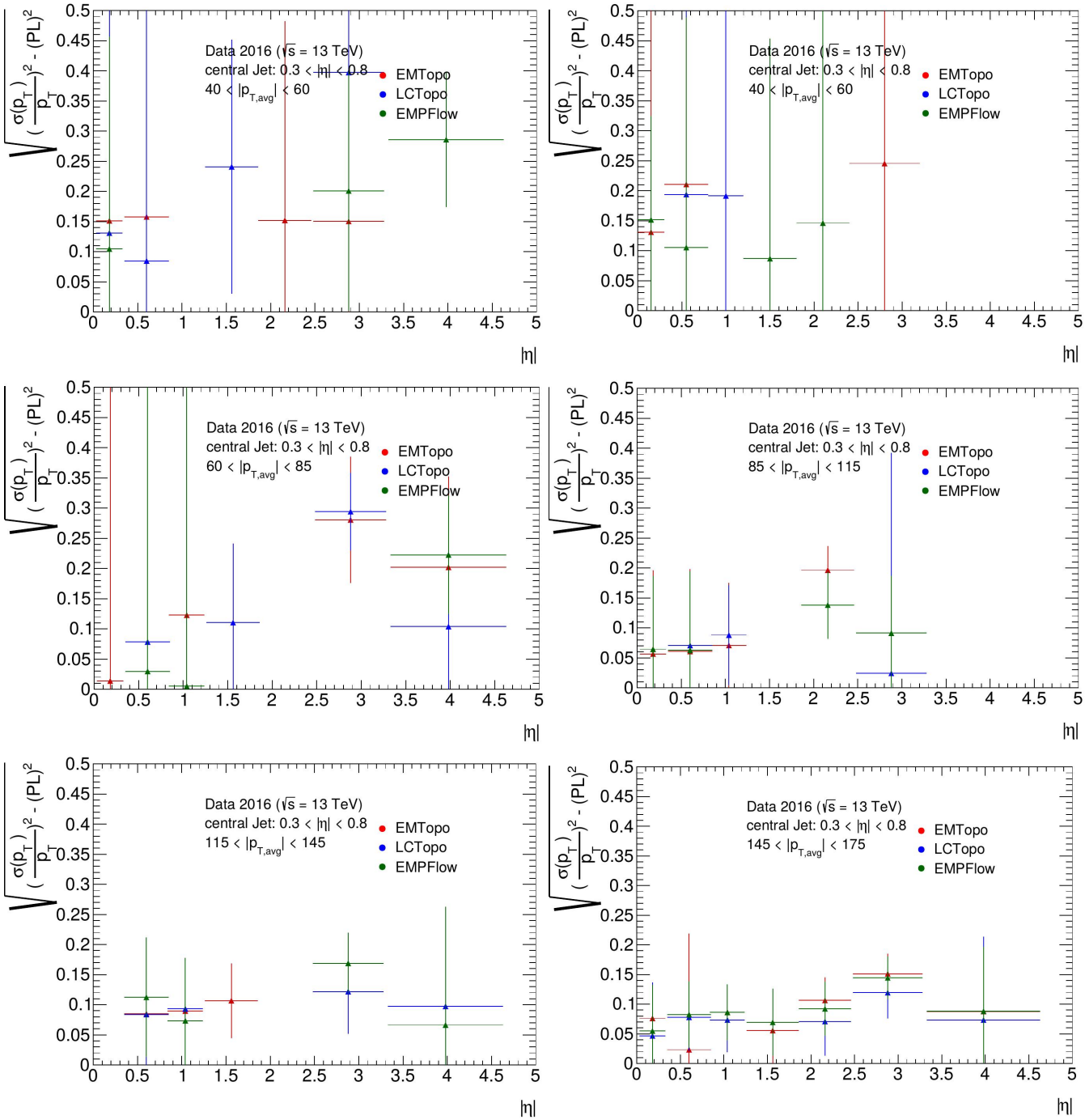

Figure D.5: The JER obtained from data events as a function of p_{T}.

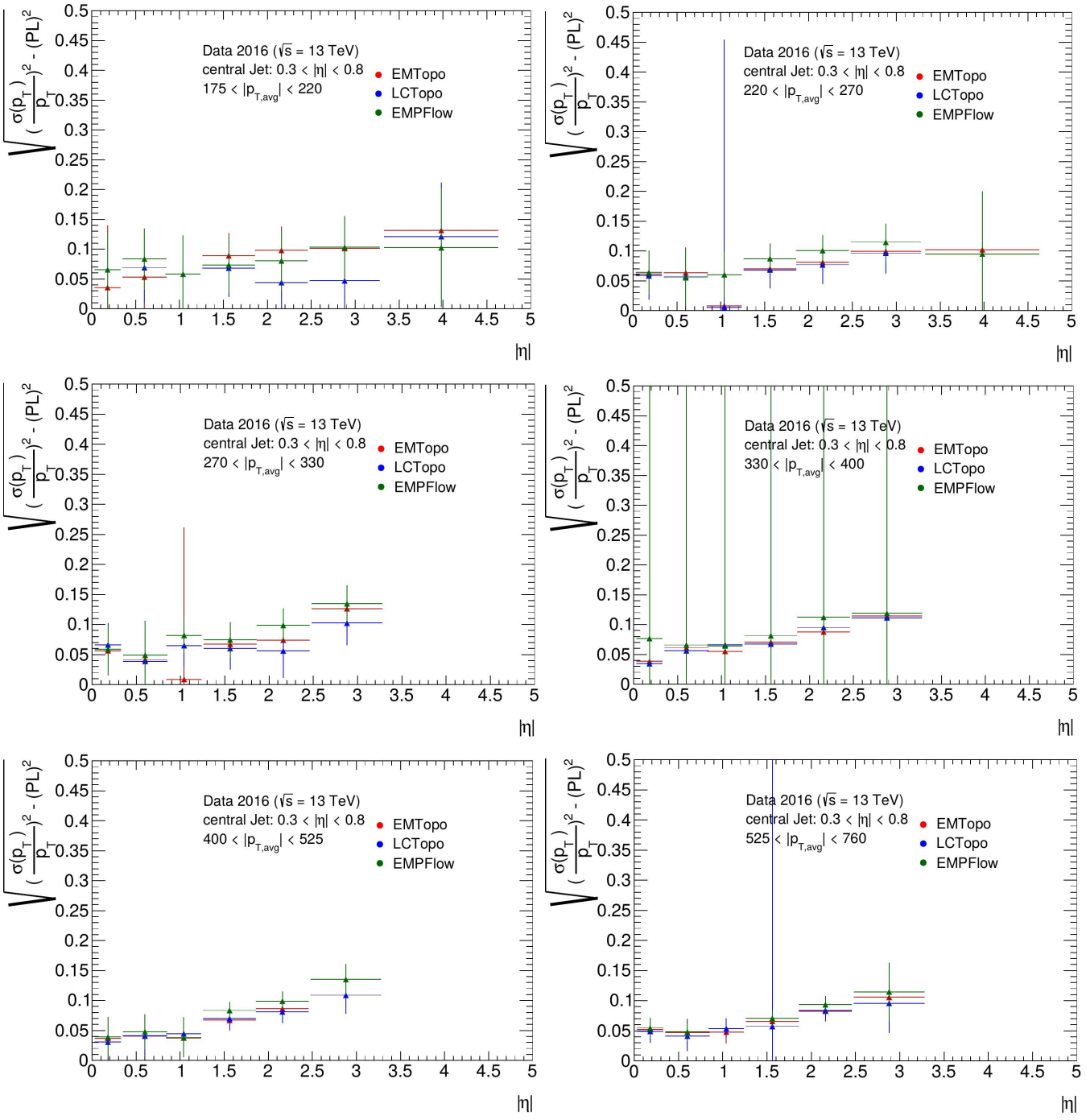

Figure D.6: The JER obtained from data events as a function of $p_{\mathbf{T}}$.

List of Figures

List of Tables